Data-driven X-ray Tomographic Imaging and Applications to 4D Material Characterization

Ziling Wu

Dissertation submitted to the Faculty of the
Virginia Polytechnic Institute and State University
in partial fulfillment of the requirements for the degree of

Doctor of Philosophy
in
Electrical Engineering

Yunhui Zhu, Chair
Ling Li
Z. Hang Yu
Ting-Chung Poon
A. Lynn Abbott

December 4, 2020
Blacksburg, Virginia

Keywords: X-ray tomography, data-driven, insufficient measurements, image processing and analysis, dynamic material characterization

Data-driven X-ray Tomographic Imaging and Applications to 4D Material Characterization

Ziling Wu

ABSTRACT

X-ray tomography is an imaging technique to inspect objects' internal structures with externally measured data by X-ray radiation non-destructively. However, there are concerns about X-ray radiation damage and tomographic acquisition speed in real-life applications. Strategies with insufficient measurements, such as measurements with insufficient dosage (low-dose) and measurements with insufficient projection angles (sparse-view), have been proposed to relieve these problems but are generally compromising imaging quality. Such a dilemma inspires the development of advanced tomographic imaging techniques, in particular, deep learning algorithms to improve reconstruction results with insufficient measurements. The overall aim of this thesis is to design efficient and robust data-driven algorithms with the help of prior knowledge from physics insights and measurement models.

We first introduce a hierarchical synthesis CNN (HSCNN), which is a knowledge-incorporated data-driven tomographic reconstruction method for sparse-view and low-dose tomography with a split-and-synthesis approach. This proposed learning-based method informs the forward model biases based on data-driven learning but with reduced training data. The learning scheme is robust against sampling bias and aberrations introduced in the forward modeling. High-fidelity X-ray tomographic imaging reconstruction results are obtained with a very sparse number of projection angles for both numerical simulated and physics experiments. Comparison with both conventional non-learning-based algorithms and advanced learning-based approaches shows improved accuracy and reduced training data size. As a

result of the split-and-synthesis strategy, the trained network could be transferable to new cases.

We then present a deep learning-based enhancement method, HDrec (hybrid-dose reconstruction algorithm), for low-dose tomography reconstruction via a hybrid-dose acquisition strategy composed of *extremely sparse-view normal-dose measurements* and *full-view low-dose measurements*. The training is applied for each individual sample without the need of transferring the trained models for other samples. Evaluation of two experimental datasets under different hybrid-dose acquisition conditions shows significantly improved structural details and reduced noise levels compared to results with traditional analytical and regularization-based iterative reconstruction methods from uniform acquisitions under the same amount of total dosage. Our proposed approach is also more efficient in terms of single projection denoising and single image reconstruction. In addition, we provide a strategy to distribute dosage smartly with improved reconstruction quality. When the total dosage is limited, the strategy of combining a very few numbers of normal-dose projections and with not-too-low full-view low-dose measurements greatly outperforms the uniform distribution of the dosage throughout all projections.

We finally apply the proposed data-driven X-ray tomographic imaging reconstruction techniques, HSCNN and HDrec, to the dynamic damage/defect characterization applications for the cellular materials and binder jetting additive manufacturing. These proposed algorithms improve data acquisition speeds to record internal dynamic structure changes. A quantitative comprehensive framework is proposed to study the dynamic internal behaviors of cellular structure, which contains four modules: (i) In-situ fast synchrotron X-ray tomography, which enables collection of 3D microstructure in a macroscopic volume; (ii) Automated 3D damage features detection to recognize damage behaviors in different scales; (iii) Quantitative 3D structural analysis of the cellular microstructure, by which key morphological descriptors

of the structure are extracted and quantified; (iv) Automated multi-scale damage structure analysis, which provides a quantitative understanding of damage behaviors. In terms of binder jetting materials, we show a pathway toward the efficient acquisition of holistic defect information and robust morphological representation through the integration of (i) fast tomography algorithms, (ii) 3D morphological analysis, and (iii) machine learning-based big data analysis. The applications to two different 4D material characterization demonstrate the advantages of these proposed tomographic imaging techniques and provide quantitative insights into the global evolution of damage/defect beyond qualitative human observation.

Data-driven X-ray Tomographic Imaging and Applications to 4D Material Characterization

Ziling Wu

GENERAL AUDIENCE ABSTRACT

X-ray tomography is a nondestructive imaging technique to visualize interior structures of non-transparent objects, which has been widely applied to resolve implicit 3D structures, such as human organs and tissues for clinical diagnosis, contents of baggage for security check, internal defect evolution during additive manufacturing, observing fracturing accompanying mechanical tests, and etc. Multiple planar measurements with sufficient X-ray exposure time among different angles are desirable to reconstruct the unique high-quality 3D internal distribution. However, there are practical concerns about X-ray radiation damage to biology samples or long-time acquisition for dynamic experiments in real-life applications. Insufficient measurements by reducing the number of total measurements or the time for each measurement, are proposed to solve this problem but doing so usually leads to the sacrifice of the reconstruction quality. Computational algorithms are developed for tomographic imaging under these insufficient measurement conditions to obtain reconstructions with improved quality.

Deep learning has been successfully applied to numerous areas, such as in recognizing speech, translating languages, detecting objects, and etc. It has also been applied to X-ray tomographic imaging to improve the reconstruction results by learning the features through thousands to millions of corrupted and ideal reconstruction pairs. The aim of this thesis to design efficient deep learning-based algorithms with the help of physical and measurement priors to reduce the number of training datasets.

We propose two different deep learning-based tomographic imaging techniques to improve reconstruction results with reduced training data under different insufficient measurement conditions. One way is to incorporate prior knowledge of the physics models to reduce the required amount of ground truth data, from thousands to hundreds. The training data requirement is further simplified with another hybrid measurement strategy, which could be implemented on each individual sample with only several high-quality measurements. In the end, we apply these two proposed algorithms to different dynamic damage/defect behavior characterization applications. Our methods achieve improved reconstruction results with greatly enhanced experimental speeds, which become suitable for dynamic 3D recording. Final results demonstrate the advantages of the proposed tomographic imaging techniques and provide quantitative insights into the global dynamic evolution inside the material. This quantitative analysis also provides a much more comprehensive understanding than qualitative human observation.

To people who have influenced my life.

Acknowledgments

It is a very valuable journey to go through my Ph.D. study process. I really appreciate this experience, not only for the academic work accomplished and knowledge learned, but also for the people I met during this period. Many people, both in and out Virginia Tech, have offered me indispensable help throughout this wonderful experience and I would like to thank all of you.

First and foremost, I would like to thank my advisor, Prof. Yunhui Zhu for her incredible patience and terrific mentoring when I first come into the lab in 2016. The professional and academic advice/opportunities that she has provided have been extremely valuable to not only accomplish my research work but also broaden my career horizon. I deeply appreciate her guidance and encouragement that I have gained to keep me on the track and to overcome the challenges.

Secondly, I would like to thank Drs. Ling Li and Z. Hang Yu for their advice during our cooperation. Your attitudes to the research and ways to deal with paper writing and figure preparing have influenced my study a lot. I also would like to thank Drs. Ling Li, Z. Hang Yu, Ting-Chung Poon, and A. Lynn Abbott for serving on my thesis committee, your insightful questions and useful suggestions during the preliminary exam and the thesis.

I would like to thank all of my peer colleagues in the Virginia Tech 3D optical information lab, Xiaolong Li, Sibi Chakravarthy, Xiaofeng Wu, Yi Han and all undergraduate students, Baokun Huang, Han Liu, Yuan Chen, and Suhani Pant, who helped me a lot with data processing, experiment acquisitions. I would like to also thank all my collaborators outside our lab, including prof. Ling Li and his students Ting Yang, Hongshun Chen, Zhifei Deng, and Zian Jia, prof. Hang Yu and his students David Garcia and Doug Hartley, prof. prof. A.

Lynn Abbott and his student Abdulaziz Alorf, prof. Guohua Cao and his student Xu Dong. Moreover, I would like to Drs. Tekin Bicer, Zhengchun Liu, Ian T. Foster, and De Andrade, Vincent from Argonne National laboratory for their patient mentor during my remote intern in the summer 2020.

Besides academic corporations, I would like to thank all professors for my course works, including professor Jake Socha from Mechanical Engineering department who taught the writing science course, professor Julianne Chung from Department of Mathematics who taught the Numerical Analysis and Software course, professor Carrie Kroehler from Center for Communicating Science who taught the communication science course, and many other professors. I have learned a lot not only from the lectures but also their helpful discussion. I also would like to thank all the staffs from Electrical and Computer Engineering administration office, Ms. Susan Broniak, Laura Villada Esquivel, and Lewis JoAnna for being my academic advisors on countless program and graduation issues; Ms. Myers, Kyle J., Becky Semones, Melanie Gilmore for numerous payroll problems and purchase orders; Mr. Brandon Russell, Richard Johnston, and Paul E. Plassmann for many facilities and computer problems. I also would like to Mr. Mark Dennis, the international Student Advisor from Cranwell International Center, who helped me a lot with the paperwork for CPT and OPT application.

Last but not least, I would like to thank my parents and my little sister for their fully understanding, and selfless love during this path. I could not finish this journey without their support. And Baoliang Ge, thanks for being my boyfriend and accompanying me during this Covid pandemic period. Thanks for all meals you cooked and advice you offered during my preparation for the graduation and job-seeking. I cannot picture my life without you in the future. I also would like to thank all my friends I knew during the study at VT, including Ying Zhan, Ting Yang, Shan Sun, Xu Dong, Xiaolong Li, Mengyu Song, Ce Zhang,

Yifei Lang, Jia Guo, Bowen Shen, Ziang Feng, and etc. There are so many things we have gone through together. Thanks for all your companion, support, and encouragement. I wish you all the best.

Contents

List of Figures

List of Tables

List of Abbreviations

AIC Akaike information criterion

BIC Bayesian information criterion

DNN Deep neural network

FBP Filtered Back-propagation

GMM Gaussian mixture model

HDrec Hybrid-dose reconstruction

HSCNN Hierarchical synthesis convolution neural network

PCA Principal component analysis

PSNR Peak signal-to-noise ratio

SIRT Simultaneous Iterative Reconstruction Technique

SSIM Structural similarity index

TV Total variation

Chapter 1

Introduction

1.1 Overview of X-ray tomographic imaging

X-ray tomography is an imaging technique to inspect internal structures of an object with externally measured data by X-ray radiation [1, 2]. The measured data, i.e. projections, characterize the interactions between objects and x-ray radiation through the recording the line integral of the objects' linear attenuation coefficient from different angles of view. With sufficient views of X-ray projections, the cross-sectional images can be reconstructed, which is called computed tomography (CT). This kind of non-invasive imaging technology has been widely used to resolve hidden 3D structures [3, 4, 5, 6, 7, 8, 9], and is widely used in applications such as clinical diagnosis in the hospital, baggage scanning in the airport, defect evolution characterization in manufacturing, fracturing observation during mechanical tests, and etc.

Image formation process is described by Radon transform in X-ray tomography, which was first studied in 1917 by Johann Radon. Each projection, which records the attenuated X-ray signals after an object, is formulated as a line (2D object) or planar (3D object) integrals with practical approximations. Figure 1.1(a) illustrates Radon transform for 2D cases and the value of the attenuation along an arbitrary line L is given by the following line integral:

$$g_\theta(s) = \int_L f(r)dr, \tag{1.1}$$

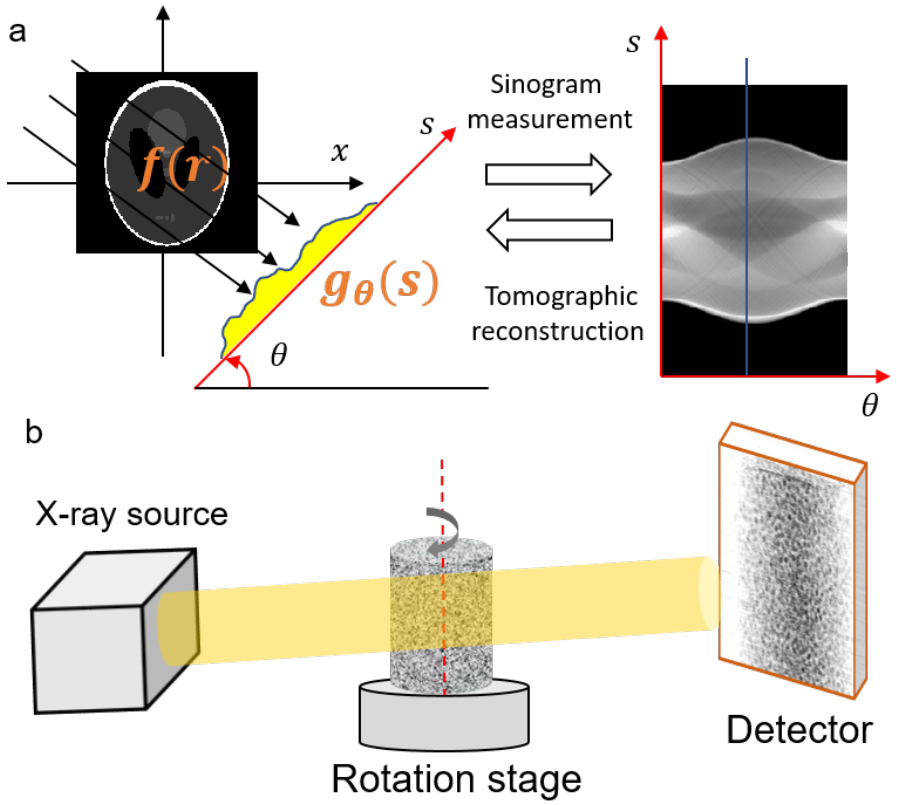

Figure 1.1: Illustration of X-ray tomographic imaging. (a) A 2D slice is recorded as a 1D line through projection. Various viewing angles of 1D projections are formed into a 2D array known as sinogram with respect to the viewing angle θ and the detector locations s. Tomographic reconstruction is obtained from estimating the object from the sinogram measurement. (b) Radon transform of a 3D object generates planar projections.

where $g_\theta(s)$ denotes the measured projection from an arbitrary angle θ, s is the coordinates on the detector and f represents linear attenuation coefficients of the object. 1D projections from various viewing angles are organized into a 2D array with respect to the viewing angle θ and the detector location s, as shown in Fig. 1.1(a). Such a 2D array is often called a sinogram because of the sinusoidal shape. In terms of 3D cases, the Radon transform typically generates planar integrals (Fig. 1.1(b)) in a higher-dimensional space compared to 2D objects.

X-ray tomographic imaging, as one important class of computational imaging, is the process

to retrieve the linear attenuation coefficients of the object $f(r)$ from indirect measurement data $g_\theta(s)$ using algorithms that rely on computation significantly. The image formation process for X-ray tomography, described as Radon transform in Eq. 1.1 before, could be discretized as a forward mapping:

$$\mathbf{b} = \mathbf{A}\mathbf{x} + n, \tag{1.2}$$

where $\mathbf{b}$ represents the measurement data recorded by the detector, $\mathbf{x}$ denotes the underlying tomographic image, $\mathbf{A}$ is the system matrix determined by the imaging protocol used for the tomography experiment, and $\mathbf{n}$ describes the data noise or error introduced by nonidealities of the physics imaging model, which is inevitable for any experiment setup. With this discrete expression of the forward model, X-ray tomographic imaging is formulated as retrieving the image $\mathbf{x}$ from the measurement $\mathbf{b}$, given the imaging system matrix $\mathbf{A}$.

The inverse of Eq. 1.2 could be straightforwardly formulated as a simplistic matrix inversion $\mathbf{x} = \mathbf{A}^{-1}\mathbf{b}$ with a non-singular $\mathbf{A}$ consisting of sufficient number of projection measurements and sufficient exposure time for each projection. However, the matrix $\mathbf{A}$ in tomographic imaging is always associated with a large condition number, meaning direct inversion is prone to large numerical errors. Inversion in the Fourier frequency domain, as stated in the central slice theorem, is a much more practical analytical way that yields a close-form expression.

However, there are concerns about X-ray radiation damage to biology samples or long-time acquisition for dynamic experiments in real-life applications. Fast tomography is desirable for these cases, which are mostly implemented by reducing the number of projections (Fig. 1.2(a) ,i.e., sparse-view) or reducing the time for each projection (Fig. 1.2(b) ,i.e., low-dose). However, insufficient acquisition in fast tomography usually leads to compromised reconstruction results $\mathbf{x}$ [10]. To improve the reconstruction quality, iterative algorithms with prior regularization are used under the condition of insufficient measurements [11].

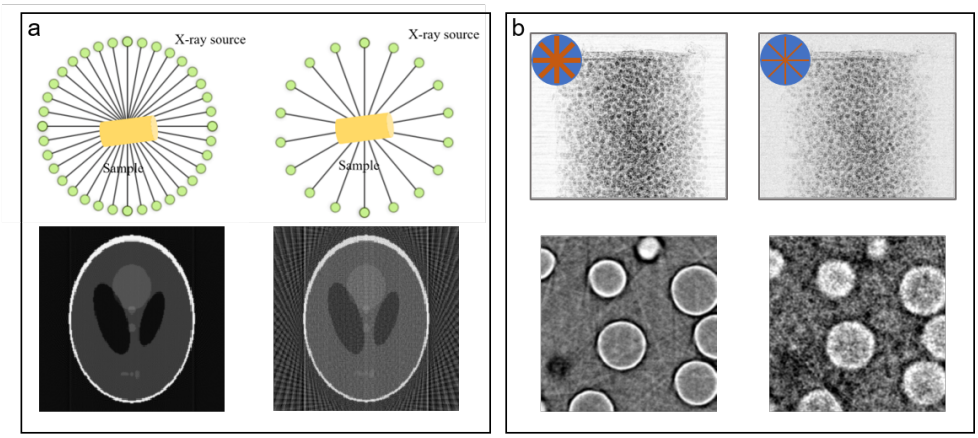

Figure 1.2: Two ways to achieve fast tomography. (a) Sparse-view tomography. (b) Low-dose tomography. The number of total lines in (a) represents the number of total projections and the thickness of each line in (b) represents the dosage value for each projection

Reconstruction results are obtained through iteratively optimizing the objective functions composed of the data-fidelity term that describes the physics detection processes (Eq. 1.2), and/or a regularization term that models the prior knowledge of the reconstructed images $\mathbf{x}$.

The simplest optimization problem without regularization terms is formulated as follows:

$$\hat{x} = \underset{x}{\operatorname{argmin}} \parallel \mathbf{Ax} - \mathbf{b} \parallel_2^2, \tag{1.3}$$

which minimizes the square of the difference between the measurement $\mathbf{b}$ and the calculated response $\mathbf{Ax}$ to constraint the data fidelity. Optimization of this least square method finds a set of solutions that are consistent with the measurement with minimized average energy of noise. Additional information from regularization term can be used to narrow down the solutions via

$$\hat{x} = \underset{x}{\operatorname{argmin}} \parallel \mathbf{Ax} - \mathbf{b} \parallel_2^2 + \lambda\phi(\mathbf{x}). \tag{1.4}$$

Here $\phi(\mathbf{x})$ represents the prior knowledge or the expectations of the reconstructed image

$\mathbf{x}$, and λ is the regularization parameter balancing the data-fidelity term and the constraint regularization term. Various regularizers have been applied to X-ray tomographic imaging reconstruction for different objects of interests, including total variation (TV) and its variants [12, 13], dictionary learning [14], non-local means [15], low-rank and its variants [16, 17, 18], and etc., but solving the optimization problem in Eq. 1.4 generally suffers from long computational time [19, 20, 21, 22]. There are also limitations regarding the inefficiency to represent image global features and constructing the regularizers for arbitrary objects [23].

1.2 Deep learning-based X-ray tomographic imaging

Recent developments in deep learning have shown great potential in a wide range of applications [24, 25, 26], including autonomous driving, natural language processing, image classification, and etc. There are also rapid developments to apply the learning-based algorithms to tomographic imaging reconstruction [27, 28, 29, 30]. These algorithms can be classified into three categories depending on the domain that deep learning techniques are applied as *measurement domain learning*, *model-based approaches*, and *image domain learning* shown in Fig. 1.3.

When operating in the sinogram domain, interpolating the sinogram (sinogram completion) or filtering the sinogram is performed with CNN. Several works are developed to interpolate missing data from the sinogram for sparse-view CT with residual learning for better convergence via patch-wisely training [31, 32, 33, 34]. This framework has high computational efficiency to correct artifacts in the sinogram domain but requires a whole set of high fidelity sinogram data. Yang *et al.* [35] presented a DNN-based method trained using low-/high-dose projection pairs to enhance low-dose X-ray tomographic projections. Besides, methods de-

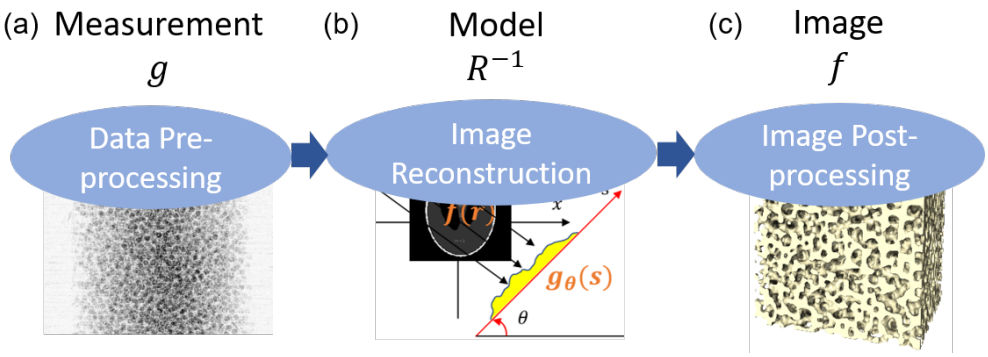

Figure 1.3: Classification of deep learning-based X-ray tomographic imaging methods based on domain that the techniques are applied.

veloped in the sinogram domain are found to result in loss of structural details and reduction of spatial resolution in the reconstructed image.

Deep learning-based algorithms have also been used within or as a replacement for tomographic reconstruction algorithms that connects the sinogram and reconstructed image [23, 36, 37], and produced promising results. The iterative reconstruction models which goes back and forth across the sinogram and image domains are performed with deep neural networks (DNN) with improved image reconstruction quality. One of such multi-domain approach takes the sinogram data as the input and generates the reconstructed image as the output directly [36], where the deep learning network replaces the traditional analytical reconstruction. Another approach is to incorporate a deep neural network powered denoising step into an iterative reconstruction framework as a regularization term [23]. In these methods, the deep learning techniques are combined with an iterative reconstruction algorithm for improved image reconstruction from insufficient measurements. Iterative reconstruction methods which incorporate the physical model into reconstruction procedure lead to superior reconstruction quality and reduced training data at the cost of longer computation time [38, 39].

The post-processing methods operated in the image domain are most popularly applied in

the field of tomographic image reconstruction. This is because the sample features in the image domain are easier to be detected and learned comparing to projections with overlapping features that are more difficult to distinguish [29, 40, 41, 42, 43]. In this approach, low quality image reconstruction is firstly carried out using simple analytical inversion algorithms, and DNNs are then used to remove artifacts and noise from these corrupted reconstructions. Given a set of training data consisting of low-quality tomography reconstructions and their corresponding high-quality images, usually obtained from idealized acquisition conditions, DNN can provide an end-to-end solution that converts future corrupted reconstructions to enhanced estimates. Many DNN-based approaches have been developed to denoise reconstructed images from traditional analytical method, such as multi-resolution convolutional neural network (CNN) [44], mixed-scale dense CNN [45], generative adversarial networks [42], and etc. However, denoising the reconstructed images requires training a model with two 3D volumes from the same sample: one from noisy or incomplete projections and the other from idealized acquisition conditions with high-dose projections, the latter is usually not available for real-life X-ray tomography applications with insufficient measurement. In addition, transferring a trained model to another sample is not trivial, since the learned features and the scale of the noise from one sample are likely mismatches those from another sample. For example, a model trained with shale sample cannot be applied to a plant cell sample; such a transferred reconstruction runs the risk of introducing artifacts in the images and/or losing structural information [40].

The deep learning based tomography reconstruction techniques can also be classified as the data-driven learning and the model-driven learning by the training data size and prior knowledge of the to-be-reconstructed images involved in the learning process, as shown in Fig. 1.4. Data-driven learning frameworks learn the complex statistics from a large training dataset in a pure data-driven approach. These algorithms do not have a structured

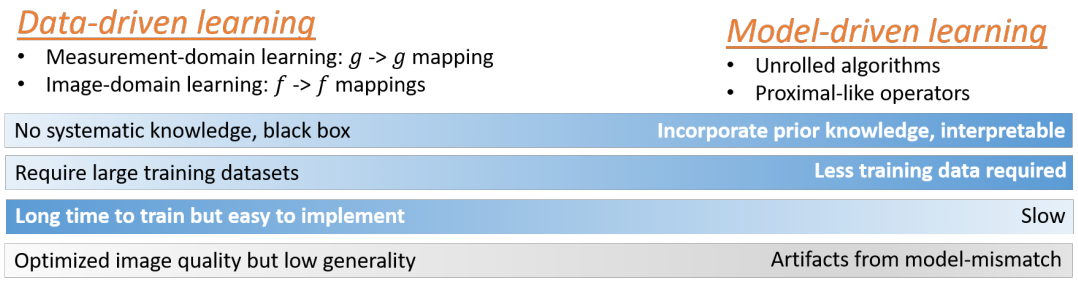

Figure 1.4: Classification of deep learning-based X-ray tomographic imaging methods in terms of the training data size and prior knowledge involved.

way to involve prior physical knowledge of the imaging system into the learning process, and their trained networks are usually difficult to interpret and without convergence guarantees [38].*Measurement domain learning*, and *image domain learning* are mostly operated with the data-driven learning frameworks. In addition, lots of labelled data are required as the ground truth to train a deep neural network and learn the corresponding features for the general cases [46, 47, 48, 49].

Model-driven learning can be trained on a reduced training dataset because it incorporates the prior knowledge of the physical system into the learning process and thereby making it more interpretable [23, 38, 50, 51, 52]. *Model-based approaches* for tomographic imaging are operated in model-driven learning framework. On the downside, model-driven learning is usually computationally expensive to implement and requires accurate model representation.

1.3 X-ray tomographic imaging applied for dynamic material characterization

Material characterization, as a fundamental process in materials science field, refers to the general and broad processes to measure and probe materials' structure [53, 54]. It pro-

vides important scientific insight to understand and determine materials' properties. X-ray tomography is widely adopted within the materials science community to quantify 3D structure and extract key topological parameters [1, 2], such as phase contiguity, phase fractions, density variations, and etc. Inspections of structural development over time, also known as dynamic characterization, provide useful information to understand mechanical properties and optimize manufacturing processes. Examples include following structural damage evolution under different loading conditions in porous materials [55], studying defect evolution during sintering or solidification in metal additive manufacturing [56], tracking particle flow through a constriction [57], and investigating liquid dynamics in the fuel cell [58].

Dynamic material characterization has been challenging as high spatial and temporal resolutions are required to resolve 3D structural information over time [55, 59, 60, 61]. Inspection has been conventionally performed based on histological sections with a few representative slices [62]. Characterization based on 2D histological sections only provides structural behaviors of a specific cross-sectional area, usually leading to loss of information or misinterpretation [63]. It cannot capture volumetric features such as orientation-dependent anisotropy and tortuously propagated cracking paths in damage evolution process of cellular materials [64, 65], and location-dependent thermal histories governed by the component geometries and hatch patterns for metal additive manufacturing [66]. In addition, inherently destructive sectioning may further destroy the structure. X-ray tomography is adopted to capture 3D dynamic structure behaviors for its superior spatial resolution and deep penetration capability. It is an ideal means to track morphological development over time by recording time lapse sequences of 3D images (a.k.a. 4D imaging). For example, inspections of porosity in Laser Powder Bed Fusion based additive manufacturing has been widely explored, revealing a rich database of porosities emerged from various mechanisms, such as keyhole collapse [67] and lack of fusion [68]; fracture mechanics assessment of crack propagation and other types

of damage accumulation from time-lapse image sequences in polymer foams [69, 70, 71], the deformation of natural cellular materials [55, 60, 72, 73], and of geomaterials [74, 75] under compression. However, lab-based X-ray tomography for large-scale sample is usually very slow; it may take hours to characterize a millimeter-scale volume with micrometer-scale spatial resolution. Synchrotron-based X-ray tomography with more enhanced resolution has speed up the acquisition process to some extent. Ultimately, fast tomography combined with computational reconstruction algorithms is expected to further speed up the acquisition and provide a realistic approach for *in situ* 4D dynamic characterization [1].

1.4 Thesis structure

The overall aim of this thesis is to design efficient and robust data-driven algorithms to achieve fast acquisition for dynamic material characterization. The remaining chapters of this dissertation is organized as follows:

Chapter 2 introduces the hierarchical synthesis CNN (HSCNN), which is a knowledge-incorporated data-driven tomographic reconstruction method for sparse-view tomography with split-and-synthesis approach. This proposed learning-based method informs the forward model biases based on data-driven learning and thereby enables a reduced training data size. The learning scheme is more robust against sampling bias and aberrations introduced in the forward modeling. Evaluation on both numerical simulation and physical experiment was conducted to demonstrate the feasibility of the proposed method. High-fidelity X-ray tomographic imaging reconstruction results are obtained with a very sparse number of projection angles. Comparison with both conventional non-learning-based algorithms and advanced learning-based approaches shows improved accuracy. As a result of the split-and-synthesis strategy, the trained network could be transferable to new cases.

Chapter 3 presents a data-driven method to enhance low-dose tomography reconstruction via a hybrid-dose acquisition strategy composed of extremely sparse-view normal-dose projections and full-view low-dose projections. The training is applied for each individual sample without the need of high fidelity volumetric training data. Evaluation on two experimental datasets under different hybrid-dose acquisition conditions show significantly improved structural details and reduced noise levels compared to uniformly distributed acquisitions with the same amount of total dosage. The resulting reconstructions also preserve more structural information than reconstructions processed with traditional analytical and regularization-based iterative reconstruction methods from uniform acquisitions.

Chapter 4 and Chapter 5 present the implementation of proposed two data-driven X-ray tomographic imaging reconstruction techniques to 4D material characterization applications, including dynamic damage behaviors characterization in the cellular materials (Ch. 4), and pore evolution in the binder jetting materials (Ch. 5). Through the integration of fast tomography reconstruction techniques and computer vision-based structural characterization, we demonstrate a pathway towards efficient acquisition of holistic dynamic damage/defect information and robust morphological representation.

Chapter 6 concludes the thesis and discusses the directions for ongoing and future investigations.

1.5 Relevant publications

The following list shows the manuscripts published, accepted, or prepared concurrently with this dissertation.

Journal publications:

1. *Y. Zhu,* ***Z. Wu****, D. Hartley, J. Sietins, C. Williams, and Y. Hang*, Unravel Pore Evolution in Post-Processing of Binder Jetting Materials: X-Ray Computed Tomography, Computer Vision, and Machine Learning, Additive Manufacturing, 2020

2. *T. Yang*,* ***Z. Wu****, H. Chen, Y. Zhu, and L. Li*, Quantitative 3D structural analysis of the cellular microstructure of sea urchin spines (I): Methodology, Acta Biomaterialia, 2020

3. *H. Chen, T. Yang,* ***Z. Wu****, Z. Deng, Y. Zhu, and L. Li*, Quantitative 3D structural analysis of the cellular microstructures of sea urchin spines (II): Large-volume structural analysis, Acta Biomaterialia, 2020

4. ***Z. Wu****, T. Yang*, Z. Deng, B. Huang, H. Liu, Y. Wang, Y. Chen, M. Stoddard, L. Li, and Y. Zhu*, Automatic Crack Detection and Analysis for Biological Cellular Materials in X-Ray In Situ Tomography Measurements, Integrating Materials and Manufacturing Innovation 2019: 1-11

5. *D. Garcia,* ***Z. Wu****, J. Kim, H. Yu, and Y. Zhu*, Heterogeneous Materials Design in Additive Manufacturing: Model Calibration and Uncertainty-Guided Model Selection, Additive Manufacturing, 2019

6. ***Z. Wu****, A. Alorf, T. Yang, L. Li and Y. Zhu*, Robust X-ray Sparse-view Phase Tomography via Hierarchical Synthesis Convolutional Neural Networks,arXiv preprint 2019 (arXiv:1901.10644)

7. ***Z. Wu****, T. Bicer, Z. Liu, V. Andrade, Y. Zhu, and I. Foster* Deep learning-based Low-dose Tomography Reconstruction with Hybrid-dose Measurements, (arXiv publication 2009.13589, accepted by 2020 ACM/IEEE Supercomputing Conference)

8. *T. Yang,* ***Z. Wu****, Z. Jia, H. Chen, Z. Deng, L. Chen, Y. Zhu, and L. Li*, A strong, damage-tolerant natural lightweight ceramic cellular solid, to be submitted.

9. ***Z. Wu****, T. Yang, L. Li and Y. Zhu*, Deep learning enabled autonomous 3D damage detection and characterization for cellular material, to be submitted.

Conference proceedings:

1. *X., Wu,* ***Z. Wu****, and Y. Zhu*, Learning a model-based neural network for quantitative phase imaging based on the transport of intensity. In Computational Imaging V, 2020

2. ***Z. Wu****, X. Wu, and Y. Zhu*, Structured illumination-based phase retrieval via Generative Adversarial Network, Quantitative Phase Imaging VI, vol. 11249, p. 112490L. International Society for Optics and Photonics, 2020

3. ***Z. Wu****, T. Yang, L. Li and Y. Zhu*, A hierarchical reconstruction of limited-view x-ray CT based on non-local structural features,, Anomaly Detection and Imaging with X-Rays (ADIX) IV, 2019

4. ***Z. Wu****, T. Yang, L. Li and Y. Zhu*, Hierarchical convolutional network for sparse-view X-ray CT reconstruction, Computational Imaging IV 10990, 109900V, 2019

5. ***Z. Wu****, T. Yang, L. Li and Y. Zhu*, Four-dimensional X-ray computed tomography reconstruction by feature based iterative algorithms for fast dynamic processes, SPIE Commercial + Scientific Sensing and Imaging, 10669-22, 2018

6. ***Z. Wu****, Xiaolong Li and Y. Zhu*, Retrieval of phase and scattering imaging from incoherent x-ray propagation with phase-space representation, SPIE BiOS, Quantitative Phase Imaging IV, 10503-25, 2018

7. ***Z. Wu****, X. Li and Y. Zhu*, Quantitative X-ray ultra-small angle scattering retrieval with structured illumination for microvessel characterization, Frontiers in Optics, JTu2A. 82, 2017

8. ***Z. Wu****, X. Li and Y. Zhu*, Texture orientation-resolving imaging with structured illumination, SPIE Commercial + Scientific Sensing and Imaging, 102220M-6, 2017

9. ***Z. Wu*** *and Y. Zhu*, Superresolution phase retrieval from non-sinusoidal structure illumination, Propagation Through and Characterization of Atmospheric and Oceanic Phenomena, JTu5A. 21, 2017

Chapter 2

Knowledge-incorporated data-driven tomographic imaging via Hierarchical Synthesis CNN

2.1 Introduction

Driven by the demand to reduce X-ray radiation dose and acquisition time in medical and industrial tomographic imaging applications [15, 44, 76, 77, 78, 79], people have been exploring X-ray tomographic imaging reconstruction with insufficient acquisition via deep learning-based algorithms [28, 80]. As shown in Fig. 1.4, these learning-based tomographic imaging methods could be classified as data-driven learning and model-driven learning, based on the training data size and whether prior knowledge is involved in the learning process. Data-driven learning-based tomographic imaging methods provide a fast and direct reconstruction from an end-to-end CNN at the cost of large size of training data and limited generality. On the contrary, model-driven learning-based methods incorporate the physics model into the reconstruction procedure, and thereby achieve superior reconstruction quality at the cost of longer computation time spend on repeated simulation of the physics model [23, 38, 50, 51, 52]. The choice between data-driven versus model-driven reconstruction is a matter of speed versus quality.

In our study, we propose to integrate the knowledge of possible sampling biases from the physics model to the data-driven learning process, in which way we achieve accurate reconstruction with less computational time and smaller training data size for sparse-view tomography reconstruction. For tomography imaging with insufficient acquisition, the initial reconstruction from conventional analytical algorithm is usually associated with various reconstruction artifacts including the ring effects, beam hardening, diffraction blurring, and Poisson noise. These artifacts and aberration effects are highly nonuniform. For example, the spatial spectral response of Radon transform severely decays at the high end, which makes the inversion prone to noise amplification at the high frequency region [81, 82]. The high spatial frequency insensitivity of CT images deteriorates with reduced projection angles, and is considered as a major obstacle to the scanning speed [83]. Spectrum aberration is also found in phase tomography, where phase induced diffraction emphasizes the high-spatial frequency components and ignores the low-spatial frequency information [84]. On the other hand, Poisson noise is highly sensitive to the intensity of photon flux. The signal-to-noise ratio is dramatically reduced in dimmer places, consequently [85]. All of these non-uniformalities may lead to sample biases in the learning processes.

In this work, we propose a novel CNN-based imaging reconstruction method that introduces a split-and-synthesis learning strategy to address for possible sampling biases. The training samples are pre-processed to split the information into different bands on domains that are prone to processing biases, which are then combined in a hierarchical synthesis network. In our application to X-ray tomographic reconstruction from limited data, the splitting pre-processing is implemented in both the spatial spectral and the intensity domains. We train these split bands in a hierarchical synthesis network, which ensures that different spatial and intensity components are re-balanced correctly in the final reconstruction. Our main contributions are as follows:

- A novel strategy to split the training data on domains of potential biases. This separation pre-processing allows for a guided learning, where physic insights of reconstruction aberration and noise can be integrated into the learning process to avoid overfitting.
- A hierarchical synthesis network that is adaptive to data pool with multiple sampling biases. The synthesis stages of the network enable the rebalance of the data against different sampling biases in each different domain one by one. As a result, the learning scheme is robust against sampling bias and aberrations introduced in the forward modeling.
- An efficient network configuration that works with multi-band information without introducing dense inter-band connections. Reduced computational effort is required as compared to dense connected DNN approaches.
- Application to X-ray phase tomography with insufficient measurement. The proposed method proves to correct for the spectral and intensity biases in both scenarios.
- Successive experimental sparse-view X-ray phase tomography reconstruction. We have demonstrated high-fidelity X-ray phase tomography reconstruction with a very sparse number of projection angles. Comparing to other state-of-the-art methods including FBPConvNet [44] and framing U-Net [86], we achieve better performance in terms of high-frequency information preservation with a significantly reduced computational time.

We also note that our HSCNN method is different from previous proposed multi-scale CNN method. Although the previous deep learning studies have achieved high quality CT reconstructions, most of them cannot be adapted to different biases introduced from the forward modeling. In particular, the existing U-Net architecture does not satisfy the framing condition for non-local basis imposed by deep convolutional framelets, which often result in the emphasis of the low frequency component of the signal (blurring artifacts). It has been

confirmed that the imaging enhancement performance is negatively influenced by the biases in the training data, which are not systematically learned and identified by the CNN [87]. For example, the lack of representation of high frequency components caused by deficient sampling, which can be resultant from the pinkish spectrum of the sparse-view CT reconstruction, can be wrongly interpreted as a feature of the object. Our method, on the other hand, is capable of dealing with biases in multiple domains in an explicit way, therefore can be adaptive to various acquisition conditions in a robust manner.

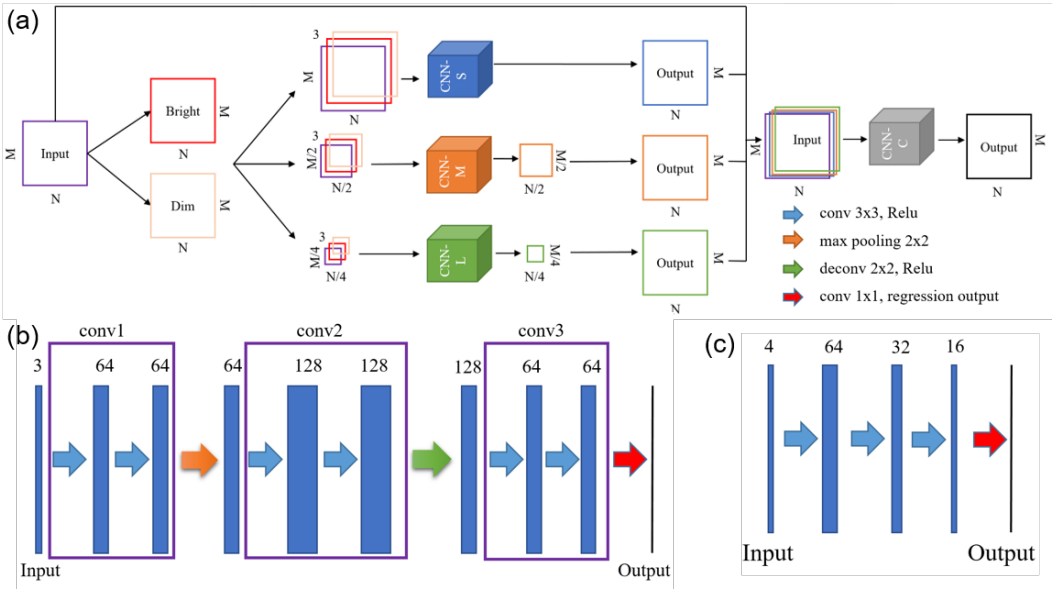

Figure 2.1: Architecture of proposed Hierarchical synthesis of CNNs (HSCNN). (a) Overall network architecture and detailed network construction for feature fusion are shown in (b) for the first stage and in and (c) for the second stage.

2.2 Methods

2.2.1 Hierarchical synthesis of CNNs (HSCNN)

The proposed method involves a hierarchical split-and-combine process for multi-domain bias correction. We choose to separate the training data in both the spatial-frequency domain and the intensity domain, where non-uniformity in the forward transfer functions are observed in tomographic reconstructions. As shown in Fig. 2.1(a), the corrupted tomographic reconstruction images I_0 are first pre-processed to split by intensity and spectral frequency. The bright band I_+ and the dim band I_- are obtained by filtering pixels above and below the average intensity, respectively. These two intensity variations $I_\pm$, together with the original inputs I_0 are concatenated together as the three-channel intensity-split images, denoted as I, and then successively split again into three spatial channels via low-pass filters on different resolution scales. Here we adopt the Gaussian pyramid construction method to generate the spatial splitting images $X_s = g_s(I)$ for all $s \in \{1, 2, 3\}$, where g_s represents a Gaussian average and scaled down function. As shown in the Fig. 2.1(a), each spatial splitting image X_s owns three-channel intensity-splitting distributions. A total of 9 copies of the training data are generated with different spatial-frequency and intensity distributions.

Next, these split sample data are fed into a two-stage hierarchical synthesis learning network. In the first training stage, three convolutional neural networks f_s are constructed for each scale s. f_s combines the corresponding three-channel intensity variations X_s to generate an output of feature maps that matches the ground truth expectations on each of the three different resolution scales. The outputs of these three networks are up-sampled and concatenated together with the original input I_0 to produce the four-channel input F for a second

training stage, which combines the spatial spectral components for the final reconstruction.

$$F = [I_0, f_1, u(f_2), u(f_3)], \tag{2.1}$$

where u represents an up-sampling function through the bi-cubic interpolation to match the size of original input I_0. Each of the separate CNN networks within the same stage can be trained in parallel, allowing for a fast learning of features with different scales and intensities. This hierarchical architecture can be easily extended to include more domain stages and more bands within each stage.

2.2.2 Architecture of CNNs for feature fusion on each stage

The training nodes in stage 1 use the same architecture as shown in Fig. 2.1(b). For each scale network f_s, the corresponding spatial splitting image X_s is used as the input to one convolutional block, which is consist of one convolutional layer and one activation function. We chose to implement rectified linear units ($ReLU$) as the activation function [88, 89], i.e., $ReLU(x) = max(0, x)$. The output of such convolutional block is followed by three residual blocks, each composed of two convolutional layers and two ReLU functions. Residual blocks create a shortcut between the block's input and output, which allows a clear path for information flow between layers. This has been demonstrated to speed up the convergence of the training phase of the deep neural network. The number of feature maps is set to 32 in the first convolutional block and increased to 64 in the following three residual blocks. The size of the convolutional kernels is set as 3×3 throughout the network in our implementation except the final 1x1 convolutional layer. Such 1x1 convolutional layer is followed with regression layers are added for the final output at the end.

The second training stage uses a slightly different network architecture compared to the

training nodes in stage 1, as shown in Fig. 2.1(c). The output of each one of these 3 different data flow paths together with the original input I_0 are concatenated to a 4-channel input F followed the formula shown in the Eq. 2.1. Similar network architecture to the networks in stage 1 with two residual blocks instead of three is used to fuse the feature maps and predict the enhancement.

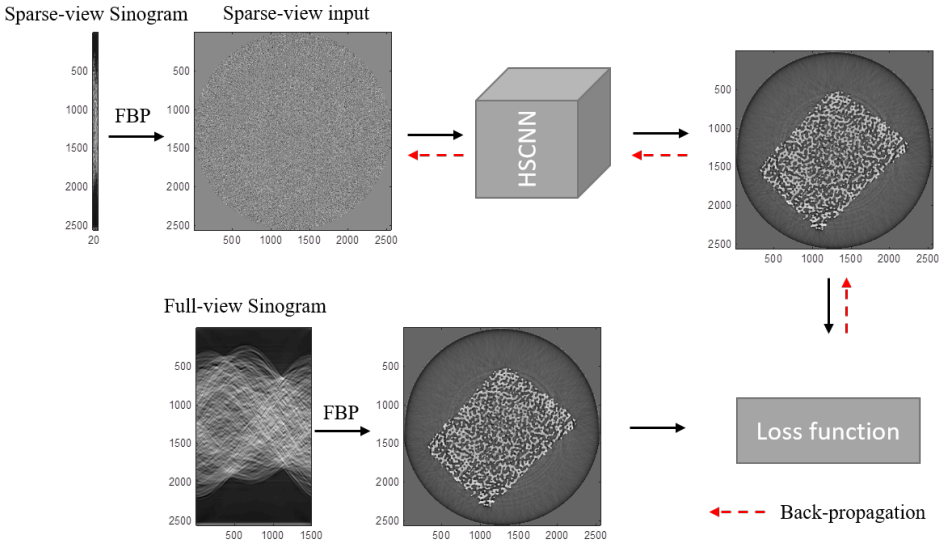

Figure 2.2: Implementation flowchart of proposed HSCNN with sparse-view tomography as an example.

2.3 Results and Discussion

2.3.1 Experimental setup

To investigate the performance of the Hierarchical synthesis CNNs architecture for improving the reconstruction images from limited data, we implemented our proposed method on MATLAB 2018b with the Deep Learning Toolbox. The machine used for our experiments is a PC with Intel Core i7-6700K 4.0-GHz CPU, 32-GB RAM, GeForce GTX 960 2GB GPU.

During each training phase, the Adam optimization method [90] was used to train model with a mini-batch size of one image patch for each iteration. Although the l_2-norm is widely used as the loss function, it may lose details with edge blurring and image structures missing. Here we adopt the l_1-norm as the loss function. The learning rate was selected to be 1×10^{-3} at the beginning and dropped by 1×10^{-2} every 5 epochs. To avoid over-fitting, l_2 regularization term is added with the weight of 0.0005. The validation dataset is used to monitor the network quality during training and provide the stop criterion. In all experiments, the l_1-norm over the validation dataset, i.e., the validation error is computed every 100 gradient steps, and the training is stopped once no improvement to the validation error is found for 1,000 gradient steps. All the parameters in this neural network are initialized using a Glorot initializer [91], which independently samples from a uniform distribution with zero mean and variance $2/(n_{in} + n_{out})$, where n_{in} and n_{out} indicates the number of input and output units in each layer. The overall framework of the proposed reconstruction method based on HSCNNs is depicted in Fig. 2.2. Low-quality images reconstructed from sparse-view measurements and high-quality images reconstructed from full-view measurements are with traditional algorithms, such as Filtered Back-projection (FBP) are fed into the HSCNN as the input and ground truth, correspondingly.

In this study, we compare results of HSCNNs with results generated by popular tomographic reconstruction algorithms including the FBP algorithm with a hann filter, the Simultaneous Iterative Reconstruction Technique (SIRT) [92] with additional box constraints and total variation-based (TV) regularization reconstruction method [12]. For each algorithm, we compare the algorithm output image from limited data with the FBP reconstruction from full-view condition, which is used as the ground truth. Three image metrics: the structural similarity index (SSIM) [93], peak signal-to-noise ratio (PSNR) [94], are carried out to quantify the improvement of our proposed HSCNN method. SSIM is a quality measurement

wherein two images are compared based on their structural information and not solely the pixel value. The index range is between zero and one which zero indicates no similarities and one is a perfect structural match between the reconstructed image and ground truth. The term PSNR is an expression for the ratio between the maximum possible value (power) of a signal and the power of distorting noise that affects the quality of its representation. A higher PSNR generally indicates that the reconstruction is of higher quality. In the case of SIRT reconstructions, we report the results for the number of SIRT iterations that resulted in the smallest mean square error (MSE), with a maximum of 2000 iterations. Fast iterative soft thresholding algorithm [95] algorithm is used to find the solution to the objection function. Through it may be a fairer comparison to require the TV method to select its parameters from the training data and evaluate on the testing data, as our proposed algorithm does, we simply select the parameters that optimize the performance on the test image via golden-section search algorithm with a maximum of 500 iterations to find the optimal λ value.

2.3.2 Simulation

We use one simulated phase tomographic data: the foam phantoms under sparse-view and low-dose limitations for evaluation of the proposed method. To generate a foam phantom, 5,000 single-material non-overlapping spheres with varies sizes are randomly distributed in a cylinder space. An example of the resulting object is shown in Fig. 2.3. The simulated object is similar to the real-world foams, which are typically difficult to accurately reconstruct from limited data. Eleven different objects with the size of $256 \times 256 \times 256$ pixels grid are generated by choosing different random seeds, with nine set of objects are used for training, one set of objects is used for validation and the rest one is used as an independent test object. Tomographic projections of the objects are simulated with TIGRE toolbox with

parallel beam [96]. The absorption coefficient is set as $1e-12\mu m^{-1}$ and the phase coefficient is 1000th of the absorption coefficient. The propagation distance from the object to the detector is set as $5e5\mu m$. Each resulting phase projection image is generated with Fresnel algorithms by propagating the intensity variations directly after the object to the detector plane.

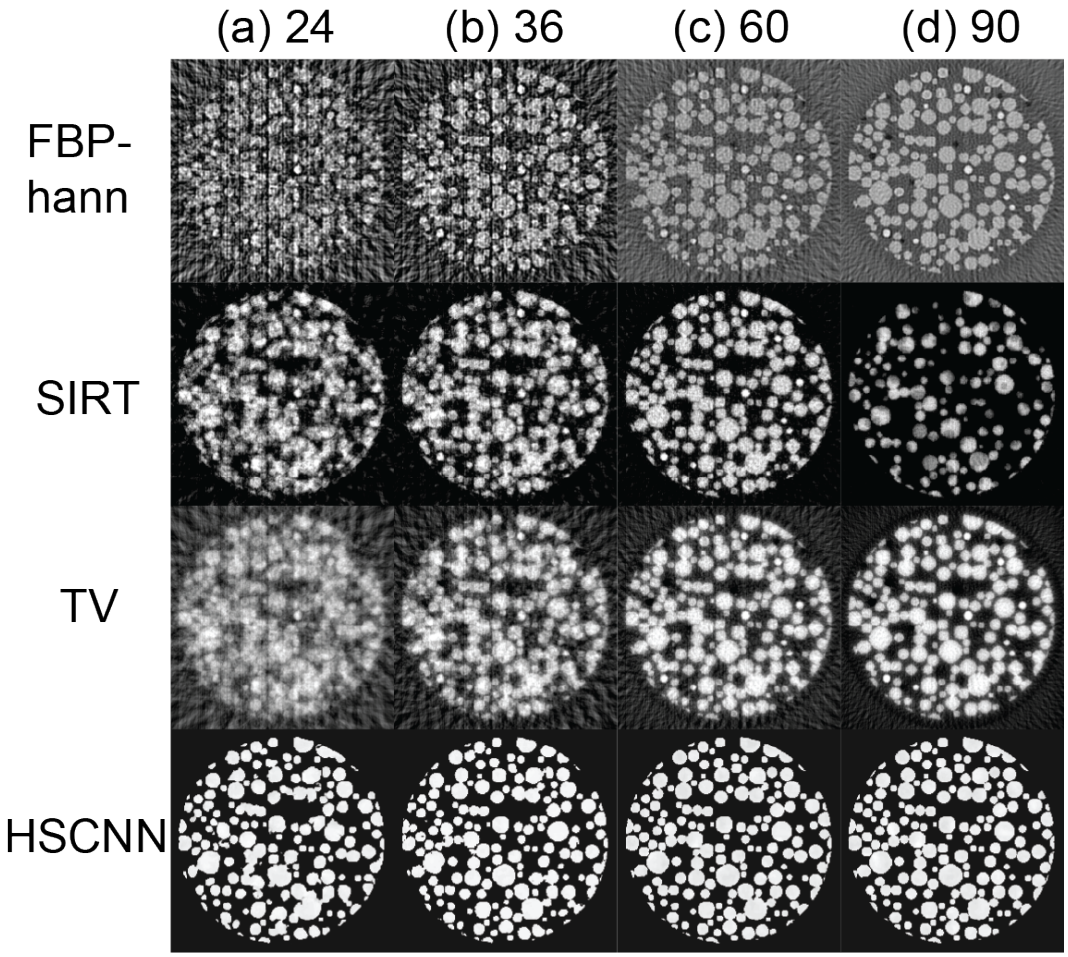

Figure 2.3: Sparse-view tomography reconstruction results of simulated foam data. Four different reconstruction algorithms FBP-hann, SIRT, TV, and HSCNN are implemented for four different number of projection views (a) 24, (b) 36, (c) 60, and (d) 90.

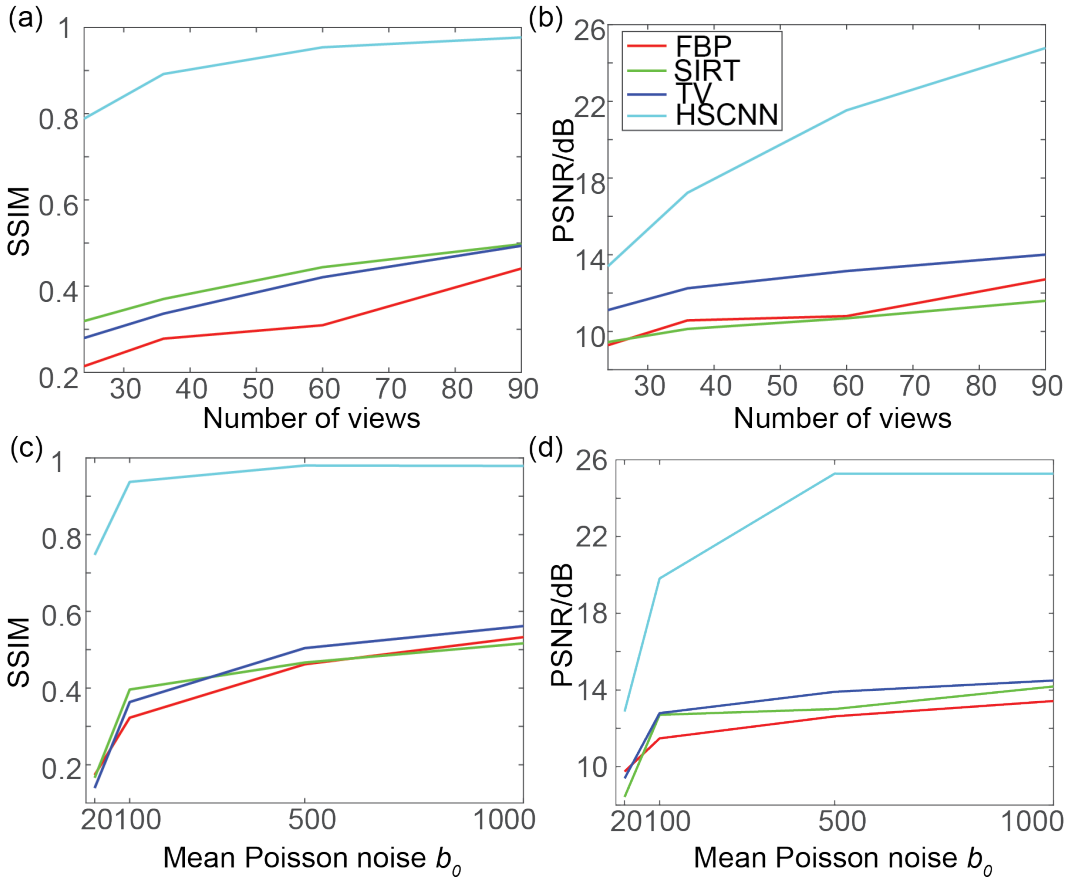

Figure 2.4: Quantitative metrics of sparse-view and low-dose tomography reconstruction results of simulated foam data. (a) & (b) SSIM and PSNR comparison for sparse-view tomography with different number of projections. (c) & (d) SSIM and PSNR comparison for low-dose tomography with different number of projections.

Sparse-view tomography

We first investigate the performance of HSCNN under sparse-view conditions. We train HSCNNs to improve the FBP reconstructions from sparse-view noise-free projections over 180° with FBP reconstructions from 360 noise-free projections over 180° as target images during training. To test the performance of the reconstruction algorithms in various sparse-view-sampling conditions, one slice tomographic image in the testing volume is reconstructed with 24, 36, 60, and 90 projections as shown in Fig. 2.3. We could HSCNN achieves the best visual

results comparing to the rest three algorithms. The quantitative metrics SSIM and PSNR comparison is shown as a function of the number of available projections in Fig. 2.4(a)&(b), which also demonstrates that HSCNN produces images with significantly better error metrics compared with popular tomographic reconstruction algorithms. Compared with the FBP-hann algorithm, our algorithm is able to reduce the number of projections ten-fold without a significant effect in error metric values. Note that even with a highly sparse condition, HSCNN is able to reproduce the general shape of the scanned object.

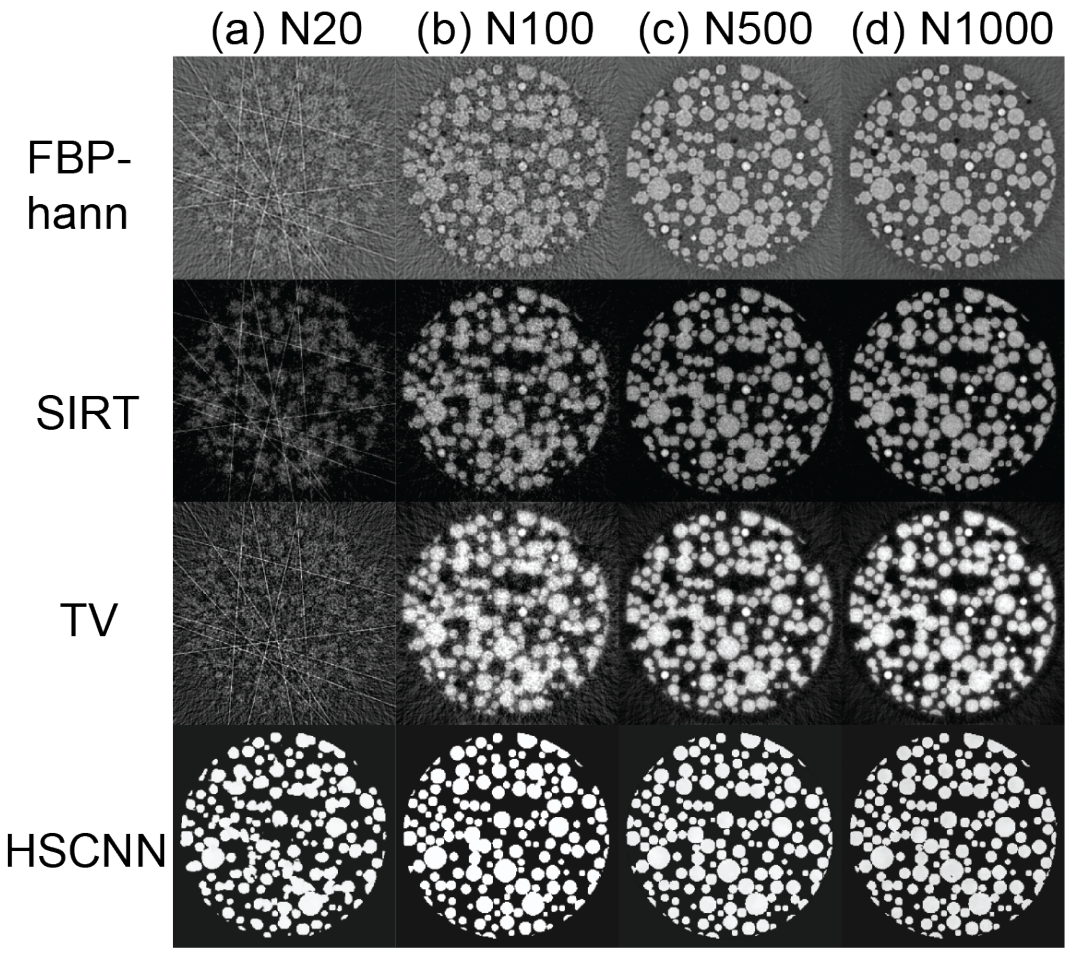

Figure 2.5: Low-dose tomography reconstruction results of simulated foam data. Four different reconstruction algorithms FBP-hann, SIRT, TV, and HSCNN are implemented for four different low-dose cases with b_0 values equal to (a) 20, (b) 100, (c) 500, and (d) 1000.

Low-dose tomography

Next, we investigate the performance of HSCNN under low-dose conditions, where each projection is prone to low X-ray photons and Poisson noise. We train HSCNNs to improve the FBP reconstructions from 360 noisy projections over 180° with FBP reconstructions from 360 noise-free projections over 180° as target images during training. To generate noisy projections, Poisson noise and Gaussian noise are applied to the noise-free projections implemented in the TIGRE toolbox. We use the parameter b_0 controlling mean number of Poisson noise which represents the mean number of photons passing through the object; m and σ^2 denoting the mean and variance of Gaussian noise which representing the mean and variance of the electronic noise respectively. In modern CT systems, m can be immediately determined before each scan and are usually calibrated to be zero. In our simulations, we set the variance of Gaussian noise σ^2 as 10 to represents typical detector noise. We empirically consider four different cases for the b_0 parameters: $b_0 = 20, b_0 = 100, b_0 = 500$, and $b_0 = 1000$ to show the results.

Specifically, the Poisson noise is applied in the following way: first, the noise-free projections were transformed to virtual photon counts using the Beer–Lambert law, with the background photon count set to b_0. For each detector pixel, a new photon count was sampled from a Poisson distribution with the original photon count as the expected value. Finally, the resulting noisy photon counts were transformed back to noisy line integrals of the phantom.

In fig. 2.5, one reconstructed image slice of the testing volume is shown for different low-dose cases, showing the HSCNN is able to produce accurate results even for highly noisy data. The comparison of SSIM and PSNR metrics shown in Fig. 2.4(c)&(d) also demonstrates HSCNN is able to produce images with significantly better quantitative performance compared with traditional algorithms.

2.3.3 Experimental Data

Sea urchin spine

We also apply our proposed HSCNN algorithm to two experiment datasets. One set of experimental data comes from the CT scan of a sea urchin spine sample, collected from the Advanced Photon Source synchrotron at Argonne National Laboratory. One typical slice is shown in Fig. 2.6(a).

To acquire this data, dried specimens of sea urchin spines from one specie (Heterocentrotus mamillatus) were used for the work. Two samples were cut at different locations and scanned using synchrotron X-ray tomography to analyze internal structures. The reconstructions of one sample were used for training and the reconstructions of the other sample were used for testing separately. 1500 projections were acquired with a 2160×2560 pixel detector as the full-view dataset. The acquired data was processed by the TomoPy software package with the phase retrieval performed by phase duality algorithm and reconstructed using the gridrec algorithm. The final reconstructed volume is 2160 2D slices of 2560×2560 pixels per scan.

To make sparse-view images, we uniformly subsampled the sinogram by factors of 10 and 20, which corresponding to 75 and 150 views, respectively. The training is performed using 75 and 150 projections over 180° as the network inputs and reconstructions from 1500 projections over 180° as the training ground truth. We train our network in a patch-by-patch manner because of the limitation of computation memory. 2,000 sparse-view tomography reconstructed image and corresponding target image patches are cropped with the size of 256×256 pixels randomly as the training set in each sparse-view tomography training volume. To produce a validation set, 15% of 2,000 image patches were randomly selected and removed from the training set.

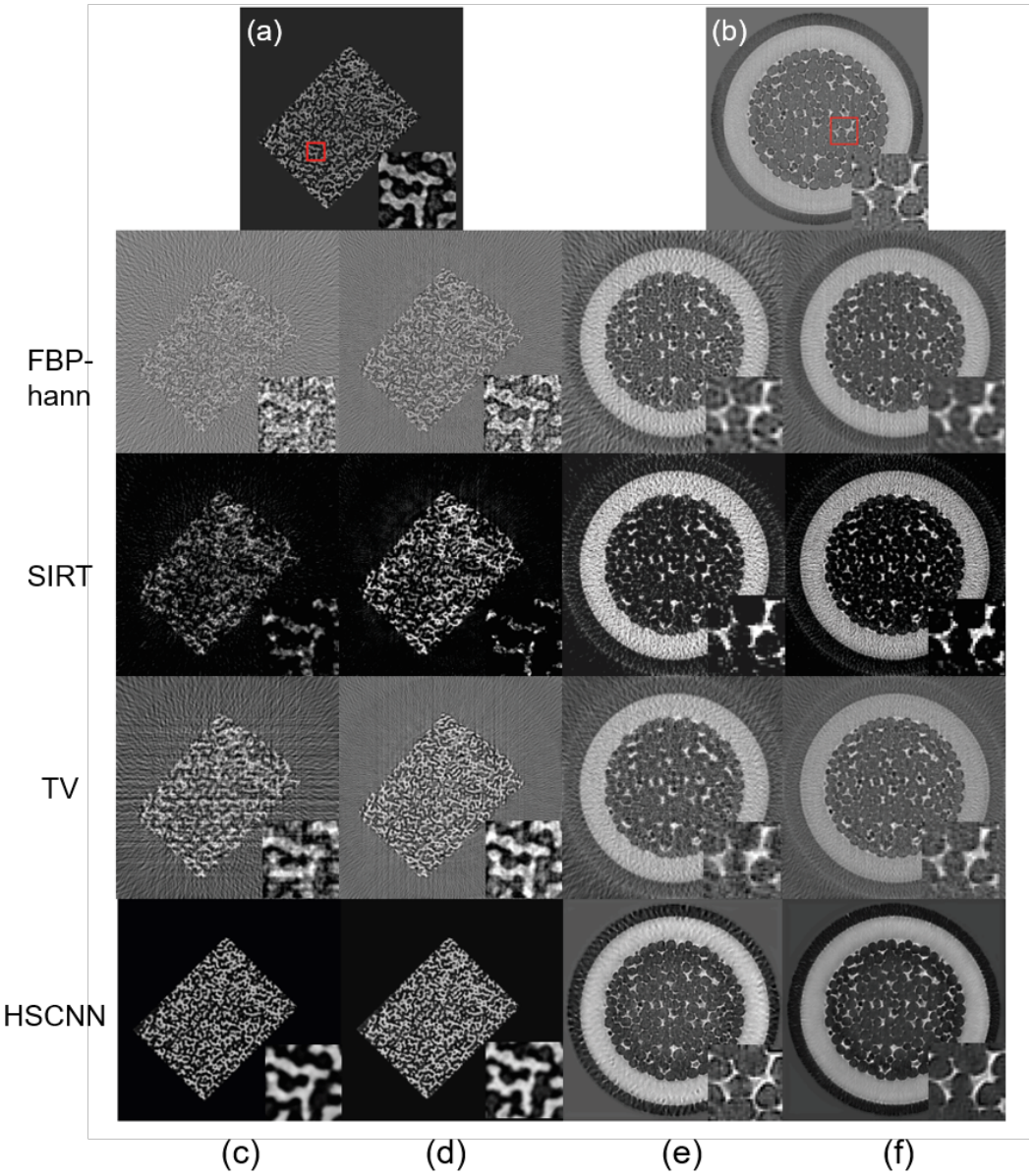

Figure 2.6: Reconstruction performance of experimental data. One typical reconstruction slice of (a) sea urchin spine sample, and (b) foam data from full-view projection acquisition. Reconstruction results from four different reconstruction algorithms: FBP-hann, SIRT, TV, and HSCNN under (c) 75-, and (d) 150-view projection acquisition for the sea urchin spine sample. Column (e) & (f) show the reconstruction results from four different reconstruction algorithms: FBP-hann, SIRT, TV, and HSCNN under 60-, and 100-view projection acquisition for the foam data.

In the first two columns of Fig. 2.6, we show the results of one slice from the tomographic scan of the testing sea urchin spine sample. In the ten-fold sparse-view case, the 1500-views reconstruction result (ground truth) shows nearly artifact-free reconstructed image, while the 150-views reconstruction result shows significant artifacts. Both traditional methods and our proposed algorithm could reduce these artifacts but our proposed algorithm could better preserve fine structures compared to the rest. When the sparsity is increased to twenty times, the artifacts in the sparse-view reconstruction are even more pronounced. We could see the results of traditional methods cannot reduce artifacts efficiently while our proposed method is able to produce the result that has a much better result over results of these traditional method, though retrains slight artifacts.

Foam data

Another set of data is the CT scan of foam data from TomoBank [97], which are complex cellular systems acquired at the TOMCAT beamline of the Swiss Light Source using the fast acquisition [57]. Artifact free tomographic reconstruction are required to quantitatively understand their time-dependent properties, such as deformation fields of bubbles. Fig 2.6(b) shows one typical slice. In the experiment, X-ray projections of the liquid foam flowing through a constriction and being rotated around the tomographic axis are acquired. 130 tomographic scans were acquired in this process. In each scan, 300 projections were recorded, processed with the TomoPy software package [98], and reconstructed using the gridrec algorithm. With binning size setting to 3, 223 2D slices of 252×252 pixels are reconstructed per scan. For training, we used reconstructions of five tomographic scans (1300 slices in total), which are 1st, 10th, 90th and 100th scan. To produce a validation set, 100 slices out of the 1300 available slices were randomly selected and removed from the training set. The middle tomographic scan, 75th scan, is used as the testing set. To make sparse-view images,

we uniformly subsampled the sinogram by factors of 3 and 5, which corresponding to 100 and 60 views, respectively. The network training is performed using 100 and 60 projections over 180° as the network inputs and reconstructions from 300 projections over 180° as the training ground truth. The network is trained based on the whole reconstructed image slice.

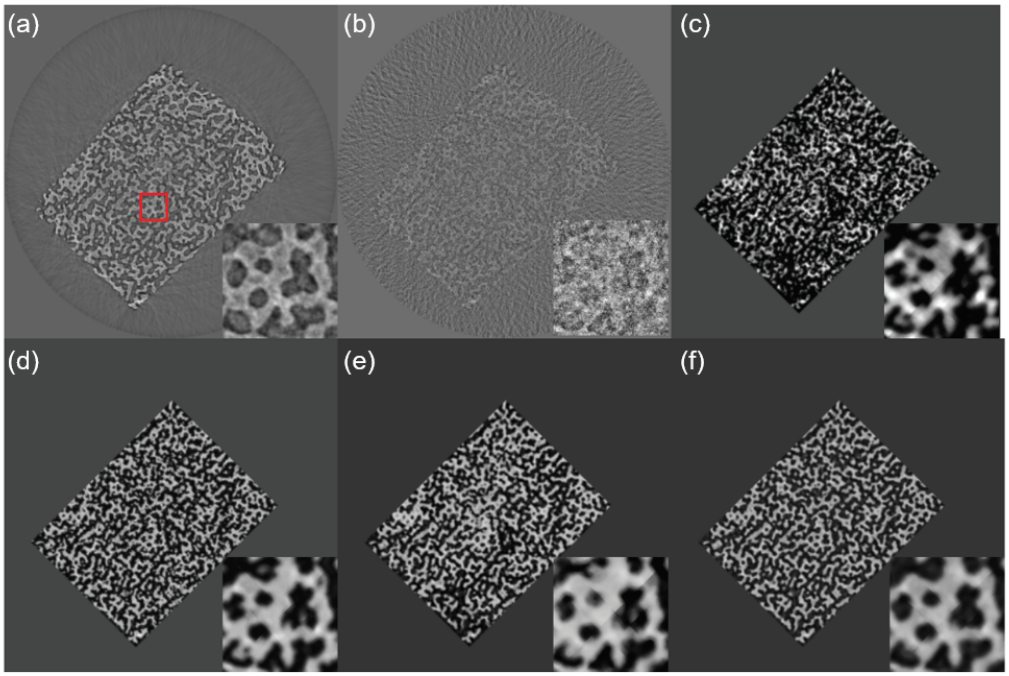

Figure 2.7: Reconstruction results from different splitting strategies. (a) Ground truth reconstructed from full-view (1500) projections, and (b) noisy reconstruction from sparse-view (75) projections, and improved reconstructions from (c) no-splitting, (d) splitting in the intensity domain, (e) splitting in the spatial-frequency domain, and (f) splitting in both intensity and spatial-frequency domain strategies. Zoom-in regions of each method are embedded in each subfigure.

The last two columns of Fig. 2.6 show the results of one slice of the testing foam data with 60 and 100 projections. We could tell that even the ground truth is pretty noisy (Fig. 2.6(b)), our results with HSCNN algorithm demonstrate great improvement with clear boundary for the foams. Our method also shows dramatic improvement compared to traditional SIRT, and TV-based iterative algorithms.

Table 2.1: Quantitative metrics comparison among different splitting strategies.

Metrics/Method	Sparse (75)	No-splitting	Intensity-Only	Spatial-frequency-Only	HSCNN
SSIM	0.1232	0.6122	0.7260	0.7133	**0.7563**
PSNR	12.6061	15.6082	19.6108	18.6420	**20.1572**

2.3.4 The importance of splitting

Next, we investigate the importance of the splitting. In our proposed algorithm, the splitting is performed in the intensity and spatial-frequency domains where the non-uniform distribution is observed. To show the importance of splitting, we compare HSCNN with three networks which are traditional convolutional neural network without any splitting (plain CNN10), traditional convolutional neural network only with intensity domain splitting (intensity-only CNN10) and convolutional neural network only with spatial-frequency domain splitting (spatial-frequency-only CNN). For fair comparison, we set the number of parameters in these three networks similar to the proposed method. The training is also allowed enough time by setting the same stop criterion. Fig. 2.7(a) and Fig. 2.7(b) show full-view reconstruction and sparse-view (75-views) reconstructions with FBP-hann algorithms. Sparse-view reconstruction result suffers from both the streaking effect and the diffraction edge effect, as well as Poisson noise. As a result, the FBP-based reconstruction is prone to noise and the loss of spectral information in both the low and the high ends. It is thus not surprising that structures are barely visible from untrained reconstruction in Fig. 2.7(b). No-splitting strategy with the deep learning-based reconstruction algorithm in Fig. 2.7(c) and Table 2.1 show great improvement compared to raw reconstruction visually and quantitatively. This dramatic improvement shows the importance to involve learning-based algorithms. Intensity-domain only splitting (Fig. 2.7(d)) and spatial-frequency-domain only splitting (Fig. 2.7(e)) show further improvement compared to no-splitting at all. HSCNN,

nevertheless, provides a high-quality reconstruction in Fig. 2.7(f) with a SSIM of 0.7563 and a PSNR of 20.1572 shown in Table 2.1.

2.3.5 Compare with other learning-based networks

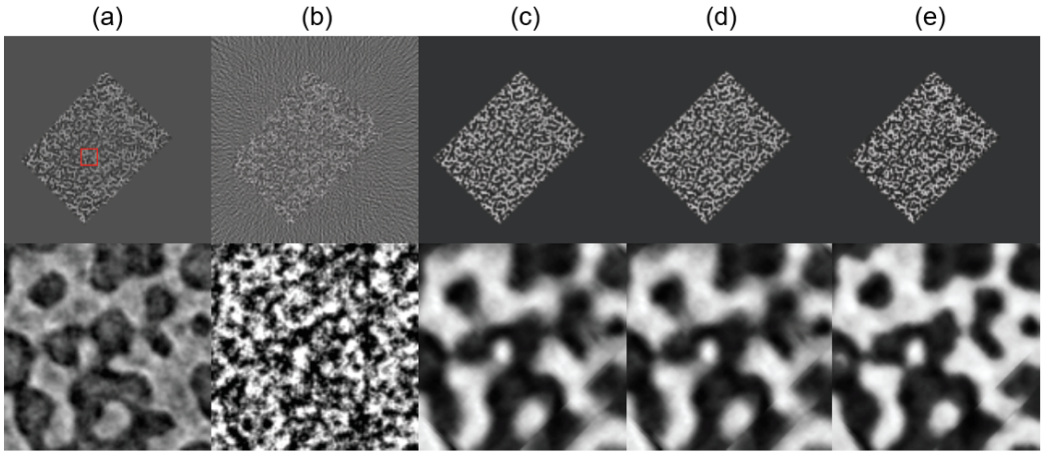

Figure 2.8: Reconstruction results comparison with other learning-based networks. The first column shows (a) ground truth reconstructed from full-view (1500) projections, and (b) noisy reconstruction from sparse-view (75) projections, and improved reconstructions from (c) FBPConvNet, (d) Framing U-Net, and (e) HSCNN. The second column shows the zoom-in regions of each method in the red area.

In this section,we compare results of the proposed HSCNN with other popular learning-based approaches: FBPConvNet [44] and Framing U-Net [86] with the sea urchin spine dataset under 75-views. The details of FBPConvNet and Framing U-Net were obtained from the original paper. Both algorithms are retrained based on our dataset accordingly. There are around 31 million parameters that have to be learned in these two networks, while HSCNN has around 0.3 million learnable parameters. The training of these two comparison networks are implemented on a PC with Python 3.5, Ubuntu Linux 17.10, 128 GB RAM, Intel Core i9 4.6GHz CPU, and a Nvidia TITAN Xp GPU with 12 GB Memory. The training time was about 1 day and 8 hours, respectively.

Table 2.2: Quantitative metrics comparison among different learning-based methods.

Metrics/Method	FBP-hann	FBPConveNet	Framing Unet	HSCNN
SSIM	0.1299	0.5831	0.7352	**0.7563**
PSNR	12.6061	16.4513	19.4911	**20.1572**

As shown in Table 2.2 and Fig. 2.9, best results are generated by our method (HSCNN), while FBPConvNet and Framing U-net methods achieve visionally similar performance. However, a closer review at the fine structures reveals the blurring effects from FBPConvNet. This is caused by the emphasis of the low frequency component of the signal of FBPConvNet. The result of the framing U-Net is improved compared to that of FBPConvNet since a high spectral emphasis is imposed through framing which improves the high frequency recovery, but still inferior to our method HSCNN. This is because the Framing U-Net only considers one level wavelet decomposition. In addition, deep convolutional framelets independently process each sub-band from decomposition perspective which ignores the dependency between these sub-bands. Our method, on the other hand, is capable of dealing with biases in multiple domains in an explicit way, therefore providing better results. Given the simplicity of our proposed method, and the easiness/speed to train and test, our proposed method outperforms all the rest two methods.

2.3.6 Knowledge transferring with HSCNN

We demonstrate the robustness of the training networking in a transfer learning between two different acquisition scenarios (i.e., sparse-view tomography with different propagation distance). By avoiding over-fitting through densely interconnected networks, the trained re-balance synthesis network can be transferred to data with slightly different spectral aberrations in the small scale. As shown in Fig. 2.9(a), the hierarchical synthesis network is first trained by the 75-view sparse-view tomography scan and obtained the network param-

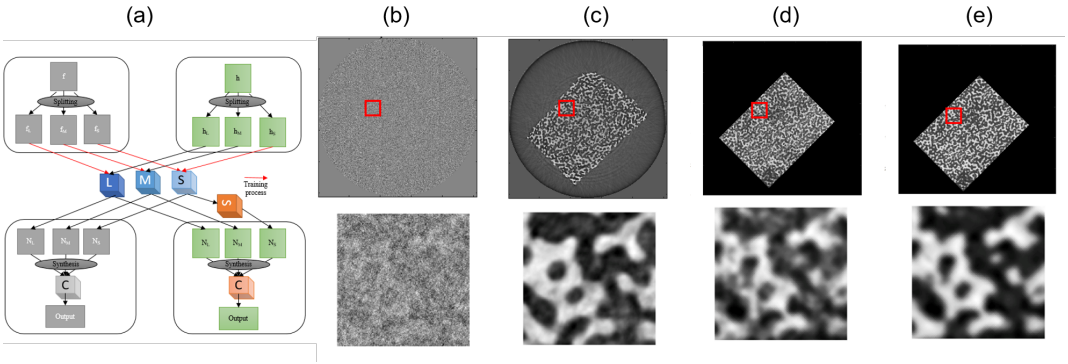

Figure 2.9: Transfer learning results. (a) Knowledge transferring strategy with proposed HSCNN algorithm. (b) noisy reconstruction from sparse-view (75) projections (c) Improved reconstruction based on the same experimental acquisition condition. (d) Directly implement of trained network for new experiment setup with propagation distance change. (e) Transferred learning results.

eters trained in the different scales and synthesis networks. The improved reconstruction result is shown in Fig. 2.9(c) with clear background noise removal and excellent structural information preservation.

When it comes to another experiment setup with slightly propagation distance change, the raw reconstruction from sparse-view (75 views) is shown in Fig. 2.9(b). If directly applied previous trained parameters to this new experiment setup, the improved result is shown in Fig. 2.9(d). Compared to raw sparse-view reconstruction (Fig. 2.9(b)), there are great improvements visually and quantitatively as shown in Table 2.3. However, there are still artifacts and noise in this directly transferred reconstruction result. With the awareness of small-scale features change, we retrained the small scale network *CNN-S* and synthesis network *CNN-C* with 20 slice datasets. This transferring strategy not only avoid retraining the whole three networks and thus reduce the computation complexity, but also reduce the number of training datasets from hundreds to tens of images. Similar high-quality reconstructions are achieved with a SSIM value of 0.7574 and a PSNR value of 17.6160 as a result of transferred learning. This is compared with a SSIM value of 0.6394 and a

PSNR value of 15.9437 obtained by directly transferred. Fig. 2.9(e) shows the final modified transferred result, which demonstrates clear improvement compared to directly transferred result as shown in Fig. 2.9(d).

Table 2.3: Quantitative metrics comparison between different transfer learning strategies.

Metrics/Method	FBP-hann	Direct transfer	Modified transfer
SSIM	0.1299	0.6394	**0.7574**
PSNR	12.6061	15.9437	**17.6160**

2.4 Conclusion

A hierarchical synthesis CNN network architecture is presented to improve X-ray tomographic imaging reconstruction results under insufficient measurement conditions. Based on the prior knowledge of potential biases in the different domains, a split-and-combine strategy is implemented to correct for the non-uniformity in the forward model. In addition, by using a hierarchical synthesis structure, we are able to fuse multi-band information without introducing dense connections across different bands.

Accurate reconstructions are obtained for simulated sparse-view and low-dose tomography, and experimental sparse-view tomography with two different samples, which outperform popular alternative approaches including traditional iterative algorithm SIRT, compressive sensing via TV minimization, FBPConvNet, and framing U-net, in term of image quality and computational speed. Generalizations are possible with biases in more than two domains, and more bands within each domain. This framework provides the possibility for in-situ dynamic 4D imaging to record continuous damage process, which is helpful to study the mechanical properties of cellular structures.

Chapter 3

Measurement-domain data-driven tomographic imaging via Hybrid-dose measurement

3.1 Introduction

Almost all developed methods for low-dose CT reconstruction improvement require a complete set of high-quality ground truth data. However, such high-quality data usually require high-dose acquisition, and is therefore seldom available in applications with a limited X-ray exposure budget, as is the case in dose-sensitive samples and dynamic processes. Recently proposed unsupervised learning processes without high-quality ground truth have achieved good results [99, 100]. However, these approaches require estimation of an additive noise model to correct for the aberrations and noise in the data. In addition, the learned model cannot easily be applied to different samples; the retraining of a new model is needed whenever a new sample or feature is encountered.

We explore here a new approach in which signals from low-dose projections are enhanced during a fast hybrid-dose acquisition, as shown in Fig. 3.1. In this approach, a few low-dose projections are collected together with their corresponding normal-dose counterparts. These

low-/normal-dose image pairs are used to train a mapping of features and noises through a DNN-based learning network; the resulting model is then used to enhance other noisy low-dose projections. This hybrid-dose data acquisition strategy requires only a few normal-dose projections, which dramatically accelerates the acquisition and minimizes dosage on samples. It also simplifies the transfer learning as its easily doable for every sample. Specifically, we make the following contributions in this work:

- We develop a state-of-the-art DNN-based denoising approach in the *measurement domain* to achieve high-quality reconstructions. Our method learns the denoising model from *extremely sparse-view normal-dose projections* and *full-view low-dose projections*. The trained model can be used to enhance and denoise full-view low-dose projections.
- We explore the strategy to distribute dosage smartly with best reconstruction quality. The denoising and reconstruction results are obtained by models learned with different number of low-/normal-dose projection pairs and different dosage value for low-dose projections.
- We evaluate our method on two experimental datasets, and demonstrate that the method can provide excellent projection denoising and reconstruction results. The results also outperform traditional regularization-based reconstruction and deep learning-based denoising approaches in terms of image quality and computational efficiency.

We show that the combination of deep learning with the hybrid-dose acquisition can enable high-quality tomographic reconstructions with low radiation dose. Our method can be applied to other tomographic or scanning based X-ray imaging techniques and has great potential for the study of fast dynamic processes.

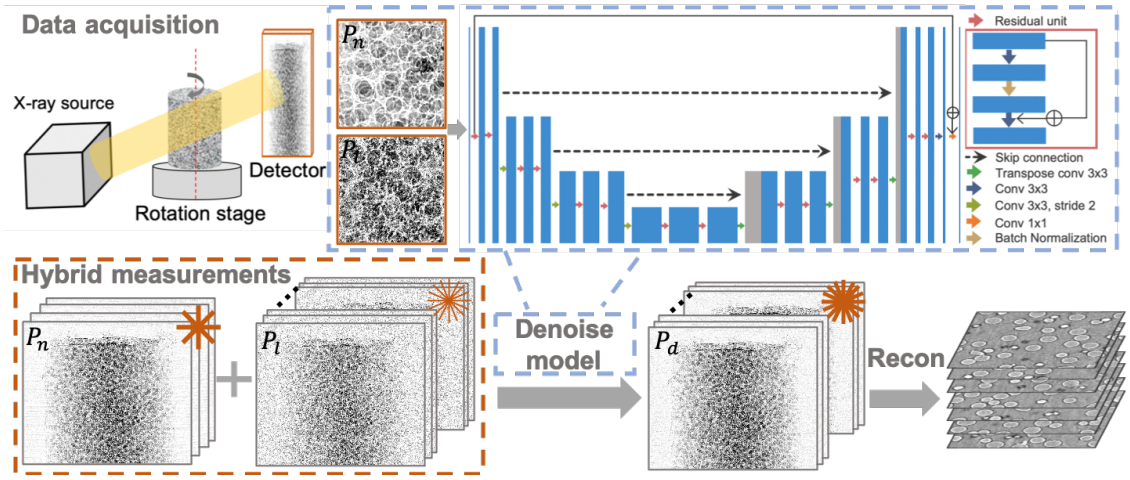

Figure 3.1: The architecture of the proposed deep learning reconstruction framework for low-dose tomography under hybrid-dose acquisition mode (HDrec). Hybrid-dose projections are recorded and corresponding image pairs are extracted to learn the denoising model. Learned model is then applied to full-view low-dose projections to obtain the denoised full-view projections P_d. Finally, image slices are retrieved from the denoised projections via conventional reconstruction algorithms.

3.2 Methods

In this section, we explain our DNN-based denoising method via a hybrid-dose acquisition scheme to improve low-dose tomography reconstructions.

3.2.1 Overview: Feature extraction with hybrid-dose acquisition

Fig. 3.1 shows the proposed DNN-based reconstruction framework for low-dose tomography under hybrid-dose acquisition scheme, which is referred to as HDrec. This framework consists of three parts. First, hybrid-dose projections are recorded including *several extremely sparse normal-dose projections (P_n)* and *full-view low-dose projections (P_l)*. The stars on the top right corner of sub-figures show different acquisition conditions, where the number of total star lines represents the number of total projections and the thickness of each star line represents the dosage value for each projection. Then corresponding image pairs are

extracted from low-/normal-dose projections to train the network. The architecture of the DNN is discussed in the next section. The trained DNN denoising model was then used to enhance the full-view low-dose projections (P_l). Finally, a conventional reconstruction algorithm, such as filtered back-propagation (FBP), is adopted to retrieve images with the denoised projections (P_d).

3.2.2 DNN architecture

Our denoising model uses the state-of-the-art U-Net architecture [101] with residual blocks [102], referred to as *residual U-net*, to facilitate the information flow. As shown in Fig. 3.1, the inputs to the neural networks are the low-/normal-dose projection pairs. The network consists of two principal parts: the image *encoder* and *decoder*. The encoder uses four successive encoding processes to extract features, each containing two residual units, as shown on the top right legend. The residual units have been proven to be efficient in learning noise models for image denoising in computer vision and X-ray tomographic reconstruction applications [103]. The activation function for each convolutional layer is the rectified linear unit (ReLU) [88, 89]. Downsampling operation is usually implemented by the max-pooling operator to reduce the dimension of feature maps and increase the size of the receptive field. It runs fast but some details may be lost in this processing due to the fixed selecting method. Here we replace it with convolution filters with the size of 2x2 and a stride of 2 to learn the downsampling strategy during the training to improve the down-sampling accuracy [40].

The encoded features then pass through three decoding processes to decode the features. Each process is the same as before with two residual units. Deconvolution layers with the size of 3x3 and a stride of 2 are implemented as upsampling layers to increase the dimension of feature maps and decrease the size of the receptive field. Following these three decoding

processes, we use a convolution layer with one kernel and 3x3 kernel size to generate the single channel image and add input to this output, same as the operation in the residual unit. At the end, a convolution layer with one 1×1 kernel generates the single channel image to match the target image. Skip connection is also implemented to avoid resolution loss during the down-sampling process of the encoder in the decoder part of the network. Feature maps generated from transposed convolution layers are concatenated with the preceding feature maps of the same scale from the encoder part.

3.2.3 Objective function

In this section, we present the loss functions used in the residual U-Net, which are the main components to quantify the difference between the noisy input and ground truth. The L2 loss function is usually utilized in CNN training processes, which attempts to minimize the pixel-wise error between the predicted image and the target one. However, the L2 loss yields over-smoothed and blurry images, which results in distortion or loss of structural details. In this work, we combined different loss terms into a hybrid objective function to learn the mapping between low-dose and normal-dose projection pairs.

1) $\boldsymbol{\ell_1}$ ***loss*** is a mean-based metric that encourages the pixels of the output image y to match exactly the pixels of the target image $\hat{y}$. It is similar to the ℓ_2 loss (mean-squared error), but does not over-penalize larger errors between a denoised image and the ground truth as ℓ_2 loss does; this prevents over-smoothness and blurring. The ℓ_1 loss also helps further improve the signal-noise-ratio. In our low-dose CT image denoising task, the ℓ_1 loss function is:

$$\ell_1(\hat{y}, y) = \frac{1}{CWH}\|\hat{y} - y\|_1, \tag{3.1}$$

where $\hat{y}$ and y are the ground truth (normal-dose projection) and a denoised projection,

respectively. C, W, and H are the image width, height, and depth.

2) ***Perceptual loss*** helps to retain texture and structural details of the denoised image by comparing high level differences, like content and style discrepancies, between images. We implement it by calculating the mean squared error of features extracted by a pre-trained VGG network [104]. Specifically, we use the first 16 layers of the pre-trained VGG network to extract the feature representation of a given image. The perceptual loss is defined as the Euclidean distance between the feature representations of a ground truth image $VGG(\hat{y})$ and the corresponding denoised image $VGG(y)$, which is described as follows:

$$l_{VGG}(\hat{y}, y) = \frac{1}{C_f W_f H_f} \|VGG(\hat{y}) - VGG(y)\|_2, \tag{3.2}$$

where C_f, W_f, H_f represent the dimension of the feature maps extracted by the pre-trained VGG network. Parameters in this network are pre-trained with natural images in ImageNet, which also work well to extract features of tomographic images [105].

Overall loss function: We combine ℓ_1 *loss* to ensure pixel identity and *perceptual loss* to keep high-level texture and structural details:

$$l = \alpha \ell_1 + \beta l_{VGG} \tag{3.3}$$

where the coefficients α and β balance these two loss terms, which are decided empirically. In the training stage, the total loss between the output y and a normal-dose projection $\hat{y}$ was calculated for each step and then back-propagated for the neural network optimization. By combining these two loss functions, we insure the quality of refined projection image.

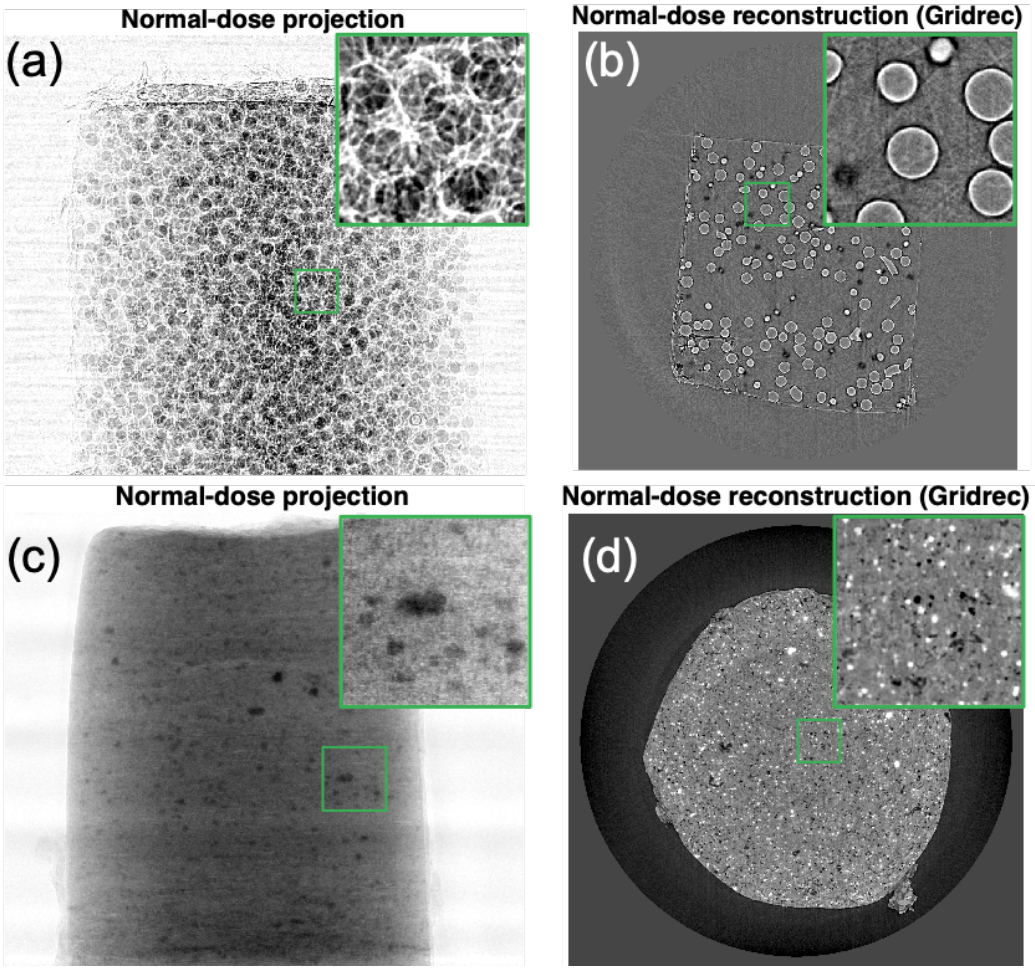

Figure 3.2: Overview of the glass and shale samples. One normalized projection slice for the (a) glass and (c) shale samples. One reconstructed image slice with Gridrec algorithm for the (b) glass and (d) shale sample.

3.2.4 Model training

Our residual U-Net with hybrid loss was trained using image patches with the size of 128×128 extracted from low-/normal-dose projections pairs, then applied on entire full-view low-dose projections. We use different number of projection pairs to explore the relationship between the denoised results and the requirement of normal-dose projections in the result section. For each case, 80% of total low-/normal-dose projections pairs are used for training and the rest are used for validation. We use the adaptive momentum estimation (Adam) to optimize

our residual U-Net with the batch size of 16. We set the learning rate to 1×10^{-4}. with the first moment estimates $\beta_1 = 0.9$ and the second moment estimates exponential decay rate as $\beta_2 = 0.999$ and a small constant for numerical stability as $\epsilon = 10^{-8}$. We implemented the network with Tensorflow.

3.2.5 Tomographic reconstruction

We feed the full-view low-dose projection images P_l into the trained denoising model, as shown in Fig. 3.1, producing full-view high quality denoised projection images P_d. We then perform tomographic reconstruction with the open-source TomoPy toolbox [98], using the Fourier grid algorithm (GridRec) with a Parzen filter to balance reconstruction speed and accuracy. Other tomographic reconstruction methods can also be used.

3.3 Results

We now present the denoising and reconstruction performance of our proposed method when applied to the glass and shale datasets (Fig. 3.2) from TomoBank [97] under different configurations. We used one NVIDIA Tesla V100 SXM2 (32GB memory) GPU card for training, denoising, and reconstruction. We evaluate our proposed methods against a variety of data acquisition schemes and compare our method to the state-of-the-art learning-based algorithm, Xlearn [35], and one iterative total variation-based (TV) regularization reconstruction [12] method both in terms of image quality and computational time requirements.

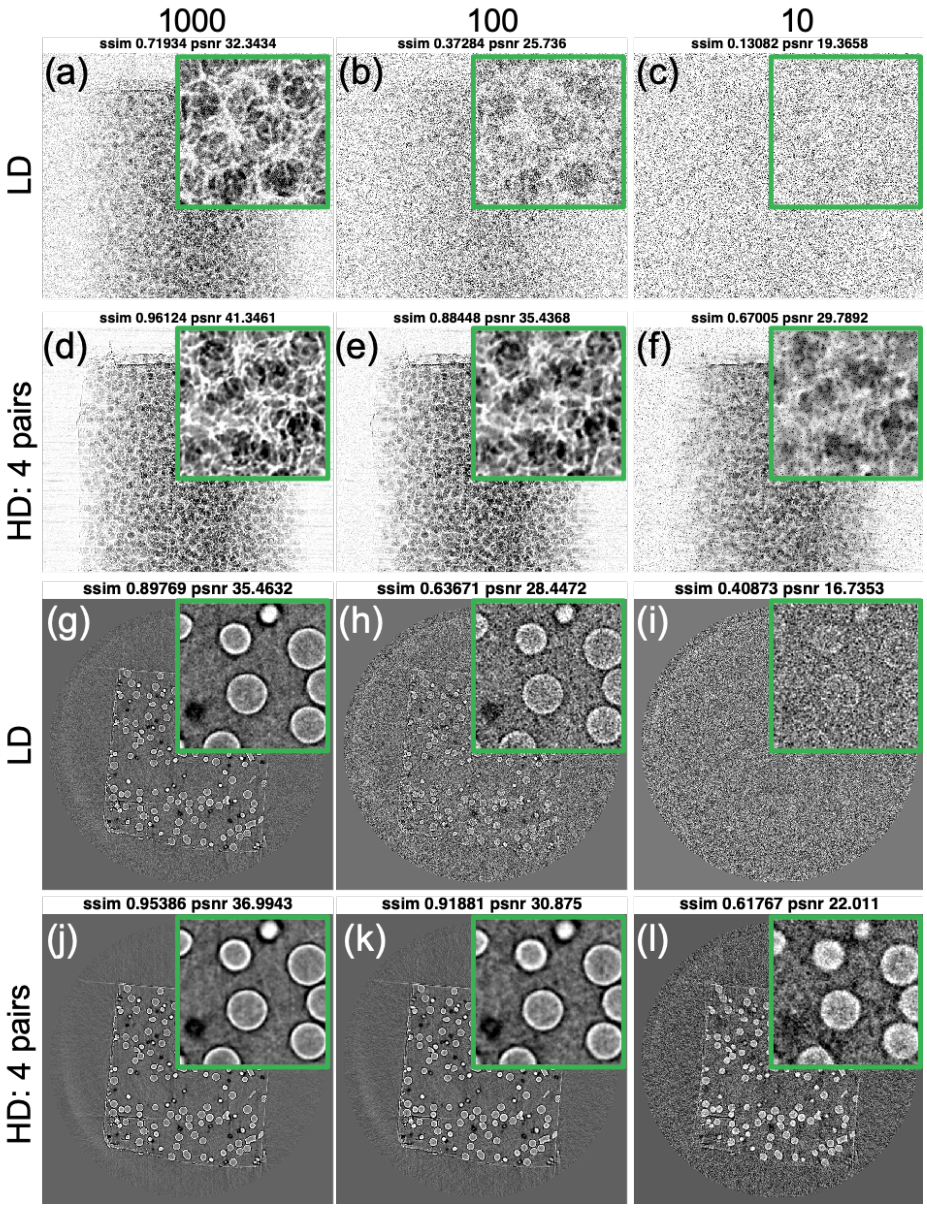

Figure 3.3: Simulated low-dose projections and denoised projections and reconstruction results for the glass sample. The first and third rows show the simulated low-dose projections and reconstruction results with the dosage value of (a, g) 1000, (b, h) 100 and (c, i) 10 per projection. The second and last rows show the denoised projections and reconstruction results enhanced with the models trained with four projection pairs and the dosage value of (d, j) 1000, (e, k) 100 and (f, l) 10 in the low-dose simulations.

3.3.1 Glass sample

The glass sample contains 20% volume fractions of borosilicate glass spheres encased in a polypropylene matrix. It was measured at the 2-BM fast tomography beamline of the Advanced Photon Source (APS), Argonne National Laboratory (ANL). The detector dimension is 2560×2160 pixels with the pixel resolution of $0.65\mu m$. The experiment was performed with source energy of 27.4 keV and exposure time of around 0.0001s as the normal-dose projections P_n. 1500 projections were taken over 180°. Each projection was normalized with white-field and dark-field measurements, which scales the image between 0 and 1 to obtain reliable attenuation information for reconstruction. Fig. 3.2(a) shows one normalized projection in the normal-dose measurements. Multiple bubbles are summed along the X-ray propagation path for each ray path, resulting in the structure overlap. The green box on the top right corner shows the zoom-in structural details. Fig. 3.2(b) shows one reconstructed image slice retrieved from full-view normal-dose measurements with Gridrec algorithm. The reconstructed structures are seen clearly in this figure.

In order to simulate low-dose projections from these normal-dose measurements P_n, we used Siddon's ray-driven forward projection method [106], and added Poisson noise as:

$$P_l \sim \text{Poisson}\{b_0 P_n\}/b_0 \tag{3.4}$$

where b_0 is the blank scan factor representing the dosage value per ray/pixel and P_l is the simulated low-dose detector measurements. No electronic readout noise was simulated. The dosage reduction ratio of simulated low-dose measurements can be adjusted by setting the number of photons per projection for the blank scan factor b_0. In the glass sample, the average number of photons for normal-dose projections per pixel is measured to be around 5000. For simplification, we use 5000 to represent the number of photons received per

projection for each normal-dose projection. Low-dose projections are simulated with Eq. 3.4 by setting $b_0 = 1000$, 100, and 10 as the lower dosage values compared to the dosage of normal projections. We use the Structural Similarity Index (SSIM) and Peak signal-to-noise ratio (PSNR) to quantify the structural similarity and noise level compared to original normal-dose projections. As shown in Fig. 3.3(a–c), the SSIM of simulated projections decreases with decreasing dosage per projection, and consequently the structural details become more difficult to distinguish.

Denoising models are trained with simulated low-dose and experimentally measured normal-dose projection pairs to enhance the full-view low-dose projections P_l and thus obtain the denoised projections P_d. Fig. 3.3(d–f) show the denoised projection results P_d with four different low-/normal-dose projection pairs at 0°, 45°, 90°, and 135° with the dosage value of low-dose projections b_0 equals to 1000, 100, and 10. Denoised projections P_d (Fig. 3.3(d–f)) demonstrate significant noise reduction and structural details improvement compared to the corresponding low-dose projections P_n (Fig. 3.3(a–c)). This is also validated with improved SSIM and PSNR values that the SSIM value of final denoised projection slice (Fig. 3.3(d)) for dosage value of 1000 is improved from 0.72 to 0.96 and PSNR value is improved from 32.34 to 41.35 by using the denoising model trained with 4 normal-dose and low-dose projection pairs. These improvements are even more significant for the projections from lower-dosage cases. For the low-dose projections with dosage values of 100 and 10, it is difficult to distinguish the structures of the glass phantoms with very low SSIM and PSNR values. By using the denoised models, the denoised projections (Fig. 3.3(e, f)) are significantly improved.

We also compare the denoised projection performance under more hybrid-dose acquisition schemes in terms of SSIM and PSNR values to explore the influence of different number of low-/normal-dose projection pairs. Fig. 3.4(a, b) depict SSIM and PSNR values in terms of mean and standard variation for the denoised projections enhanced with 4, 32, 128, and 256

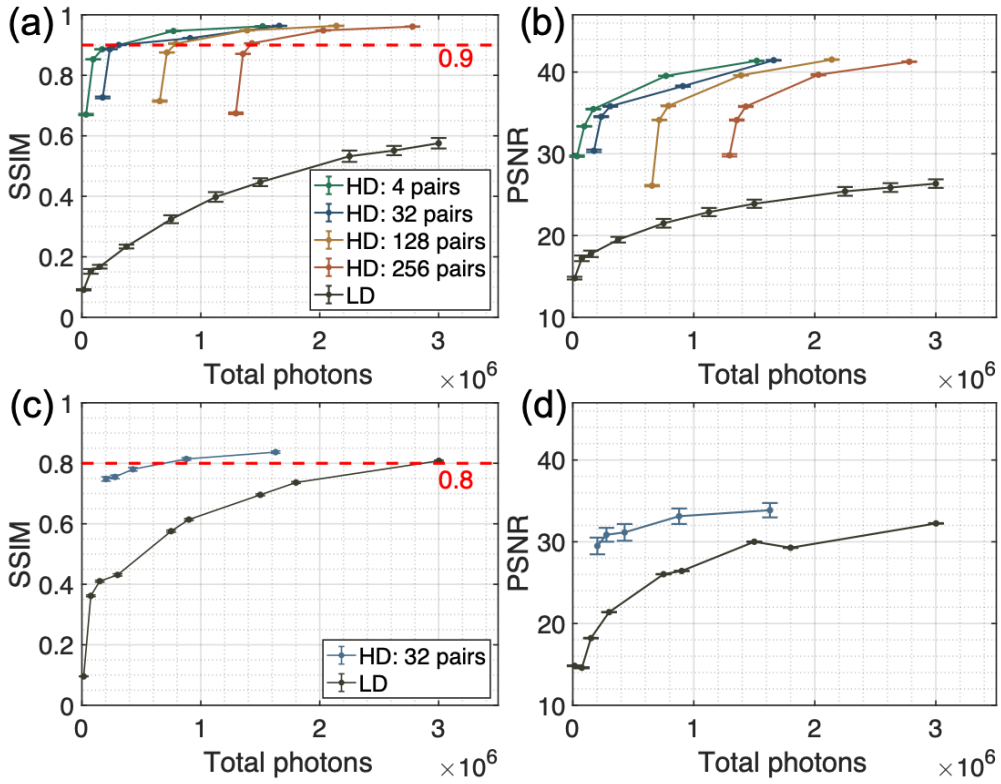

Figure 3.4: SSIM and PSNR distribution with respect to the number of total photons under each configuration for the (a, b) glass and (c, d) shale sample. Green, blue, yellow, and orange lines in (a, b) denotes the performance of enhanced projections with different number of low-/normal-dose projection pairs (4, 32, 128, and 256). Five dots on each line represent different dosage values b_0 = 10, 50, 100, 500, 1000 for corresponding low-dose projections. Blue line in (c, d) denotes the performance of enhanced projections with the models trained with 32 low-/normal-dose projection pairs. Five dots on each line represent different dosage values b_0 = 50, 100, 200, 500, 1000 for low-dose projections. Black line represents the performance of pure low-dose projections.

low-/normal-dose projection pairs, shown in green, blue, yellow, and orange lines, respectively. Five dots on each line represent the given dosage values of low-dose projections b_0, which are 10, 50, 100, 500, and 1000 respectively. We calculate the total photons for each configuration as x label by summing up all required sparse-view normal-dose and full-view low-dose projections. By comparing these four lines under different hybrid-dose acquisition modes, we could conclude that more projection pairs don't improve the projection enhance-

ment performance. On the contrary, the least low-/normal-dose projection pairs, which is four projection pairs in our study, always performs the best in terms of SSIM and PSNR values. We also calculate SSIM and PSNR values of low-dose projections under uniformly distributed acquisition modes. Ten different dosage values per projection are simulated with respect to the total photons and treat as the baseline, shown as the black line in figure 3.4(a, b). The performance of non-hybrid measurements (black line) is consistently worse than that of the denoised projections with the network enhancement (green, blue, yellow and orange lines) under the fixed number of total photons. In other words, when the number of total photons is limited, uniformly distributing the total photons to each projection can results in mediocre or sub-optimal projection quality. As empirically shown, it is better to concentrate the photon budget to the few normal-dose projections, and uniformly distribute the rest as low-dose projections.

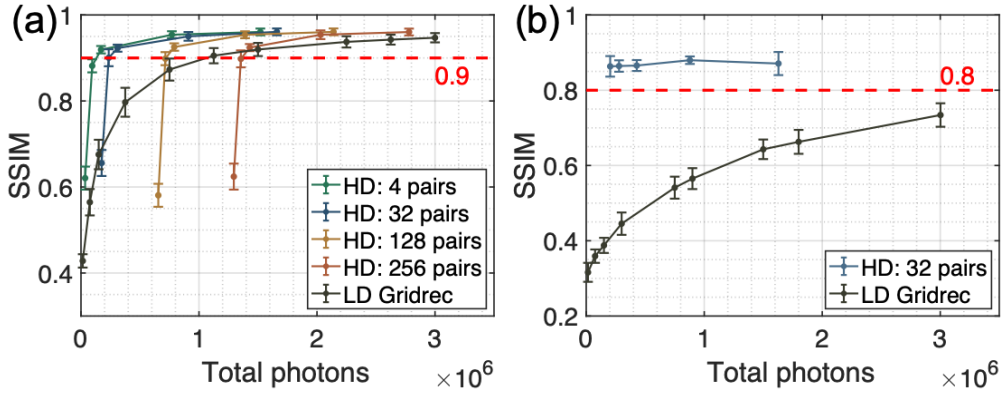

Figure 3.5: SSIM distribution of reconstructed slices with respect to the number of total photons under different hybrid-dose acquisition schemes for the (a) glass and (b) shale sample. Green, blue, yellow, and orange lines in (a) denotes the performance of enhanced projections with four different number of low-/normal-dose projection pairs (4, 32, 128, and 256). Five dots on each line represent different dosage values $b_0 = 10$, 50, 100, 500, and 1000 for low-dose projections. Blue line in (b) denotes the performance of enhanced projections with the models trained with 32 projection pairs. Five dots on each line represent different dosage values $b_0 = 50$, 100, 200, 500, and 1000 for low-dose projections. The black line represents the performance of pure low-dose projections.

Next, we study the reconstruction results from full-view normal-dose projections P_n, full-

view low-dose projections P_l, and their corresponding *denoised* versions P_d. Fig. 3.2(b) shows the the tomographic reconstructions from P_n, whereas Fig. 3.3(g–i) and (j–l) illustrate reconstructions from P_l and their corresponding *denoised* versions P_d, respectively.The SSIM value of the final reconstruction slice for the dosage value of 1000 (Fig. 3.3(j)) improves from 0.90 to 0.95. These improvements are more significant for the the reconstructions with lower-dosage values. For the reconstruction results based on low-dose only measurements with dosage of 100 (Fig. 3.3(h)) and 10 (Fig. 3.3(i)), it is difficult to distinguish the structures of the glass phantoms with very low SSIM values. The final reconstructions (Fig. 3.3(k, l)) from enhanced projections with corresponding trained models are improved significantly in terms of visual quality and quantitative SSIM value.

We also compare the mean SSIM values of the final reconstruction volume performance (Fig. 3.5(a)) to explore the influence of different number of normal-dose and low-dose projection pairs and how to distribute the total X-ray photons. We could tell there are some differences between Fig. 3.4(a) and Fig. 3.5(a). Final reconstruction from the learned denoising models with a few normal-dose projections outperforms the results from uniformly distributed projections. The two points beneath the black line are reconstruction results from the models trained with 128 and 256 low-/normal-dose projection pairs, and the low-dose projection dosage values b_0 are set to 10 and 50, respectively. When we compare the SSIM performance under the fixed photon budget, the points on green line and blue line significantly outperform these other two configurations. They are also better than the black line which represents the uniformly distributed dosage in non-hybrid measurements. These points on the green and blue lines represent the performance of reconstruction results trained with 4 and 32 low-/normal-dose projection pairs and the low-dose projection dosages b_0 are around 500 and 1000, respectively. This is because if the dosage value of projections is too low, the structural details are smeared by the noise. Simply adding more normal-dose pro-

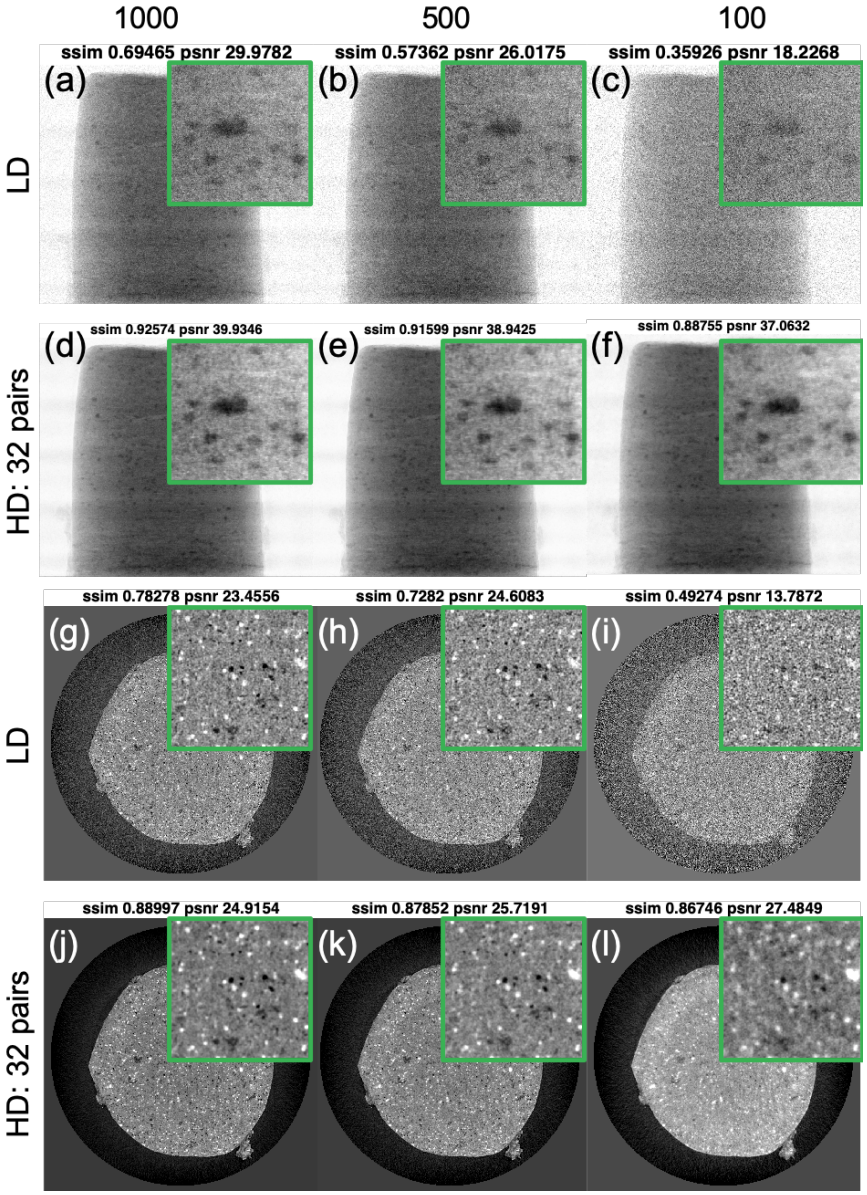

Figure 3.6: Projection and reconstruction performance of full-view low-dose measurements and heir corresponding denoised versions for the shale sample. The first and third rows show the simulated low-dose projections and reconstruction performance with the dosage value of (a, g) 1000, (b, h) 500 and (c, i) 10 per projection. The second and last rows show the denoised projections and corresponding reconstructions enhanced with the models trained with 4 low-dose and normal-dose projection pairs and the dosage value of (d, j) 1000, (e, k) 500 and (f, i) 100.

jections doesn't improve the structural restoration. In other words, when the total photon budget is fixed, it is better to distribute the photons to fewer normal-dose projections, and uniformly distribute the rest with not-too-low dosage value for each projection.

3.3.2 Shale sample

We further validated the proposed method on a second experimental dataset of the shale sample with significant different structural features. Shale is a challenging material as its multi-phase composition, low but significant amount of porosity, small grain size, and strong shape- and lattice-preferred orientation. In this work, we use a shale sample dataset from the Upper Barnett Formation in Texas [107]. Micro-CT measurements of the shale sample were also acquired at APS. We used 1501 projections acquired over 180° at APS as the normal-dose projections. Fig. 3.2(c) shows one normalized projection in the normal-dose measurements. Multi-phase compositions are summed up along the X-ray propagation path for each ray path, resulting in the structural overlapping. Fig. 3.2(d) shows one reconstructed image slice retrieved from full-view normal-dose measurements with Gridrec algorithm. The average number of photons for normal-dose projections per pixel is measured to be around 4000. We simulate the low-dose projections from these normal-dose measurements according to Eq. 3.4.

Figs 3.6(a–c) and 3.6(g–i) show simulated low-dose projections and corresponding reconstructed image slices for low-dose projections with blank scan factor $b_0 = 1000$, 500, and 100. Grain structures are smeared by the noise with the decreased dosage value per projection in the low-dose measurements, which is also validated with the SSIM and PSNR of simulated projections and SSIM of reconstructed image slice.

Similar to the glass sample, we trained the residual U-Net to estimate the high-resolution

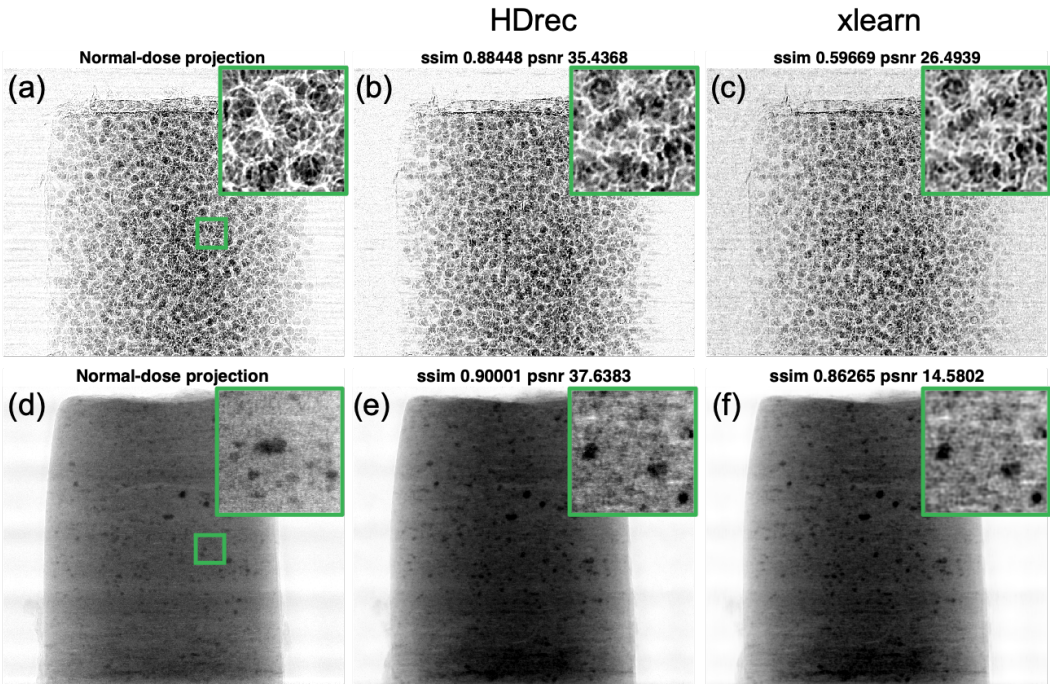

Figure 3.7: Projection denoising performance comparison with Xlearn for the (a–c) glass and (d–f) shale sample: (a, d) normal-dose projections, (b, e) denoised projections with our method, HDrec; (c, f) denoised projections with Xlearn.

measurements (P_n) when provided with full-view low-dose projections P_l ($b_0 = 1000, 500, 10$) with 32 low-/normal-dose projection pairs. The second row of Fig. 3.6(d–f) and Fig. 3.6(j–l) show the denoised projections P_d and reconstruction results enhanced by the denoised models. Denoised projections P_d could remove the noise significantly and improve the structural details compared to corresponding low-dose projections P_l, shown in Fig. 3.6(a–c). Tomographic reconstructions (Fig. 3.6(j–l)) of corresponding denoised full-view projections also show improved structural restoration, which is also validated with the SSIM values.

We also plot the SSIM and PSNR values of projection slices (Fig. 3.4(c, d)) and SSIM values of reconstructed slices (Fig. 3.5(b)) vs. number of total photons for each configuration. The performance of uniform distributed low-dose measurements (black line) is again consistently worse than that of the denoised projections with network enhancement (blue line) under a

fixed number of total photons, which is consistent with the glass sample results. This result again shows that it is better to concentrate photons to a few normal-dose projections and uniformly distribute the rest as low-dose projections.

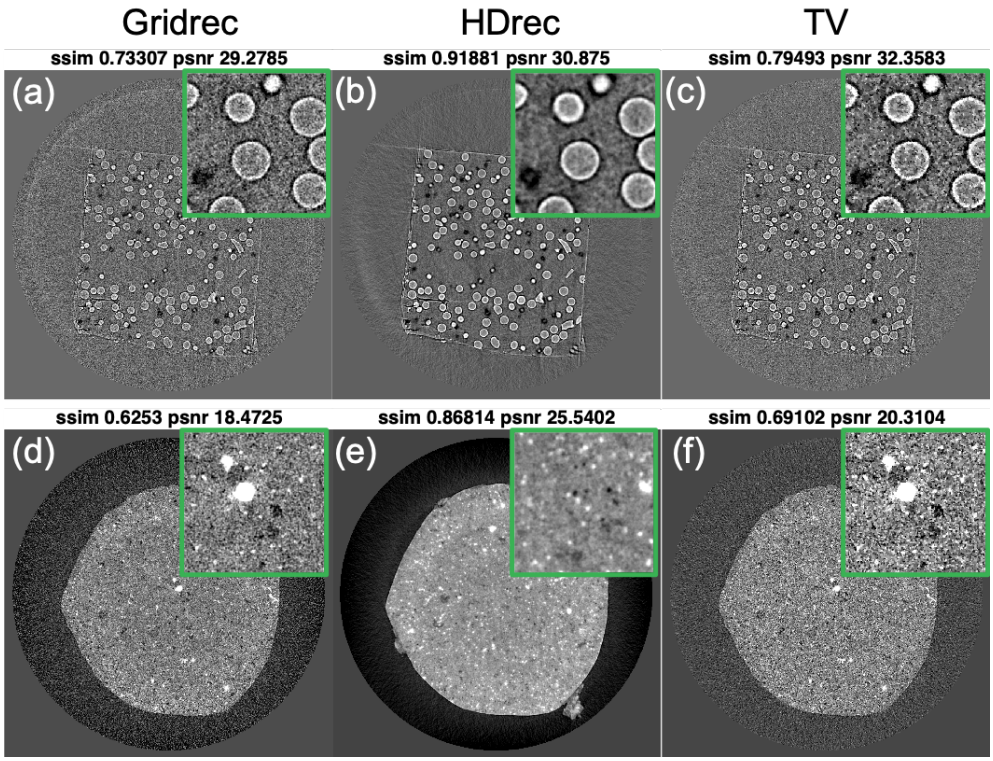

Figure 3.8: Reconstruction performance comparison with total variation-based regularization method for the (a–c) glass and (d–f) shale sample. (a, d) Reconstruction results with Gridrec for low-dose projections of same number of total dosage as hybrid-dose measurements. (b, e) Reconstruction results with Gridrec for denoised projections. (c, f) Reconstruction results with TV-based method for low-dose projections of same number of total dosage as hybrid-dose measurements.

3.3.3 Projection denoising performance comparison with Xlearn

We compare the denoised projection results against a previously proposed learning-based method, Xlearn [35]. This comparison method was originally trained with several low-/high-dose projection pairs and applied to whole low-dose measurements. For fair comparison with

our case, we use the same network architecture and training strategies as Xlearn and retrain for the low-/normal-dose projection datasets used in this work. As shown in fig. 3.7, our method achieves better structural restoration and noise removal performance compared to Xlearn.

3.3.4 Reconstruction performance comparison with total variation-based regularization method

We also compare reconstruction image quality with that obtained via the iterative total variation-based (TV) regularization reconstruction method. We show the reconstructed results (Fig. 3.8(b, e)) generated by the denoising model trained with 32 low-/normal-dose projection pairs and low-dose dosage values of 100 and 200, respectively. For a fair comparison, we simulate the uniform distributed low-dose projections using the same total dosage as for HDrec: 206 and 285 per projection for glass and shale, respectively. The Gridrec (Fig. 3.7(a, d)) and TV-based (Fig. 3.7(c, f)) reconstructions for the glass and shale samples are worse than those obtained with HDrec, both qualitatively and quantitatively.

Table 3.1: Computation time comparison

	HDrec	xlearn	TV
Single projection denoising	**1.34**	550	-
Single image reconstruction	**0.86**	**0.86**	55.79

3.3.5 Computational time comparison

We use the glass sample to show the computational costs of HDrec, the Xlearn-based projection denoising method, and the TV-based iterative reconstruction method, as shown in Table 3.1. All methods are run under the same computer configuration. The comparison is

based on:

1) *Single projection denoising*: HDrec's use of a fully convolutional neural network allows it to complete in 1.34s: 410 times faster than the 550s taken by Xlearn.

2) *Reconsructing a single image*: For HDrec and Xlearn, this requires the application of gridrec to denoised projections (around 0.86s for a single image); for TV-based iterative reconstruction, only the reconstruction operation is needed to obtain the final image slice, with average time of around 55.79s.

3) *Total time from denoising of projections to reconstruction*: For a complete dataset, it takes around 1 hour, 9.5 days, and 17 hours for HDrec, Xlearn, and the TV-based method, respectively, corresponding to speedups of 214 and 16 for HDrec over Xlearn and the TV-based method, respectively.

3.4 Conclusion and Discussion

We have presented a deep learning-based enhancement method, HDrec, for low-dose tomography using hybrid-dose measurements, which contains *extreme sparse-view normal-dose projections* and *full-view low-dose projections*. The denoised projections and reconstructed slices show significant improvement when compared to Xlearn-based projection denoising and TV-based reconstruction methods in terms of image quality and computational efficiency. In addition, we provide a strategy to distribute dosage smartly with improved reconstruction quality. With a limited dosage budget, the strategy of fewer normal-dose projections in combination with the not-too-low full-view low-dose measurements greatly outperforms the uniform distribution of the dosage.

Chapter 4

Application to damage characterization of bio-cellular sea urchin spine structure

4.1 Introduction

Cellular materials represent an important class of materials that offer supreme functional properties with minimum densities [108, 109]. In particular, natural cellular solids exhibit remarkable damage tolerance behaviors that far exceed their brittle solid counterparts, inspiring explorations on the imitation of graceful degrading [64, 110, 111]. Understanding the damage behaviors is a fundamental challenge in biocellular materials science and relevant to a broad range of energy absorption and impact shielding applications. These ubiquitous phenomena emerging from natural evolution lies at the heart of biomicic structural material design, offers damage tolerance mechanisms across hierarchical length scales that remains to be revealed. There is a strong belief that the damage tolerance properties are correlated with the 3D structure of the cellular network. However, damage behaviors characterization has been conventionally performed based on 2D histological sections with few representative slices and lab-based micro-computed tomography with low-spatial resolution as discussed in section 1.4. Recently, synchrotron-based X-ray tomography have provided major insight

into volumetric information with enhanced spatial resolution.

Damage features captured with current damage characterization techniques often rely on tedious and observer-dependent manual labeling to exclude the complex structural background[112, 113]. The labeling process is further complicated by the multiple simultaneous failure features in cellular materials, involving struts bending, buckling, fracturing and fragmentation, and etc. [114, 115, 116] More importantly, many recent researches suggest that natural cellular materials demonstrate multi-scale damage-resistant mechanism, ranging from individual struts damage, crack propgation among clustering of chains, formation of densified bands to the global network failure [117, 118, 119]. Registration of damage behaviors to the network hierarchy is therefore needed to replace the stochastic description used for homogenous random porous architectures. The desired holistic 3D registration of multiple damages to the cellular structure inevitably involves challenges to deal with huge amount of volumetric analysis that cannot possibly implement manually. An automatic, general approach directly applicable to 3D data is thus crucial and highly desirable to obtained quantitative and holistic damage information, which is ultimately required for the understanding and engineering of damage tolerance through 3D cellular structural design.

Fortunately, recent advances in deep learning dramatically improves the accuracy and efficiency of automatic computer vision-based analysis. A few recent researches have also explored using machine learning for damage characterization on pavement, bridge concrete and metal alloys [120, 121, 122]. However, these learning-based methods have been mainly applied to 2D images, and the characterized damages are sparsely presented on a solid background with minor noise or texture, thus are insufficient for the complexity of cellular damages. In addition, extending the framework of 2D learning to 3D data is not simply the routine of stacking 2D slices together, which can be impacted by slice orientation and stark effects [65]. A fast, general, reliable and accurate way to identify and analyzing damages in

3D cellular materials is still elusive.

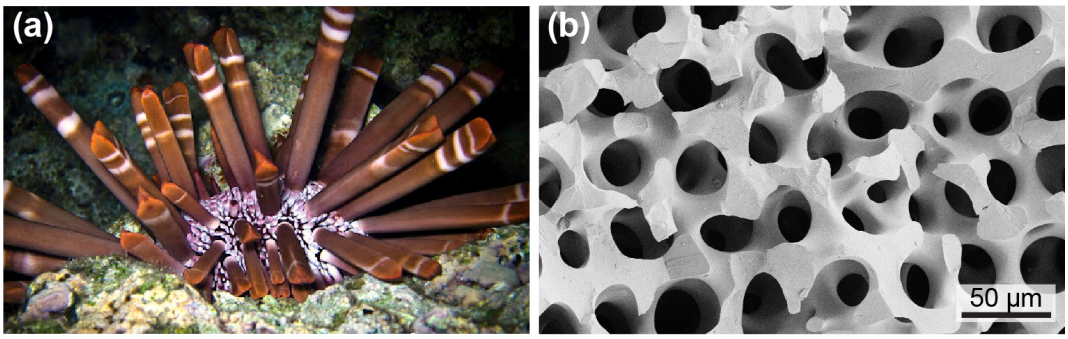

Figure 4.1: The cellular structure from the spine of the sea urchin Heterocentrotus mamillatus used in this work. (A) Photograph of a live H. mamillatus sea urchin (Image credit, Eric Noora). (B) Scanning electron microscopic (SEM) image of the biomineralized cellular structure.

In this work, we implement an in-situ synchrotron-based X-ray tomography to enable a high-resolution recording of damage evolution over a large spatial-temporal span for 3D cellular samples. Deep learning-based pattern recognition, 3D computer vision and cellular microstructure network representation are integrated to enable rapid automatic damage behaviors detection and quantitative analysis. Damage structures across multiple length scales, embedded in the complex cellular network, are recognized efficiently and accurately with deep learning-based algorithms by involving neighboring CT slices as semi-3D damage detection. The spatial correlations among 2D slices in different orientations and between adjacent parallel slices are incorporated to extract multi-scale features for local classification and global segmentation. Final damage regions are identified by combining detection results from three orthogonal views to fully utilize the advantages of 3D spatial information. Detected damage structures are registered to the hosting struts and supporting structures based on the network representation. Various damage features are quantified, including damage structural morphology and spatial distribution, hosting struts preference and weakness location, supporting struts properties, and etc. Holistic review of these damage features enables

the tracing of structural-damage relationship and provide the possibility to unravel the design code for cellular materials. We demonstrate the efficiency of our proposed approach with the sea urchin spine as the model system for representative damage modes including catastrophic failure under shear force, and graceful failure under compression and shear-free bending. By removing cumbersome manual labeling and avoiding associated intra- and inter-observer variations, our method enables large-scale quantitative registration of damage structures and their interactions with the hosting cellular structure. The comprehensive damage data can be directly used for precise damage modeling and simulation, paving the road towards quantitative material design for damage tolerance.

4.2 Methods

The proposed pipeline consists of four modules: (i) In-situ synchrotron X-ray tomography, which enables collection of 3D microstructure in a macroscopic volume; (ii) Automated 3D damage features detection to recognize damage behaviors in different scales; (iii) Quantitative 3D structural analysis of the cellular microstructure, by which key morphological descriptors of the structure are extracted and quantified; (iv) Automated multi-scale damage structure analysis, which provides quantitative understanding of damage behaviors. Fig. 4.2 depicts a flowchart for the four modules and their connections.

4.2.1 In-situ synchrotron Tomography data acquisition and reconstruction

Dried cylindrical-shaped spine specimens from the sea urchin Heterocentrotus mamillatus (diameter, 10-15 mm, as shown in Fig. 4.1(a)) were used for this work. A coordinate system

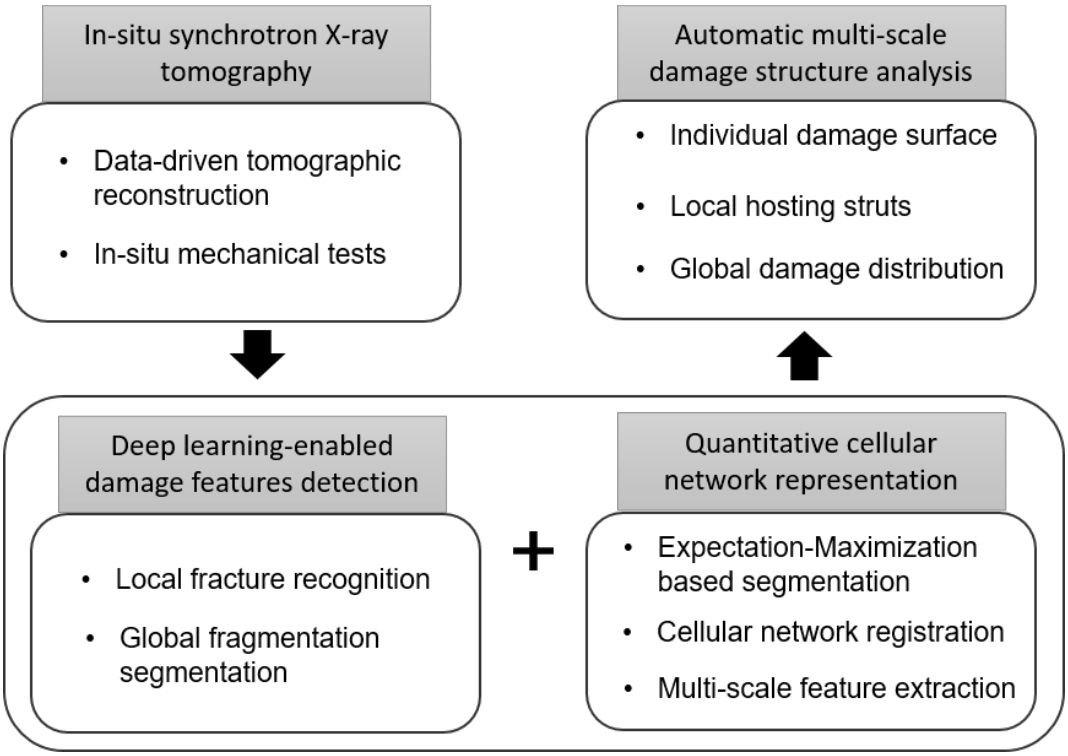

Figure 4.2: Workflow of the quantitative damage characterization pipeline developed in this work.

with three orientations, L (longitudinal direction of the spine), C (circumferential direction of the circular cross section), and R (radial direction of the circular cross section) was used consistently throughout this work. Samples with this configuration were imaged via the synchrotron-based μ-CT measurements conducted at the beamline 2-BM at the Advanced Photon Source, Argonne National Laboratory. A customized in-situ mechanical loading device was used for both synchrotron-based compression and indentation tests, through which the samples can be mechanically tested while allowing for X-ray imaging through an X-ray transparent window. For the in-situ compression tests, the samples were compressed by a steel platen through a stepwise fashion (typical step size, ca. 0.1 mm). Once the displacement is stopped, the sample stage together with the in-situ device was rotated for a full tomography scan. The beamline was equipped with a single-crystal LuAg:Ce scintillator

for converting the X-ray into visible light, which was further magnified with a 2x or 5x long-working distance objective lens. For a typical scan, 1500 projection images were acquired during a rotation with the exposure time of 0.1 s (corresponding to the total scan time for a single tomography scan of 2.5 mins). The projection images were collected by using a PCO-Edge high-speed CMOS detector (2448 $\times$ 1024 pixels), which resulted in typical voxel size of 1.725 or 0.69 μm depending on the objective lens used. This resolution ensures the profiling of local branch morphology, with at least 10 voxels sampled across the branch cross sections. For the in-situ indentation tests, a ceramic tip was used to induce localized deformation.

The tomographic reconstructions of the collected projection images were achieved through two methods: a standard Fourier grid reconstruction algorithm implemented in the open source software Tomopy [98] for full-view measurements and a custom-developed knowledge-Incorporated hierarchical synthesis convolutional neural network (HSCNN) implemented for sparse-view measurements to speed up the acquisition. For the reconstructions implemented in Tomopy, a number of imaging treatments were used to suppress noise and remove reconstruction artifacts. Firstly, pixels with abnormal counts resulted from defective detector pixels were removed from the projection images and replaced by the average of surrounding pixels. Secondly, the projection images were normalized with the white and dark backgrounds. Thirdly, streak artifacts caused by X-ray scattering were suppressed by applying a Fourier Wavelet-based filter[37], Titarenko's filter[38] and subsequently a smoothening filter to the projection sinograms. Lastly, for the diffraction induced fringes at the edge and the presence of high-density convoluted interfaces in the structure[39,40], a phase retrieval step was conducted to restore the diffraction fringes to sharpen the boundaries of the objects. This step is implemented through the phase-attenuator duality model[41-43], where the attenuation coefficient (absorption) and the extinction coefficient (phase diffraction) are jointly considered for imaging reconstruction. Desired sharpness of edges was obtained by

manually tuning the relative strength between the absorption and the phase diffraction.

In the custom-developed HSCNN method, sparse-view (150 projection images) measurements are uniformly extracted from full-view (1500 projection images) measurements for the undamaged original stage, which provides 10 times reduction of the scan (from 2.5 mins to 15 secs). Image slices are then reconstructed with both sparse-view and full-view measurements with Tomopy toolbox as the input and ground truth to train the HSCNN model. Detailed implementation method related to HSCNN model is discussed in Chapter 2. After training the HSCNN model for undamaged stage, We could further implement it to damage stages with faster experiment speeds which could provide more continuous damage stages.

4.2.2 Deep learning enabled autonomous damage features detection

The damaged construction units (struts) embedded in the complex cellular network are identified via a deep learning-enabled process. Common features of damaged struts are extracted in a semin-3D manner by learning in three orthogonal views and neighboring adjacent slices of each direction, which enables accurate damage regions detection in new cases. The choice of deep learning framework could be adjusted depending on the integrality degree and distribution scope of damaged struts.

Classification of local scale damage features

The slightly damaged strut usually behaves like a separated intact strut with a high contrast micro-notch (fracture). Fractures embedded in original struts are distributed locally, and thus identified by DL-based local feature recognition algorithm, as shown in Fig. 4.3. Fracture locations and rough shapes are firstly proposed by correlating with a manual-established

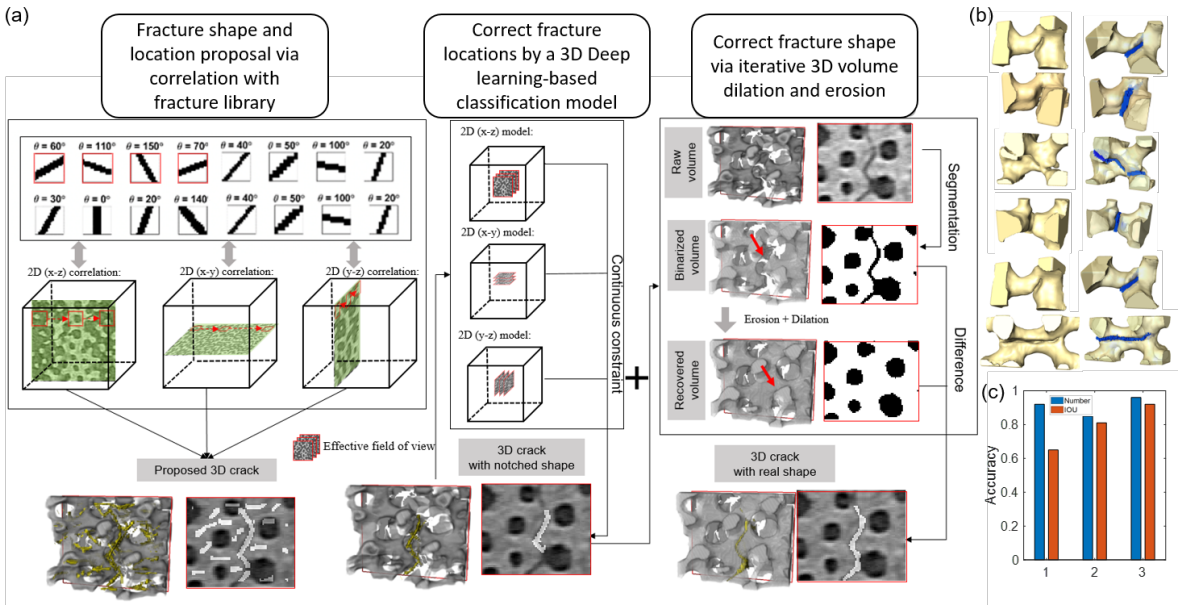

Figure 4.3: Deep learning-based fracture recognition. (a) Method flow of fracture detection. (b) Selected 3D view of individual struts and corresponding detected fracture, illustrating the correct classification results using this three-step strategy algorithm. (c) Performance of fracture detection accuracy in terms of number and area (IOU) for each step, which showing the high fracture number accuracy at the last step and increasing fracture area detection accuracy.

multi-scale fracture library. Fracture patterns are defined as multiple narrow gap patterns and formed as a feature map library. Such local fracture feature libraries considering all possible orientations, widths, and lengths in the small patch of size, based on the observation of fracture patterns from the databases and resolution limits. Tomographic reconstructed slices are correlated with the defined crack library in the x-y, y-z, and x-z planes as the first step in Fig. 4.3(a). An initial crack filtering is then implemented by thresholding the maximum correlation value for each pixel. The highly correlated locations indicate a high probability of finding a crack, and the highly correlated filter at this location reveals the shape of the potential crack. The proposed crack candidates are then further classified in the 3D DL-based algorithm to enhance the accuracy of detection based on nonstandard features beyond the feature library and correct the influence of complex cellular structures.

We calibrate the initial fracture detection with manually labeled crack data, which is used to train a convolutional neural network (CNN) classifier. Adjacent slices in addition to 2D image slices are involved to extract 3D multi-scale features. Finally, 3D image dilation and erosion are implemented to the summation of identified fracture with damage struts as faked intact struts. Real fracture shape is refined by subtracting damage strut from faked intact struts.

Segmentation of global scale damage features

With the accumulation of multiple fractures, struts are further separated into multiple pieces, leading to fragmentation. Fragmented struts are distributed dispersed across space and are more interconnected compared to fractures. A semi-3D segmentation framework is established to label the fragmentation regions by combining detection results from three orthogonal views to fully utilize feature in different orientations. To be specific, fragmented struts are first manually labelled in three different orientations, each orientation with 10 image slices. These image slices in combination with their adjacent slices and their corresponding manual segmentation are used as the input and ground truth to train one convolutional neural network (CNN). The image slices in three different orientations are identified with the trained network separately. Final fragmentation results are obtained by combining results from three different orientations. In each orientation, we further extended the 2D segmentation, which is usually done by to extracting features from a single 2D slice, to semi-3D by taking advantage of the spatial correlation between adjacent slices. The semi-3D training significantly reduces computational costs and memory requirement compared to an end-to-end training of the 3D architecture.

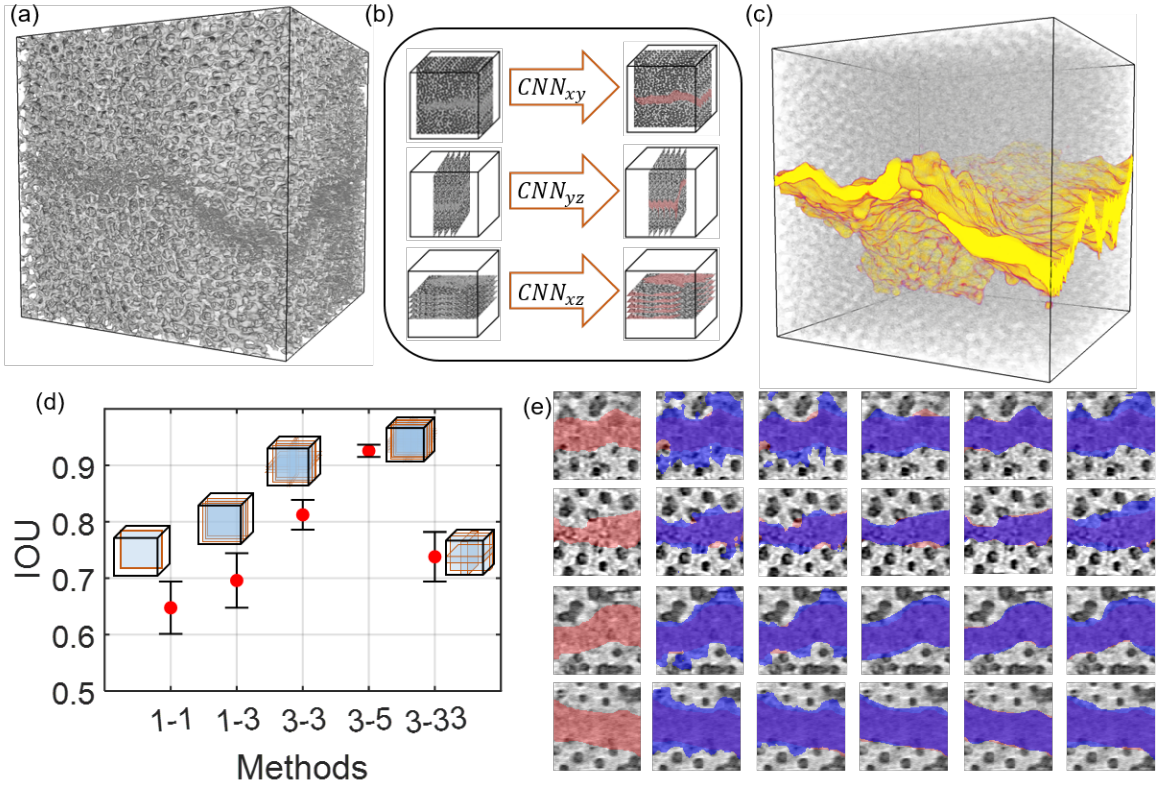

Figure 4.4: Global fragmentation detection. (a) 3D representative damaged volume. (b) Fragmentation segmentation framework, which contains three different CNNs in three different orientations, including the x-y, y-z and x-z planes. (c) Final segmented fragmentation region, colored in yellow. (d) Fragmentation detection accuracy with different recognition strategies, including 1-1 (1 orientation and 1 slice), 1-3 (1 orientation and 3 slices), 3-3 (3 orientation and 3 slices), 3-5 (3 orientation and 5 slices), 3-33 (3 orientation and 33 slices). These different strategies are implemented to study the importance of involving different orientation and different number of adjacent slices. The strategy of 3-5 shows the best results, which is the algorithm we used for segmentation in the following analysis. (e) Selected 2D slices to show the performance of each strategy.

4.2.3 Quantitative 3D structural analysis of the cellular microstructure

Besides autonomous detection of damage features, a quantitative description and analysis in 3D are required to fully understand the mechanical properties of the complex cellular structures. However, the details of the network organization and statistical features of these

structures in both local and global scales still remain elusive. In this section, we present a comprehensive computational data analysis pipeline for processing, extracting, representing, and analyzing the hierarchical structural parameters of the 3D cellular microstructures of echinoderms' skeletons by using sea urchin spines as a model system.

Automatic image segmentation

We first segment the tomographic imaging of cellular microstructure of sea urchin spines into binary data. We utilized the Expectation-Maximization (EM) algorithm to group pixels into foreground and background by modeling the distribution of pixel features with a mixture of Gaussian functions. Segmented volumes are shown in Fig. 4.5A.

Network construction and Network construction

The segmented volumetric data was used as the input for the cellular network analysis followed by the procedures below.

Skeletonization: A custom-written 3D thinning algorithm based on an iterative erosion method was developed to extract the 3D skeleton of the cellular structure from the binarized data, which represented individual branch as a line with one voxel thickness [123] (Fig. 4.5A-C). The skeleton of the cellular structure consists of a network of branches interconnected with nodes. The node of the skeleton is defined as the voxel with more than two neighbor voxels. The position of the node is also used to register individual branch by specifying the starting and ending nodes. The network after the direct skeletonization treatment suffers from several inherent artifacts, including extrusions from dangling branches (Fig. 4.5E) and node clusters characterized by unrealistic short branches (Fig. 4.5F).

Adaptive trimming: To refine the skeletonized network, we applied an adaptive trimming

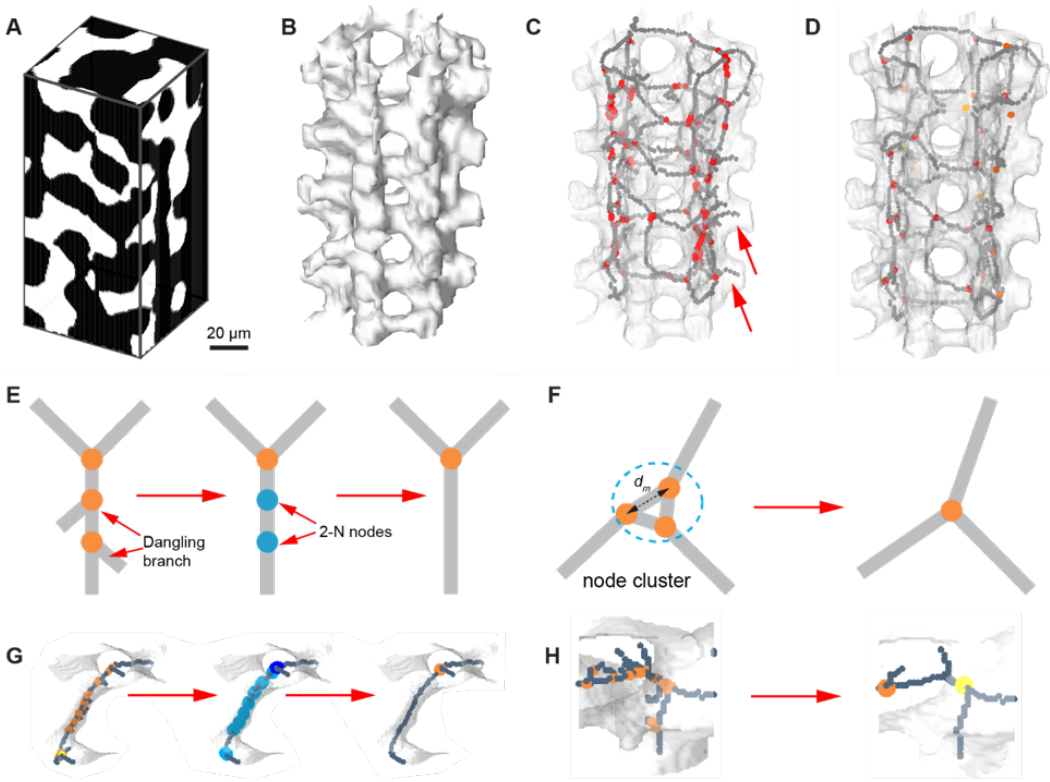

Figure 4.5: Network construction. (A) A representative volume based on the segmented binary data. (B) 3D rendering of the cellular structure, and corresponding (C) cellular network consisted of branches (gray) and nodes (colored dots) after initial skeletonization step and (D) after adaptive trimming and node merging. (E) Schematic illustration and (G) a corresponding representative example of the adaptive trimming process, which removes extruded dangling branches and associated nodes. (F) Schematic illustration and (H) a corresponding representative example of the node merging process, through which node clusters with distances between adjacent nodes smaller than a critical distance, d_m will be merged to a single node.

process to remove extruded branches, which were branches not connected to the network at one end (Fig. 4.5E). Extruded branches are often due to the local surface extrusions of the cellular structure. In addition, branches that are cut off by the volume boundaries also exhibit as extruded branches (red arrows, Fig. 4.5C). Extruded branches are identified by inspecting the connectivity and lengths of branches within the analyzed network. As the side effect of this removal step, nodes connected by two branches, which are referred as 2-N nodes, emerge. We identified each pair of branches connected by these 2-N nodes and connected

these branch pairs by replacing these 2-N nodes with branch points. The connectivity of the network is updated after each trimming step after all the extruded branches are removed, as shown in an example in Fig. 4.5G.

Node merging: After removing the extruded branches with the adaptive trimming, further refinement was conducted on nodes. The node cluster that is composed of nodes connected with very short branches is considered as artifacts after skeletonization (Fig. 4.5F). We first dealt with one special case of node cluster, i.e., adjacent nodes that are directly connected without branch points between the nodes. Connected nodes are results from the skeletonization of the non-smooth discrete volume, where extrusion are recognized as branches with unnecessary nodes. We replaced connected nodes with one single node, the coordinate of which is in the center coordinate of the node cluster. The connectivity of the network is updated after this merging procedure. For general case of node clusters, we removed short branches and merged the node cluster into one node in the center of the cluster. In our analysis, we set the threshold of merging distance (dm = 10 voxels, corresponding to 6.5 μm) to be roughly the mean branch radius (6.2 μm). As shown by a typical example in Fig. 4.5H, many node clusters are present in the original skeletonized network, and this merging process is critical to clean the unnecessary nodes and short branches.

The aforementioned steps establish the cellular network of the original tomography data of sea urchin spine's porous structure. The network information, including nodes, branches, and their associated surface profiles, is registered in terms of a featured graph $G = N, B, P$, where N and B represent for nodes and branches, respectively. The associated surface profiles, P, for individual branches are registered by using the binarized volumetric data. This allows for further structural quantification, such as branch thickness, surface curvature, and node diameter. The size of this combined network representation is 0.1% of the original tomography data, yet it carries the complete geometric information of the original structure.

Feature extraction and analysis

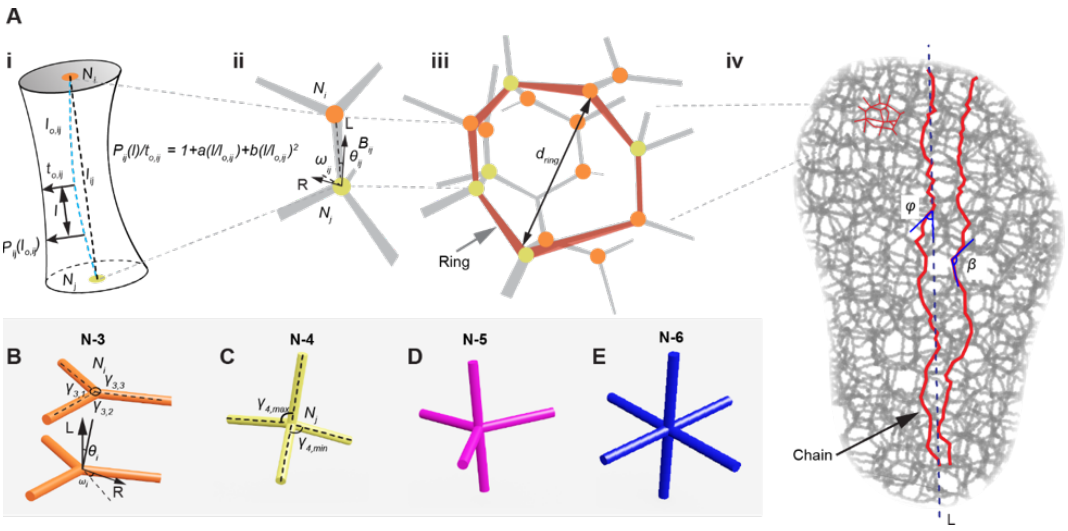

Figure 4.6: A multi-scale representation scheme for the cellular network of sea urchin porous structures. (A) On the individual branch level (panel i and ii), each branch is denoted as B_{ij} bounded by two nodes N_ind N_j which is characterized by its original branch length ($l_{o,ij}$), Euclidean distance (l_{ij}),branch orientation $\theta_{o,ij}$ and $\omega_{o,ij}$,branch thickness ($t_{o,ij}$, the radius of the thinnest part of a branch) and branch morphology. $\theta_{o,ij}$ the misorientation angle of the branch from longitudinal direction (L) and $\omega_{o,ij}$ denotes the angle between the branch projection and radial direction (R) in R-C plane. The branch morphology along a branch ($P_{ij}(l)$)) is normalized and fitted into a quadratic function. On the local cellular level (panel iii), the node types (represented by colored dots) and ring structures formed by connected branches (highlighted by a red circle) are registered. The diameter of the rings is denoted as d_{ring} global network level (panel iv), the long-range alignment of branches, denoted as "branch chain", can be identified. Two angles are defined: ψ. misorientation angle of a branch in the chain from longitudinal direction (L), β, inter-branch angle between two adjacent branches in the chain. (B-E) Schematic diagrams of node type N-3, -4, -5, and -6. $\gamma_{3,1}$, $\gamma_{3,2}$, $\gamma_{3,3}$ represent the three inter-branch angles in N-3 node ($\gamma_{3,1} < \gamma_{3,2} < \gamma_{3,3}$), and mean angle $\gamma_3 = (\gamma_{3,1} + \gamma_{3,2} + \gamma_{3,3})/3$. θ and ω represents the node orientation. The misorientation angle (θ) for N-3 node is the angle between the longitudinal direction (L) and the normal direction of the base plane of N-3 nodes. By projecting such normal direction to R-C plane, the angle ω denotes the angle between the projection and the radial direction (R).$\gamma_{4,min}, \gamma_{4,max}$ represent the minimum and maximum inter-branch angle for a N-4 node N_j.

In this step, we developed an automatic computer vision-based pipeline to extract, classify, and analyze the structural descriptors of the registered cellular network and surface morphol-

ogy at three length scales, namely, the individual node and branch level, the local cellular level, and the global network level (Fig. 4.6).

Individual node and branch level: The network connectivity registration identifies individual branch, B_{ij}, which is bounded with two end nodes, N_i and N_j, as shown in Fig. 4.6A-i. The branch length is calculated with two metrics, the Euclidean distance, l_{ij}, defined as the straight distance between the starting and ending nodes, and the physical branch length, $l_{o,ij}$, obtained by accumulating the distances in all neighboring voxels on the branch. The physical length $l_{o,ij}$ records the curviness of the branch and therefore is usually greater than the Euclidean distance l_{ij}. We define the branch length ratio as $s_{ij} = l_{o,ij}/l_{ij}$, which is greater than 1 for curved branches and equals to 1 for straight ones. The branch orientation is characterized by two angles, the misorientation angle, θ, and the in-plane rotation angle, . θ is defined as the angle between a branch vector and a reference global direction (e.g., the longitudinal direction (L) of the sea urchin spine). For calculation of the in-plane rotation angle , the branch vector is first projected to the plane perpendicular to the defined global direction (e.g., the R-C plane for the case of direction L). is then defined as the angle between the projection direction and another selected in-plane reference direction (e.g., the radial direction R). The in-plane misorientation angle ranges from 0° to 360°. The branch profile, P_{ij} (l), is used to describe the cross-sectional size and morphology along the length of each branch (Fig. 4.6A-i). This is achieved by registering the intersecting line profiles between the cross-sectional planes (perpendicular to B_{ij} at the sampling point) and branch surface at a given location of l. This allows for the determining the branch profile, P_{ij}, by using the radius of an equivalent circle with the same area of the intersecting profile. The thickness in the middle of a branch is denoted as branch thickness, $t_{o,ij}$. The local branch

thickness profile P_{ij} is fitted with a second-order polynomial

$$P_{ij}(l)/t_{o,ij} = 1 + a(l/l_{o,ij}) + b(l/l_{o,ij})^2 \tag{4.1}$$

where a and b are fitting parameters.

Following the previous work on the inter-trabecular angle (ITA) method developed by Reznikov et al. for the analysis of trabecular bone microstructure[4,53], we quantified the node connectivity and characteristics of the cellular structure of sea urchin spines (Fig. 4.6A-ii). First, the node type is categorized by the number of branches connected to a given node as N-3 (with three connecting branches), N-4 (with four connecting branches), ..., and N-n (with n connecting branches) (Fig. 4.6B-E). The inter-branch angle for different node types is defined following the similar approach described in [4,53]. For example, for N-3 nodes, the three inter-branch angles are denoted as $\gamma_{3,k}$, where k (1, 2, and 3) indexes the three angles in a ascending order (Fig. 4.6B). The average inter-branch angle for individual node is denoted as γ_3. Similarly, the inter-branch angles for N-4 nodes are represented by $\gamma_{4,min}, \gamma_4, \gamma_{4,max}$ representing the minimum, average and maximum values (Fig. 4.6C).

To analyze the orientation of N-3 nodes, we defined a central axis as the orientation that shared the same angle with each individual branch of a N-3 node (Fig. 4.6B). The misorientation angle θ and the in-plane rotation angle are defined in a similar way for the branch orientation. The direction of the central axis is selected so that the angle between the central axis and each branch is less than 90 degrees. Due to this convention, the misorientation angle θ ranges from 0° to 180°, which is different from the range of branch orientations. Following the previous work on trabecular bones [124], we defined the cosine of the angle between the central axis and each branch as the planarity index, which varies between 0 and 1. The plane formed by N-3 nodes is flatter when planarity index is closer to 0.

Local cellular scale: In this scale, we investigated the local interconnection characteristics of adjacent branches. An algorithm was developed to quantify the number of branches required to form a complete ring structure (Fig. 4.6A-iii). The analysis process is as following: starting from a given node, a "tree-shape" structure is constructed by identifying the neighboring nodes that are connected to the starting node. As this process continues to expand the "tree" structure, a ring is identified when the original node is included in the new layer of connections. This indicates that the node is connected back to itself in a non-repeated manner. The number of branches included in a complete ring is then used to define the ring type. For instance, a 5-B ring refers to a ring composed of 5 branches. We calculated the area enclosed by the ring and fitted it into a circle. The diameter of the fitted circle is defined as the ring size (d_{ring}). All branch points that form a ring are fitted into a plane, the normal direction of which is defined as the ring direction. The ring orientation is characterized by following the same definition of branch orientation and N-3 node orientation.

Global scale: The alignment of connecting branches over long distance is investigated by defining a branch alignment factor as $CAF_{ij}^{k} = max\ _{(}k = i, i+1\ldots)(c_k\ c_{(}k+1))_{(}k, k+1)$, where c_k is the unit vector of normal direction of the kth branch in a "chain" structure starting from the branch of interest. By including the inter-branch angle $_{k,k+1}$ between two neighboring branches in the chain structure, CAF measures the degree of alignment for the most aligned k-node chain structure (Fig. 4.6A-iv). An iterative algorithm is implemented to detect aligned chain structure with minimized CAF. The statistical analysis of inter-branch angle β, branch length and thickness for branches in the detected chains, and offset angle (the angle away from a defined global direction) can be performed to evaluate the structural characteristics of these chains. We further quantitatively describe the structural orderings at global scale by conducting the long-range 3D fast Fourier transform (3D-FFT) analysis of structural descriptors extracted from the full-volume registered network of the

cellular structure. In particular, we applied Fourier analysis on registered node positions over large volumes (>0.1 mm^3) to investigate its long-range periodicity. Note that directly implementing a Fourier analysis on the original 3D tomography data with such large volume is computationally expensive, and not necessarily informative due to the mixing of structure information on all different scales. The 3D-FFT analysis based on the node distribution resolves these challenges, and provide a clear representation of the global orderliness or randomness of the cellular network.

Implementation and accessibility

The customized cellular network analysis algorithm has been implemented in MATLAB. It is available for download at *https://github.com/Ziling-Wu/Quantitative-3D-structural-analysis-of-the-cellular-microstructures*.

4.2.4 Multi-scale damage structure analysis

With the detected damage features and quantitative description framework of the cellular structure, we perform a multi-scale damage structure analysis to quantitatively characterize the damage process. This provides important insights to study local damage preference and overall damage evolution process, which are mostly studied qualitatively in previous research. Damaged struts are firstly identified by overlapping detected fracture/fragmentation with the original undamaged volume. Here we identify the corresponding original undamaged volume by using digital volume correlation (DVC) with the damaged volume. This volume is then represented as a cellular network consisting of individual nodes and labelled connecting struts as discussed in section 4.2.3. All struts are characterized by branch length, branch thickness, and branch orientation. Damage surfaces are then located and registered to each hosting

individual strut through the nearest neighbor criterion. These hosting struts are classified as broken struts and the rest struts without registered damage surfaces are considered as intact struts. Subsequently, registered damage struts surface are analyzed at three length scales, including individual damage surface level, local hosting struts level, and global damage distribution level.

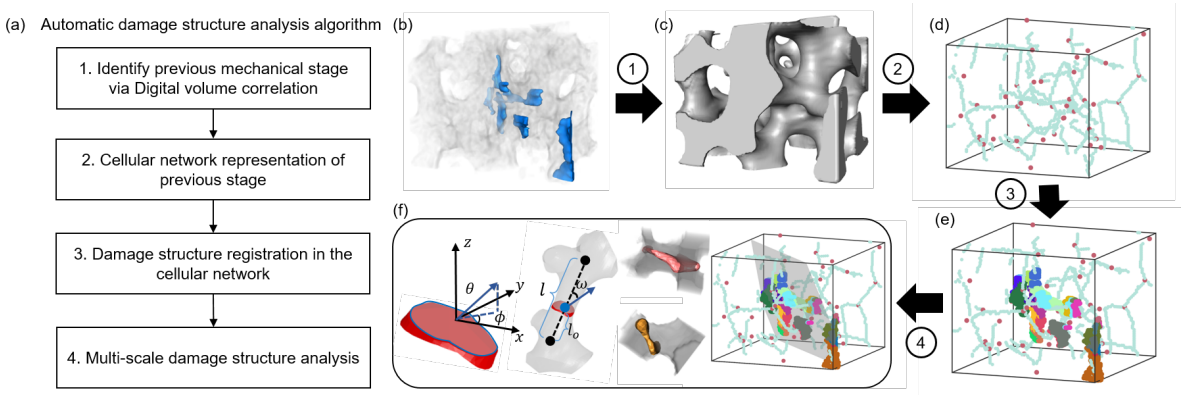

Figure 4.7: Automatic multi-scale damage structure analysis. (a) Steps of automatic damage structure analysis algorithm. (b) Damage detection results with deep learning-based recognition. (c) Identified previous mechanical stage (undamaged or previous stage) via digital volume correlation. (d) Cellular network representation of undamaged volume. (e) Damage structure registration in the cellular network. (f) Multi-scale damage structure analysis.

Individual damage surface level: Individual properties of registered damaged surface are quantified through principal component analysis in 3D, which results in three principal directions with different variances. The principal direction with the minimum variance is treated as the normal direction of the registered damage surface, which is also named as damage vector v_d. The orientation of registered damage vector v_d is characterized by two angles, the misorientation angle, θ, and the in-plane rotation angle, ϕ. θ is defined as the angle between a damage vector and a reference global direction (e.g., force direction during the mechanical test), which ranges from 0° to 90°. For calculation of the in-plane rotation angle ϕ, the damage vector is first projected to the plane perpendicular to the defined global direction and then defined as the angle between the projection direction and another selected

in-plane reference direction. The in-plane misorientation angle ϕ ranges from 0° to 180°.

Local hosting struts level: Registered damaged surface is further correlated to the hosting struts in the local scale. We first characterize the intersection angle between the struts and damage vector v_d as inter-branch-damage angle ω. There are two ways to fracture the struts as through-damage and across-damage. Through-damage goes through the nodes area and continuously destroy the other struts; Across-damage only fracture single struts without connecting to a next registered damage. Branch ratio ω_o is used as the criterion to differ these two different damage types, which is defined as the ratio of branch thickness and half of the branch length for each specific strut. If the inter-branch-damage angle ω is bigger than ω_o, the damage is denoted as through-damage, otherwise, it is described as across-damage. Exact damage positions are further identified as the point in the branch line which has the smallest distance to the damage surface. In this case, damage location is defined as the minimum distance l_d of the damage point to the connected nodes over the branch length l.

Global damage distribution level: Damage surfaces are fitted into one plane with the principal components analysis algorithm. The planarity is defined as the distance of each point on the damage surface to the fitted plane, which shows the variation of the damage propagation. Damage surfaces are further labelled as each isolated parts considering their connectivity. The number of registered damage surface on each isolated damage surface is counted to study the connectivity of damage surfaces.

4.3 Results and Discussion

4.3.1 In-situ synchrotron Tomography reconstruction

We performed sparse-view tomography of 150 views and 75 views for undamaged sea urchin spine volume with our developed HSCNN algorithms. 2D image slices reconstructed based different acquisition conditions, including full-view, 150-views, and 75-views are compared in chapter 2.3.3. *In situ* sparse-view experiments under mechanical tests have not performed yet as the result of the Covid shut-down policy. HDrec algorithm discussed in chapter 3 also shows the potential to speed up the acquisitions to provide more continuous damage stages. We would like to perform *in situ* hybrid-dose acquisition experiment for sea urchin spine structure under mechanical tests in the future. We intend to acquire several normal-dose measurements (P_n) and full-view low-dose measurements (P_l) before the mechanical test to learn the denoise model firstly. Then continuous full-view low-dose projections (P_l) are acquired with the advancement of mechanical tests. Each full-view scan will take shorter time depending on how low dosage each projection is. For example, ten times dosage reduction on each projection could lead to 30 seconds per scan. Then the learned denoise model is applied to measured continuous low-dose projections and obtain high-quality measurements. In this way, more continuous damage stages are acquired to study the dynamic evolution process. For the following analysis, we still utilize the full-view reconstructed volumes to demonstrate our analysis methods.

4.3.2 Damage detection accuracy

Fracture detection accuracy

We used a data set of 2 volumes (which contain $\sim$ 200 fractures), cropped from two different mechanical test experiments, to train and validate the fracture labelling algorithm. We obtained a number classification accuracy (the percentage of correctly classified fracture number according to a human observer) of 95% and an area classification accuracy (IOU: interaction of classified fracture area and a human observer result over union of these two results) of 92%. It is worth to be noted here that it is difficult to determine the ground truth via human labelling since the complex and noisy background. Our final detected results are visually similar to the manual labelled results without obvious errors. The accuracy of each step is also shown in Fig. 4.3(c). A few examples of fractured struts and their corresponding recognized fractures also show the correct classification results using this three-step strategy algorithm.

Fragmentation detection accuracy

Fragmented struts are first manually labelled in three different orientations, each orientation with 10 different image slices. These image slices combined with their adjacent slices and their corresponding manual segmentation are used as the input and ground truth to train (24 slices) and validate (6 slices) the fragmentation segmentation network. Five different segmentation strategies are studied , including 1-1 (x-y orientation and 1 slice), 1-3 (x-y orientation and 3 slices), 3-3 (3 orientation and 3 slices), 3-5 (3 orientation and 5 slices), 3-33 (3 orientation and 33 slices). These different strategies are implemented to study the importance of involving different orientation and different number of adjacent slices. The strategy of 3-5 shows the best results with the IOU of $92.56\% \pm 1.10\%$, which is the algorithm

we used for segmentation in the following analysis, as shown in Fig. 4.4(d). Several selected 2D slices are shown in Fig. 4.4(e) to illustrate the performance of each strategy.

4.3.3 Network representation and multi-scale statistical analysis

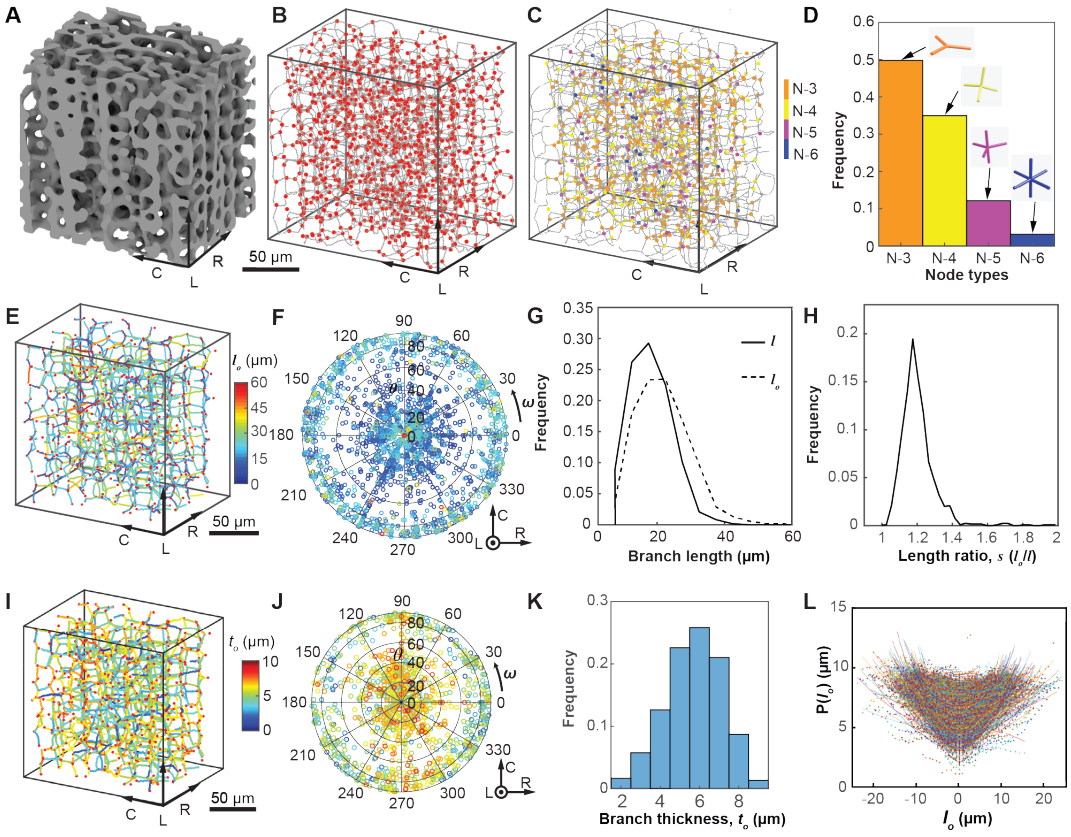

Figure 4.8: Selected quantitative analysis of the cellular structure in H. mamillatus spines. (A) 3D rendering and (B) corresponding skeletonized network of a volume close to the center region of a H. mamillatus spine. (C) Skeletonized network with node types indicated with colored dots. (D) Distribution of node types in this volume. (E) Network representation of the selected region with branch length highlighted in different colors and (I) Correlation of branch orientation and length in the same volume. (D)&(I) are based on the same color scale. (G) Distribution of branch length $l_{o,ij}$ and Euclidean distance l_{ij}. (H) Distribution of the length ratio s_{ij}. (I) Skeletonized network with branches colored according to their thicknesses ($t_{o,ij}$). (J) Correlation between branch orientation and thickness in this volume. (K) Statistical distribution of branch thicknesses $t_{o,ij}$ in this volume. (L) Measurements of branch profiles and the fitting results for individual branches in this volume.

In this work, we chose the spines from sea urchin H. mamillatus as our model system. The H. mamillatus spines exhibit a gradient porous internal structure with porosity ranging from 80 vol% in the center to 60 vol% in the edge region, which was consistent with previous measurements [125]. In the current study, we used a relatively small region (200 μm (R)×250 μm (C)×250 μm (L)) of the sea urchin spine (H. mamillatus) to demonstrate the capability of this cellular network analysis method. The representative volumes used in this work were extracted close to the center region of a spine. We show several selected statistical results of this represented volume in this section.

The representative volume (200 μm (R)×250 μm (C)×250 μm (L)) after segmentation is shown as a 3D volume rendering in Fig. 4.8A. After the initial skeletonization, this volume contains 6342 nodes and 4574 branches. The trimming process reduces the numbers to 5126 nodes and 3584 branches, and the final merging treatment further refines to 1249 nodes and 2233 branches. The density of nodes and branches are $124900/mm^3$ and 223300 $/mm^3$, respectively. Fig. 4.8B shows the final registered network including the node coordinates N_i in red dots and connecting branches B_{ij} in dotted grey lines.

Node characteristics: Due to the incomplete cutting of branches at volume boundaries, nodes within 10 μm and branches within 20 μm from boundary are not considered in our further analysis. In this volume, 289 nodes and 1030 branches are deleted due to this boundary effect. The node types of the valid nodes within this volume is illustrated in Fig. 4.8C as differently colored dots, which exhibits a uniform distribution. As shown in Fig. 4.8D, node type N-3 (nodes connected with three branches) and N-4 (nodes connected with four branches) are dominating node types within this volume (50% and 35%, respectively). Node type N-5 and N-6 comprise 12% and 3%, respectively, where no N-7 nodes and nodes of higher-connectivity are observed. The relative frequencies of N-3: N-4: N-5: N-6 nodes are around 17:12:4:1.

Branch characteristics: The measurement of the branch length requires a consistent determination of the two ends of a branch. With the skeletonized network representation, we are able to measurement the lengths and morphology of branches consistently. First, both physical branch length $l_{o,ij}$ and the Euclidean distance l_{ij} are calculated for each branch from the network registration, and the distribution is shown in Fig. 4.8G. The mean physical branch length is 21.7±7.9 μm and the mean Euclidean distance is 18.0±6.2 μm (N=1203). As shown in Fig. 4.8H, the length ratio s_ij is 1.2 ± 0.1, indicating that most of branches are slightly curved. The branch length can be also presented by the 3D branch map colored in terms of their physical length shown in the original cellular network (Fig. 4.8E). The correlation between branch orientation and branch length can be further visualized by using the polar scatter plots (Fig. 4.8F). The long branches (cyan and yellow data points) typically have =90°, which indicates that they are orientated in the R-C plane. Moreover, the shorter branches corresponding to the dark blue data points exhibit a clear orientation preference by aligning along the L direction with misorientation angles centered around 20°. In addition, the uniform distribution of in-plane rotation angles shows no orientation preference in the R-C plane.

The calculated branch thickness t_o is shown in a colored 3D diagram mapped on the original cellular network (Fig. 4.8I). The mean branch thickness is 6.2±1.5 μm (N = 1203), and most of the branch thicknesses range from 4 to 8 μm (Fig. 4.8K). In addition, as shown in the polar plot of the branch thickness as a function of their orientation distributions (Fig. 4.8J), the thicker branches (red and yellow data points) concentrate in the center of the plot, indicating that the branches aligned in the longitudinal direction tend to have larger thicknesses, whereas the branches with values close to 90° typically have thickness smaller than 5 μm (blue data points, Fig. 4.8J). This indicates that the thinner branches are mostly oriented in the R-C plane. In addition to the single branch thickness value at the middle

point of a branch, the entire transverse profile of each branch within this volume is extracted as P_ij, which is then fitted with a 2nd order polynomial according to Eq. 4.1 (Fig. 4.8L). The average normalized branch morphology, we normalize each individual branch profile with its own length l_o and thickness t_o, and the fitting result is $P(l)/t_o = 1 - 0.026(l/l_o) + 1.23(l/l_o)^2$ ($R^2 = 0.899$). This finding indicates that the branches in the sea urchin spine structure are highly curved, in stark contrast to the morphologies of branches in synthetic foams, where the well-known plateau branches are observed [126, 127].

More statistical analysis results in local cellular level and global network level are included in the references.

4.3.4 Results of multi-scale damage structure analysis

In this section, we show the multi-scale fracture and fragmentation analysis results. Three different cases of fracture regions detection embedded in their corresponding representative volumes are depicted in Fig. 4.9(a), which are extracted from three different mechanical tests. Fig. 4.9(a-i) shows the volume ($186\mu m \times 233\mu m \times 186\mu m$) under the compression mode, Fig. 4.9(a-ii) shows the volume ($260\mu m \times 326\mu m \times 260\mu m$) under the shear mode, and Fig. 4.9(a-ii) shows the volume ($208\mu m \times 260\mu m \times 208\mu m$) under the bending mode. These volumes are of similar number of struts ($\sim$ 1400 struts). Fractures are registered to each individual struts and colored differently according to their orientation θ in Fig. 4.9(b). We can see that fractures formed under the compression mode (Fig. 4.9(b-i)) are more concentrating around 0 degree and tend to be perpendicular to the compression direction. Such distribution is dramatically different compared to the distribution of fractures formed under the shear mode (Fig. 4.9(b-ii)), which are more concentrating around 90 degree and tend to be parallel to the compression direction. The distribution of fracture under the bending mode

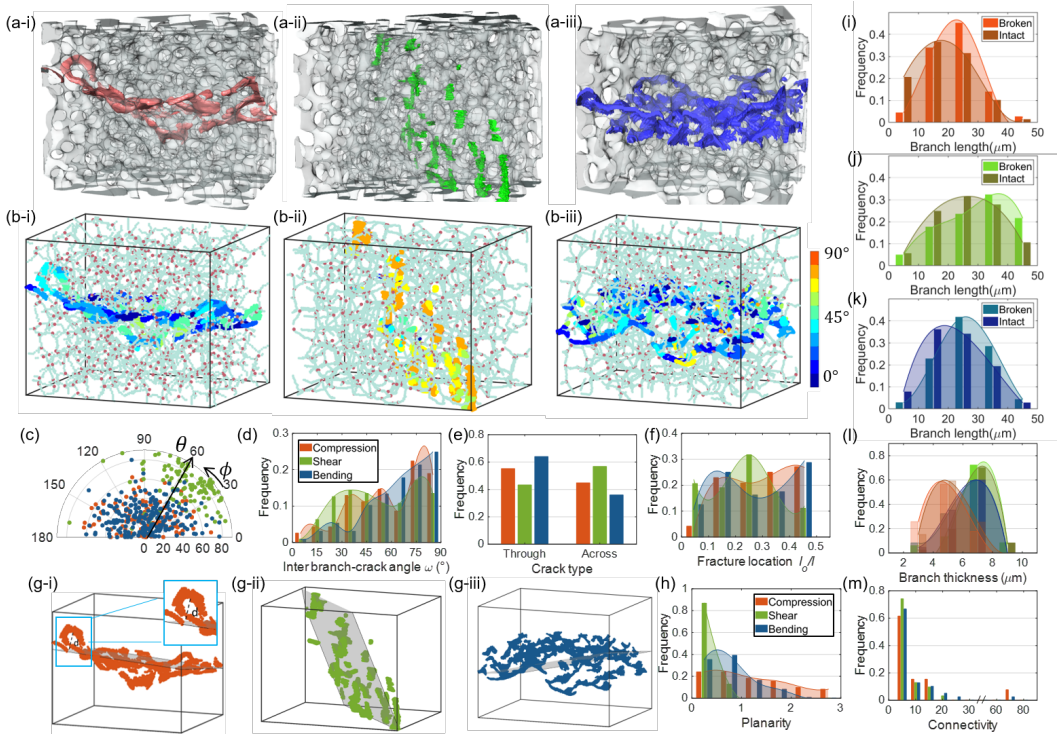

Figure 4.9: Fracture analysis results. (a) Fracture regions detection embedded in their corresponding representative volumes under (a-i) compression, (a-ii) shear and (a-iii) bending modes. (b) Fractures registered to each individual struts with different colors according to their orientation θ for these three different modes. (c) In-plane rotation angle ϕ distribution. (e) Inter branch-crack angle ω distribution, and (f) comparison of two different crack types for these three different modes. Branch length distribution in terms of broken and intact struts for (i) compression, (j) shear, and (k) bending modes. Branch thickness distribution in terms of broken and intact struts for these three modes. (g) Fitted plane in gray color for (g-i) compression, (g-ii) shear and (g-iii) bending modes. Overall (h) planarity and (m)connectivity distribution.

(Fig. 4.9(b-iii)) is more dispersed compared to the rest two. In terms of the distribution of in-plane rotation angle ϕ (Fig. 4.9(c)), fractures formed under the compression and bending modes are distributed more dispersed the compared to shear mode. Fig. 4.9(d & e) show the results of inter branch-crack angle ω and corresponding crack type distribution when comparing each fracture in terms of each corresponding struts. There are more through-strut fractures for the compression and bending modes compared to more across-strut fractures in the shear mode. In addition, fractures formed with these three different modes are all

randomly positioned on each strut (Fig. 4.9(f)). The branch length and branch thickness of the broken struts and the intact struts are also analyzed statistically for these three modes in Fig. 4.9(i-l). It shows no preference for the branch thickness for among the broken struts, but longer branches tend to break in all these three different cases. In terms of global damage spatial distribution, fractures under these three different modes are fitted into planes (shown as gray planes in Fig. 4.9(g)). The distance of each voxel on fractures is measured as d and compared to each individual mean branch length l_m for these three different modes. The distribution of the ratio d/l_m is shown in Fig. 4.9(h) that fractures formed under the shear mode are more aligned compared to the compression and shear modes. We could also tell from the connectivity of these three modes in Fig. 4.9(m) that fractures formed under the compression and bending modes are more connected compared to fractures formed under shear mode, indicating that the cracks are more likely to propagate to its adjacent struts in compression and bending.

Detected fragmentation regions are shown for both the compression and indentation modes in Fig. 4.10 (a) & (i) in light green color. The blue region shown in Fig. 4.10 (i) is the labelled ceramic tip with proposed algorithm. Then we overlap the fragmentation region with the previous damage stage (aligned and identified via DVC) to recognize the fragmentation boundary as the damage surface. Upper surface for compression mode and outer surface for the indentation mode are analyzed statistically. Damage surface is further registered to each individual strut and colored differently according to their orientation θ in Fig. 4.10(b) & (j) for these two modes. We could see that damage surfaces formed under the indentation mode (Fig. 4.10(j)) are more dispersed compared to the compression mode (Fig. 4.10(b)), as expected, but both of the two modes show dispersed in-plane rotation angle ϕ distribution in Fig. 4.9(e) & (k). Fig. 4.10(f) & (g) illustrate the results of inter branch-crack angle ω and corresponding crack type distribution for compression mode and display more through-struts

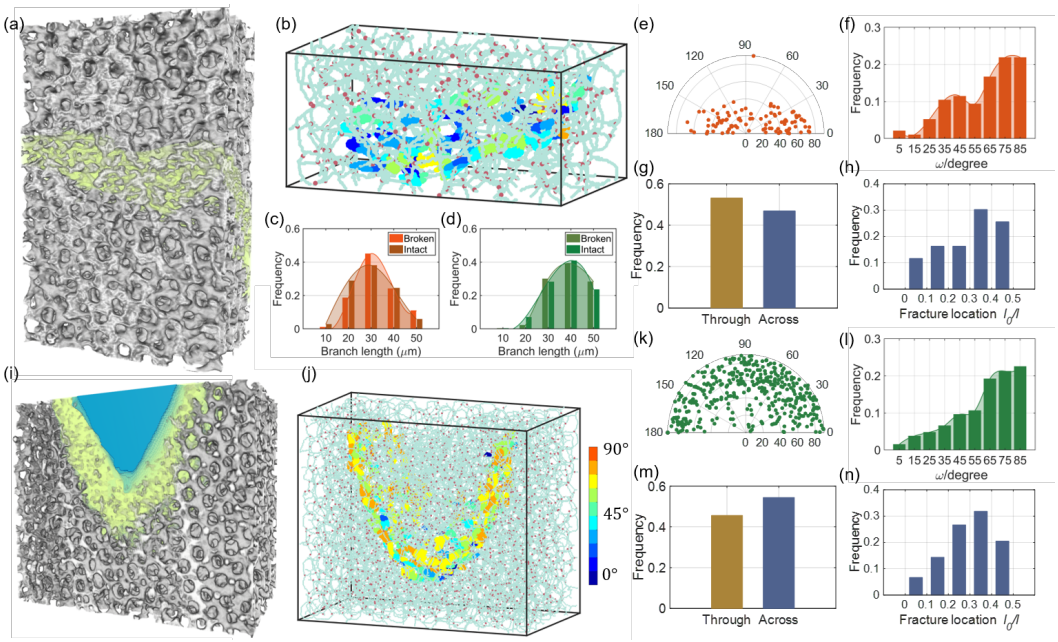

Figure 4.10: Fragmentation surface analysis results. (a) & (i) Detected fragmentation regions for both compression and indentation modes in light green color. The blue region shows the labelled ceramic tip. (b) & (j) Damage surface is registered to each individual strut and colored differently according to their orientation θ for compression and indentatin modes. Branch length distribution of broken struts and intact struts for (c) compression and (d) indentation modes. Distribution of (e) registered damage surface orientation, (f) inter branch-crack angle ω, (g) corresponding crack type distribution, (h) fracture location for compression mode, and Distribution of (k) registered damage surface orientation, (l) inter branch-crack angle ω, (m) corresponding crack type distribution, (n) fracture location for indentation mode.

damage surface, which is consistent with the fracture distribution under compression mode (Fig. 4.9(d) & (e)). Differently, damage surfaces under the indentation mode tends to be more across-struts as shown in Fig. 4.10(l) & (m). In addition, damage surface formed with both these two modes has no preference for the position on each strut (Fig. 4.10(h) & (n)). The branch length of the broken struts and the intact struts is also analyzed statistically for these two modes in Fig. 4.10(c) & (d). It shows no branch length preference of the broken struts for the indentation mode (Fig. 4.10(d)) but longer struts are more likely to break under the compression mode (Fig. 4.10(c)), which is similar to fracture preference for the

compression mode discussed before.

4.4 Conclusion

To summarize, we present a quantitative comprehensive framework to study the dynamic internal behaviors of cellular structure, which contains four modules: (i) In-situ synchrotron X-ray tomography, which enables collection of 3D microstructure in a macroscopic volume; (ii) Automated 3D damage features detection to recognize damage behaviors in different scales; (iii) Quantitative 3D structural analysis of the cellular microstructure, by which key morphological descriptors of the structure are extracted and quantified; (iv) Automated multi-scale damage structure analysis, which provides quantitative understanding of damage behaviors. We demonstrate a pathway toward efficient characterization of holistic damage information and robust quantitative way to represent mechanical behaviors in complex cellular structures.

For future work, the presented inspection pipeline will be extended to record the damage evolution process in more continuous mechanical tests by applying hybrid-dose measurement strategy. The whole characterization framework will be further applied to analyze the damage evolution process to establish the linkage among different mechanical test stages, which could provide important insights to study mechanical properties of the cellular structure. The comprehensive damage data can be directly used for quantitative and multi-scale damage modeling and simulation, paving the road towards quantitative material design for damage tolerance.

Chapter 5

Application to Unravel Pore Evolution Process in Binder Jetting printed Materials

5.1 Introduction

Recent years have witnessed the rapid development of various metal additive manufacturing (AM) technologies, from powder bed fusion, directed energy deposition, and binder jetting, to additive friction stir deposition, allowing for net-shaping of a broad range of metals and alloys [128, 129, 130, 131, 132]. However, AM also features a variety of defects like pores, internal micro-cracks, and air bubbles that can be present in massive quantities with heterogeneous distributions in the as-printed materials [131, 133], and is found to severely degrade the mechanical properties of the binder jetting samples [134]. The reliability of AM parts critically depends on our quality control capabilities, which allows for optimization that reduces or eliminates the defects [66]. This necessitates the development of advanced inspection schemes to enable complete volumetric examination on the macroscopic level as well as comprehensive understandings of the defect characteristics and their global evolution during AM and post-processing. There are still a number of substantial challenges for the Understanding defect evolution in current AM research [59, 135, 136], including: 1) high-

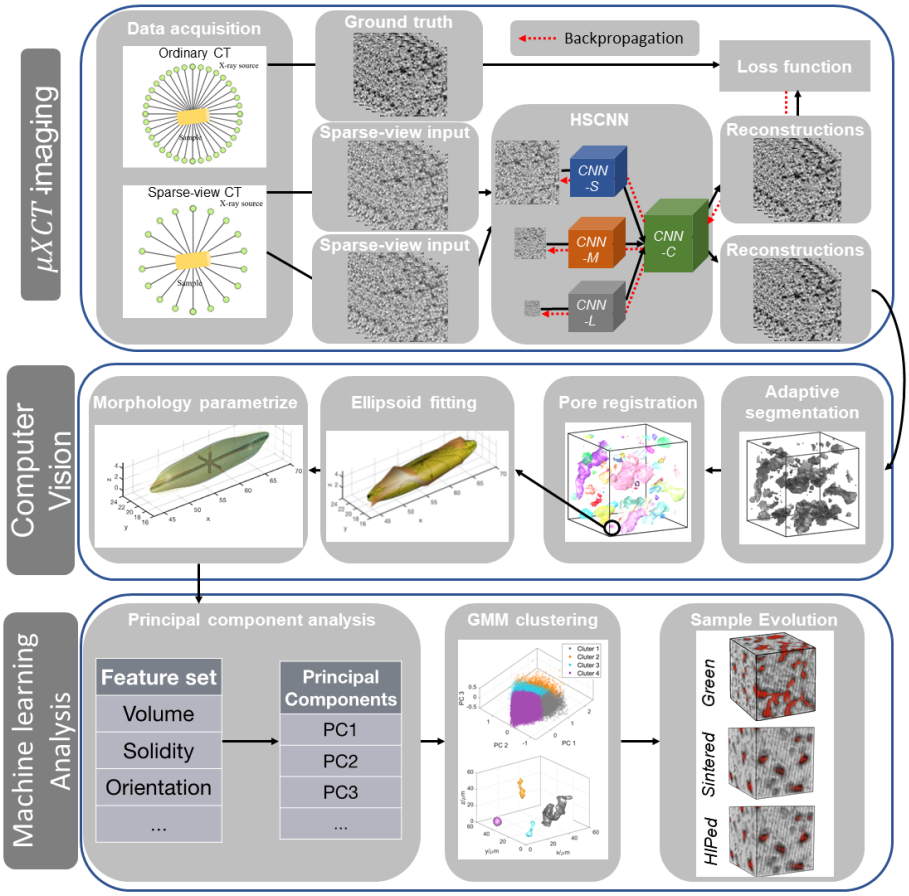

Figure 5.1: Framework of the 3D inspection pipeline for pore evolution in post-processing of additive manufacturing using binder jetting, including three major components of 1) X-ray micro-tomography data acquisition, 2) 3D morphological and statistical analysis, and 3) machine learning analysis. GMM stands for Gaussian mixture model.

throughput internal defects detection, 2) automated defect registration, and 3) large and complex defect datasets analysis in macroscopic samples.

To address the first challenge, we implement our developed fast tomography algorithm,

HSCNN, to collect high-resolution X-ray tomography data with only a fraction of the normal data acquisition time. This method enables major advancements compared to other available techniques, such as optical, scanning electron, or transmission electron microscopy. Detailed review of previous traditional techniques is included in the Section 1.4. However, high-resolution lab-based micro-tomography for large-scale sample is slow; it may take hours to characterize a millimeter-scale volume with micrometer-scale spatial resolution. Fast tomography is more describe to speed up the acquisition with high-quality volumetric data.

The second challenge stems from automated defect registration. While the high-resolution volumetric tomography data provides comprehensive structural information, the size of the dataset is massive (∼2-15 GB), involving a large quantity of 3D defects with morphological features spanning over several orders of magnitude. As a result, defect identification and characterization need to be automated with 3D morphological analysis algorithms. Some commercial software codes, such as FEI Avizo [137], and free image analysis software, such as ImageJ/Fiji [138], are employed to perform the semi-automated defect analysis for XCT data to provide some useful information of defects, such as porosity fraction, pore area/volume size, position, etc. in 2D slices or 3D volume. These pre-defined parameters, however, could not fully characterize the pores morphology features such as extrusion and necking. As a result, the capability for quantitative defect categorization and dynamic evolution analysis is limited. More comprehensive and reliable morphological characterization are needed with 3D analysis algorithms. Recently, there has been great interest in developing computer vision based automated inspection [139, 140, 141]; in particular, deep learning approaches have enabled example-based rather than conventional rule-based algorithms [24, 142]. Progress in this regard will facilitate automated 3D analysis approaches for advanced inspection in metal AM, which provides the solution for automated defect registration through employment of computer vision algorithms. The involvement of computer vision algorithms could

process large sets of X-ray tomography data for holistic defect registration and morphology parameterization more reliably and efficiently.

The third challenge lies in efficient data analysis of defects with complex shapes, where quantification of the morphology is essential to understand the global defect evolution during AM and post-processing. Currently, the defect information in AM is typically represented by a single metric, porosity, which is the volume fraction of pores [143, 144, 145]. The porosity can effectively describe the quality of AM parts only if the spatial distribution of pores is uniform and all of the pores are similar in sizes and shapes. It is also well known that porosity alone is insufficient to account for the part properties such as permeability, elastic anisotropy and fracture toughness [146, 147], which are highly dependent on the pore shape, orientation, and spatial distribution. Understanding the underlying correlations and trends for large defect datasets is therefore extremely important. Such quantification and assessment can be explored through statistical extremes, such as the maximum volume [148]. Here, we explore an alternative big data approach to extract evolutional features from the comprehensive dataset of all pores to address this challenge.

In this work, a new inspection approach for AM research in binder jetting materials is proposed, which integrates the recent advances in (i) fast tomography, (ii) 3D morphological analysis, and (iii) machine learning-based big data analysis. Here, we demonstrate this method by examining the post-processing in binder jetting additive manufacturing, which involves substantial global pore evolution from the green state, to the sintered state, and to the hot isostatic pressed (HIPed) state. We use copper as a model system, which is difficult to print using powder bed fusion and directed energy deposition due to the high reflectivity and high thermal conductivity [149], but are readily printed by binder jetting with good quality—as long as the internal pores can be effectively reduced via post-processing. We show that the approach is effective at detecting and handling the information associated

with the large number ($\sim 10^5$) of pores in macroscopic samples, and the pore morphology can be sufficiently represented by a few morphological descriptors based on principal component analysis (PCA). The detected pores are found to be best categorized into four morphological groups, including quasi-spherical pores, small elongated pores with high solidity (a.k.a. convexity, which is used to quantify the amount of concavities of a shape within in its convex boundary.), large elongated pores with low solidity, and reticulated defects. By quantifying the evolution of the pore morphological parameters and the weight of each categorized morphological group, we find a reduction in the pore size and eccentricity after sintering and HIP. During sintering, the interconnected reticulated defects break up into smaller pores, while the HIP process is more effective at reducing the size and increasing the solidity of the isolated pores.

5.2 Methods

The proposed pipeline consists of three modules: (i) fast micro X-ray computed tomography, which enables quick collection of 3D defect data in a macroscopic volume using sparse-view tomography techniques; (ii) automated 3D morphological analysis, based on which the collected data is processed for defect registration and morphology parameterization; (iii) principal component analysis and clustering analysis, by which key morphological descriptors of the defects are extracted and the defect morphology evolution is quantified during post-processing. Fig. 5.1 depicts a flowchart for the three modules and their connections.

5.2.1 Micro X-ray computed tomography (μXCT)

Global-scale AM characterization necessitates efficient and accurate acquisition of the 3D morphological data of defects. A tomographic scan is performed to acquire projection images of the object from different viewing angles. In this work, full view construction is first performed in µXCT characterization of the binder jetted samples. To reduce the data acquisition time, we also explore fast tomography, in which a hierarchical synthesis convolutional neural networks (HSCNN)-based reconstruction algorithms is used to enhance the imaging quality from sparse-view CT, as illustrated in Fig. 5.1. Implement detail related to HSCNN algorithm is discussed in Chapter 2.

5.2.2 Automated 3D morphological analysis for pore morphology parameterization

To register the defects and parametrize their 3D morphology, the raw voxel-based 3D data from µXCT (∼2 GB) is processed using computer vision algorithms. First, the voxel brightness distribution is sorted and fit to an expectation function of a bimodal Poisson model [150], where the mean brightness of the expectation function is set to be consistent with the density of the measured sample. This step removes unevenness from background illumination. Second, an adaptive segmentation algorithm is implemented to differentiate low-density regions (pore or binder domains) from high-density regions (metal) [151]. This step binarizes the gray-scale images to reduce the data size by three orders of magnitude (from 2 GB to 400 MB). Last, each potential pore region is identified from the 3D binary data using connectivity analysis, and the target regions are extracted and cross-referenced with the gray-scale dataset. If the potential pore is well padded (i.e., surrounded by a gradual transition region), it will be considered as a true pore and will be registered. Otherwise, it

will be considered as an artifact and ignored. The output of this step is a full list of registered pores, which will be stored as connected voxel clusters.

The registered 3D pores are then parametrized to form a morphology data pool F, which are registered with the variables summarized in Table 5.1. For each pore, we first register the volume v based on the number of voxels and then register the surface area s by fitting the pore surface with triangular meshes [47]. The pore shape and orientation are determined based on ellipsoidal representation. Such geometrical approximation allows us to register the principal axis length (a, b, and c), the axis orientation (θ and ϕ), the centroid location (x_o, y_o, and z_o), and the bounding box size (x, y, and z) of each pore. Finally, we characterize the pore solidity using convex hull. The convex hull of a closed region is the smallest convex set that contains the region. The volume of each convex hull is recorded as v_{hull}. The corresponding solidity can be measured by the ratio between the actual volume and convex hull volume: v/v_{hull}. Solidity effectively characterizes the pore shapes in terms of convexity, which quantifies ratio of concavities of a shape in comparison to its convex bounding hull volume. High solidity means the volume is more convex and low solidity means there are more concave boundaries. For a spherical pore, the actual volume is the same as the convex hull volume and the solidity is 1. For a pore resulting from a network of multiple narrow particle gaps, the convex hull volume is much larger than the actual volume, and the solidity is much smaller than 1. The holistic morphology data allows for statistical analysis of pore size, eccentricity, and orientation distributions.

Table 5.1: Registered pore morphology variables

Elliptical representation				Voxel & Mesh fitting		Convex hull
Centroid coordinates	Orientation	Principal axis lengths	Bounding box size	Volume	Surface area	Volume
x_o, y_o, z_o	θ, ϕ	a, b, c	x, y, z	v	s	v_{hull}

5.2.3 Principal component analysis and clustering analysis

Morphology parameterization of all pores in the entire specimen allows for objective feature selection without sampling bias using big-data analytical tools. In this module, we aim to find the key descriptors that most efficiently represent the morphology variations among the pores, and characterize the pore evolution within the key descriptor domain through principal component analysis (PCA) [152].

Formally speaking, given the N morphology parameters for M pores, we register the N×M matrix $F = f_{ij}, i = 1, ...N, j = 1, ...M$ to establish a pore morphological feature library. The PCA method generates the uncorrelated orthogonal basis set $P = P_i, i = 1, ...N$—the principal components, where each P_i is a linear combination of the N feature variables in F. Selecting the first few P_is allows for the optimal preservation of the morphology differences with a reduced representation. The reduced PC domain provides a natural basis to describe the morphology evolution of pores.

Finally, we categorize the pores into different morphological groups by identifying clusters that are maximally separated in the reduced PC domain. This is achieved through the Gaussian mixture model (GMM) clustering [153, 154], which fits the dataset into multi-variate normal components that maximize the component posterior probability. The optimization algorithm involves iteratively updating cluster centroid, covariance matrices, and mixing proportion, and assigning data points to the clusters with the maximum expectation [155]. As compared to other clustering methods such as k-means [156], GMM clustering provides a universal framework that allows us to compare different clustering numbers and covariance structures. Two information criteria are employed, Akaike information criterion (AIC) and Bayesian information criterion (BIC) [157], to evaluate the effectiveness and accuracy of the clustering models. Here we employ the minimization of AIC and BIC to choose an adequate

clustering model that represents the dataset without exceeding complexity. This analysis enables quantification of the major trend of global defect evolution based on objective, data-driven approaches.

5.3 Results and Discussion

5.3.1 Material and experimental setup

Copper samples were additively manufactured using binder jetting, followed by several post-processing steps. The copper powder used in this study was spherically shaped featuring a bimodal diameter distribution with peaks at 5 µm and 30 µm. The two types of powders were mixed in the ratio of 27:73 by weight using a low energy ball mill for 2 hours. Binder jetting additive manufacturing was conducted using an ExOne R2 3D printer at a layer thickness of 70 µm. Standard binder PM-B-SR2-05 provided by ExOne was used at a 100% binder saturation value. More details of the AM parameters were elaborated elsewhere [158, 159].

The green copper sample consisted of two phases: loosely packed copper particles and numerous binder domains [160]. The first step in post-processing was de-binding, which was carried out at 450 °C (53% melting temperature of copper) for 0.5 hour in a reducing hydrogen environment. The second step was sintering, which was carried at 1075 °C (99% melting temperature of copper) for 3 hours in the same environment. The third step was hot isostatic pressing (HIP), which was carried out at 1075 °C under an argon pressure of 206.84 MPa for 2 hours. Three experiments were performed under the same binder jetting conditions but were stopped at different steps of post-processing. Experiment 1 involved no post-processing; Experiment 2 involved de-binding and sintering; Experiment 3 involved de-binding, sintering, and HIP. The three corresponding samples were labeled as 'green',

'sintered', and 'HIPed' respectively.

For each copper sample, the 3D defect morphology was scanned using a laboratory-based micron-scale X-ray tomography platform (ZEISS Xradia Versa 520, Carl Zeiss X-ray Microscopy Inc., Pleasanton, CA) with a macroscopic volume of $2 \times 2 \times 2mm^3$. Tomographic scan is implemented with the voltage of 160 KeV and the current of 200 µA. In the full-view configuration, 3201 projections are performed for high-quality reconstruction, which takes around four hours. For sparse-view tomography, only 201 projection images were scanned for each sample with the same operating parameters. The sparse-view scan took around 15 minutes, approximately 16 times of reduction compared to full-view experiment. For sparse-view reconstruction, the HSCNN algorithm is performed to improve reconstruction quality. We crop 1740 patches with the size of 256×256 pixels randomly from the first 100 sparse-view reconstructed images and corresponding full-view reconstructed images as the network datasets; 80% are used for training, and the rest are used for testing. The training of the network is implemented on MATLAB 2018b (Mathworks, Natick, MA, USA). The trained network is then used to enhance the rest, untrained slices by translate each patch in the new slice into the enhanced output. These output patches are stitched accordingly to retrieve the reconstruction result. The processor is Intel Core i7-6700K, the memory is 32 GB, and the GPU is one NIVIDIA GeForce GTX 960 card. In this configuration environment, it takes about 6 hours to train samples over the network for one type of data. Once trained, it takes around 4 seconds for the translation of one full slice.

All the post-processing, including the Automated 3D morphological analysis for pore morphology parameterization, Principal component analysis, and clustering analysis, were performed on MATLAB 2018b (Mathworks, Natick, MA, USA).

5.3.2 Sparse-view X-ray tomography reconstruction via HSCNN

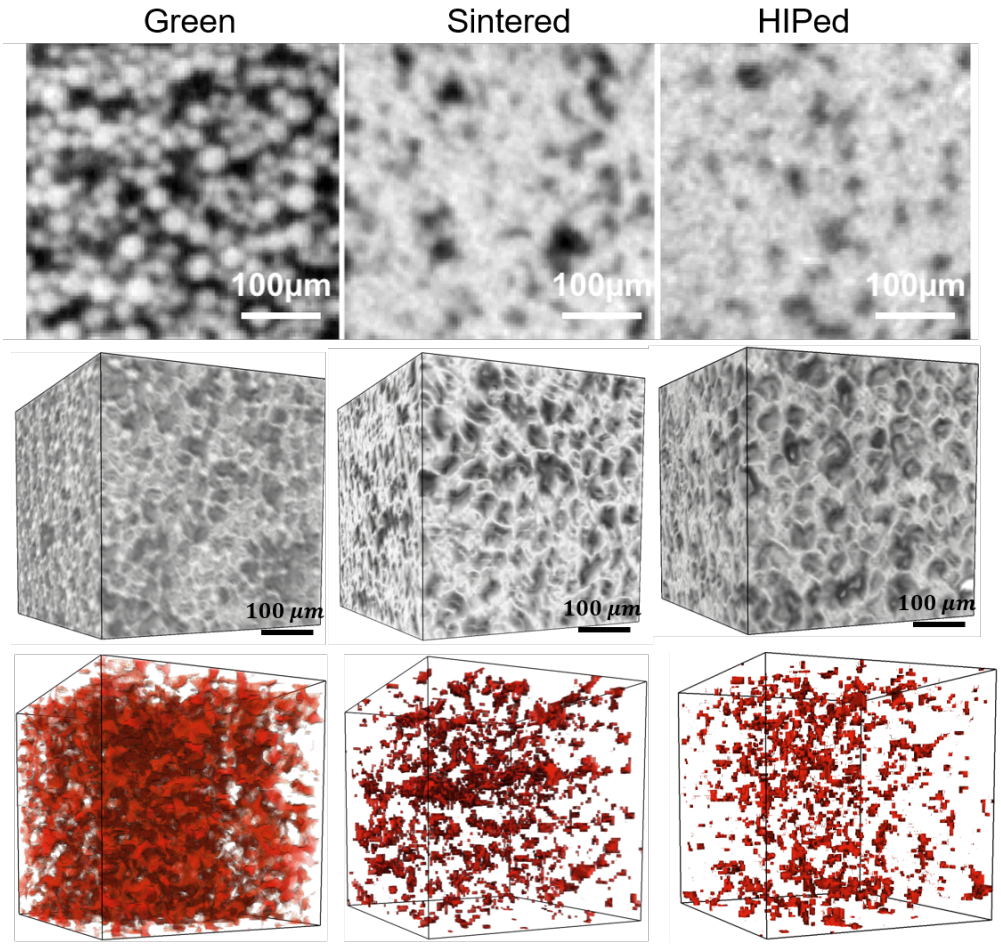

Figure 5.2: Results of the μXCT imaging in 2D and 3D representation, and pore extraction. Slices of cropped region with different magnification are shown for the green, sintered, and HIPed samples, respectively. and pore extraction. Slices of cropped region (1st row) are shown for the green, sintered, and HIPed samples, respectively. 3D volumetric renderings are shown for (2nd row) raw µXCT reconstruction, and (3rd row) extracted pores only, respectively.

The µXCT reconstruction results are shown in Fig. 5.2 as 2D slices and 3D volumetric renderings for the green, sintered, and HIPed samples. It should be noted that the pores are filled with binder in the green sample but are not in the sintered and HIPed samples. For convenience, in all the cases we use 'pore' to refer to the space that is not filled by

copper, regardless of whether it is filled by the binder. The morphology evolution of the

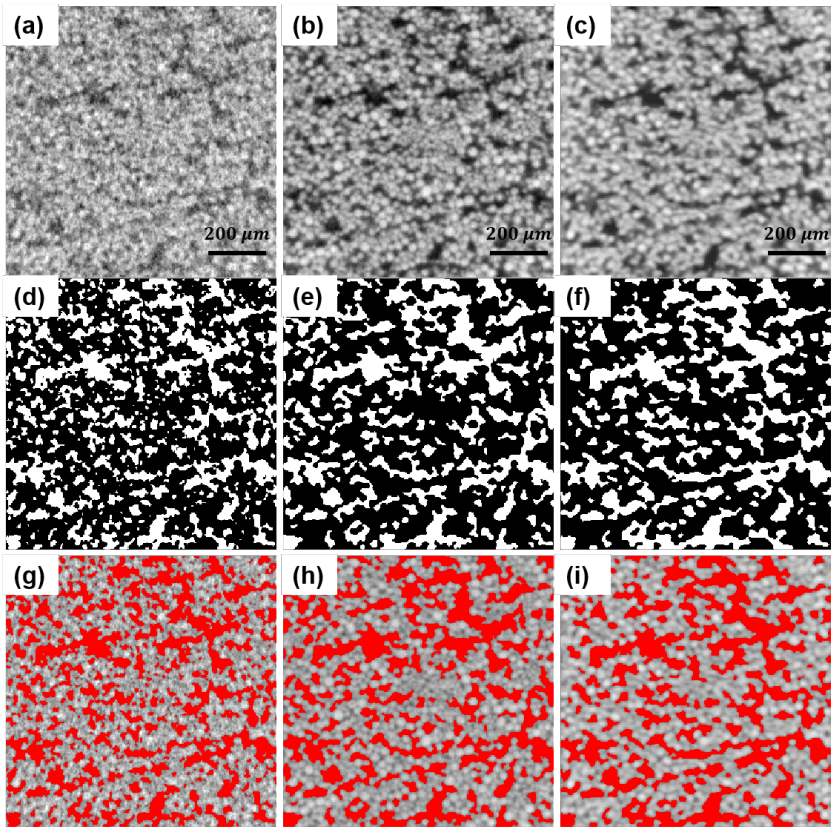

Figure 5.3: Fast tomography reconstruction for the green sample. The left column figures ((a), (d), (g)) represent the sparse-view reconstruction results. The middle column figures ((b), (e), (h)) represent the ground truth from the full-scan reconstruction. The right column figures ((c), (f), (i)) represent the high-fidelity reconstruction through deep learning based on sparse-view reconstruction. The 1st, 2nd, and 3rd row show the original gray-scale reconstruction results, the corresponding segmentation results, and the corresponding pore extraction results, respectively.

pores can be identified from the reduction of porosity and pore sizes. In the green state, there are numerous pores, which are generally elongated, irregularly shaped, and in some cases highly interconnected. Quantitative analysis confirms that the percentage of such reticulated defects make up over 90% of the relative pore volume fraction. After burn-out of the binders and sintering, the part has significantly increased its density, and network-

like interconnected pores are seen to break up into a large number of more isolated pores (from 22,912 in green sample to 54,739 in sintered sample). After the final post-processing stage (HIPed), many small pores disappear, leading to reduction in the total number of pores (40,018 in HIPed sample). The mean pore size is decreasing during this process (from $20,322\mu m^3$ in the green sample to $14,593\mu m^3$ in the sintered sample, and to $4,842\mu m^3$ in the HIPed sample). A change of the pore shape is also observed—the pores become more spherical, which is reflected in the increase of solidity (from 0.6532 in green to 0.6840 in sintered sample, and to 0.7026 in the HIPed sample). Overall, after each post-processing step, it is evident that the pores become smaller in size. It is also observed that the smaller pores are generally more spherical and closed in shape.

The effectiveness of the fast X-ray CT algorithm is demonstrated for the green sample. Fig. 5.3 shows a comparison between (1) the sparse-view reconstruction (based on 201 projections), (2) the full-view reconstruction (based on 3201 projections), and (3) the corresponding enhancement using the HSCNN algorithms discussed in Section 2. Clearly, the blurring and streak artifacts shown in the sparse-view reconstruction have been effectively removed. Validation on a number of slices also proves that the pore registration results from the enhanced sparse-view reconstruction (i.e., the 3rd column) are very close to that from the full-view reconstruction (i.e., the 2nd column). Quantitatively, the MSE between sparse-view reconstruction result (Fig. 5.3 a) and the ground truth reconstructed from full-view CT (Fig. 5.3 b) is 0.0073. This error is reduced to 0.0030 (Fig. 5.3 c), while the SSIM increases from 0.5439 to 0.7407 with the HSCNN algorithm. We also compared the 2D porosity fraction and pore size results based on extracted pores of these three slices (Fig. 5.3d-f). While the total porosity of the three slices are obtained as 33.08%, 33.52% (ground truth), and 33.44% for sparse-view and full-view reconstruction using traditional FBP algorithm, and sparse-view reconstruction from HSCNN algorithm, respectively, the

distribution of pore sizes is more accurately captured with HSCNN. There are 320 pores in the sparse-view reconstruction result (Fig. 5.3 d), 112 pores (ground truth) in the full-view reconstruction (Fig. 5.3 e), and 115 pores in the sparse-view reconstruction with HSCNN algorithm (Fig. 5.3 f). The mean pore area of these three slices are 931 μm^2, 2696 μm^2(ground truth), 2619 μm^2, respectively. These quantitative comparisons indicate the reliable and efficiency of HSCNN algorithm for sparse-view CT reconstruction. With reduction in the number of projection measurement by a factor of 16, we have been able to obtain the high-resolution CT scan within 15 minutes, as compared to 4 hours of data acquisition in full-view reconstruction.

While the developed fast tomography method for enhanced sparse-view reconstruction works well for the green sample, the performance is less impressive for the sintered and HIPed samples. The spherical shape of the as-printed particles provides a strong prior structural feature for the fast tomography reconstruction for the green sample, but this feature becomes substantially weaker after sintering and HIP as individual particles are merged through surface diffusion. In the following analysis, therefore, the fast tomography approach is used for the green sample, whereas the full-view tomography approach is used for the sintered and HIPed samples.

5.3.3 Morphological and statistical analysis results

The collected X-ray imaging data of copper samples is processed to yield a total pore number of 117,669, including 22,912 pores in the green sample, 54,739 in the sintered sample, and 40,018 in the HIPed sample. Pore morphology is parameterized for all pores using the approach elaborated in Section 5.2.2. Based on the pore morphology database, a statistical analysis is implemented. The porosity of the green, sintered, and HIPed sample is measured

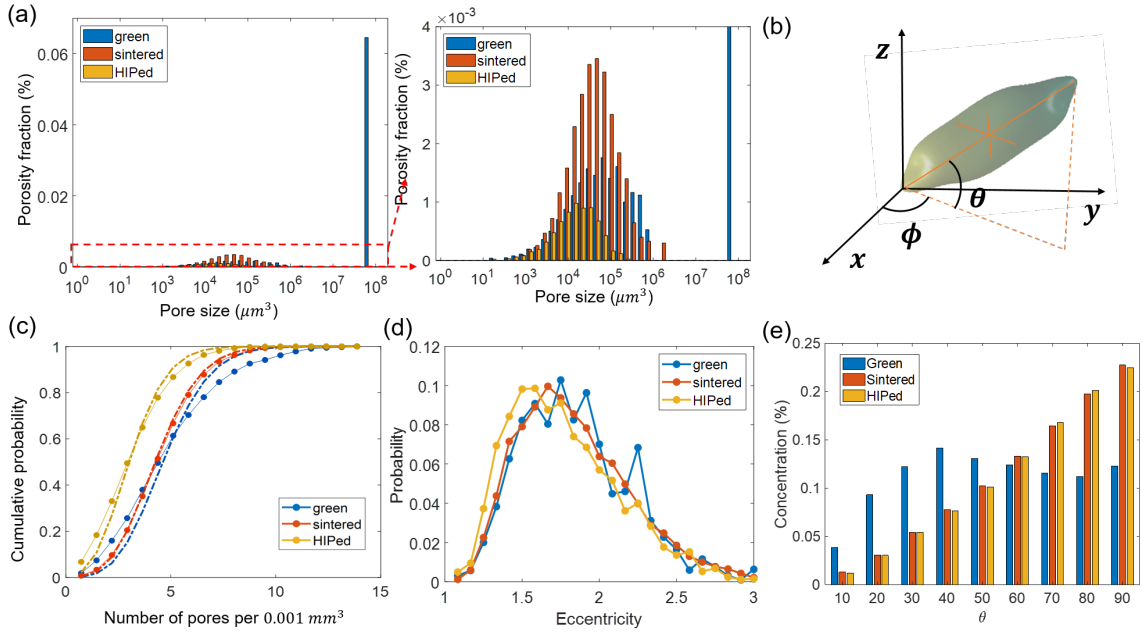

Figure 5.4: Statistical analysis results for the pores in the green, sintered and HIPed samples respectively. (a) The porosity fraction distribution of pore size (represented by the pore volume). Note that the singularity peak on the right represents a large interconnected pore in the green sample. Also shown is a 'zoom-in' view of the porosity fraction distribution without the singularity peak. (b) Definition of the azimuth angle ϕ and the altitude angle θ. (c) Cumulative probability distribution of the pore number density. (d) Probability distribution of eccentricity. (e) Probability distribution of the altitude angle .

as 37.90%, 3.43%, and 0.89%, respectively. This 3D pore analysis is consistent with measured the density of the samples via the conventional Archimedes method for the sintered and HIPed samples, which are 94.5% and 99.07% of density, respectively. Fig. 5.4 (a) shows the evolution of pore size distribution, which consistently shifts to the smaller side (left) from the green sample to the sintered and to the HIPed sample. Notably, the green sample features a singular, massive interconnected void that is shown as a single bar on the far right in the histogram plot. Originating from the pore network interconnected throughout the entire sample, the giant defect accounts for 35% of the total pore volume. After sintering, this massive singular defect breaks up into a large number of smaller pores. We will use the machine learning analysis to further quantify pore decomposition to identify correlated

morphology changes in addition to the volume reduction (Section 5.3.4). Fig. 5.4 (c) plots the distribution of pore number density (calculated as the number of pores per $1 \times 10^{-3} mm^3$) based on cumulative probability to evaluate the randomness of spatial distribution for the pores. For randomly distributed pores, the volumetric density distribution should follow Poisson's distribution. When comparing the detected pore number density (dotted lines) to the Poisson's distribution (dashed lines), the sintered and HIPed samples demonstrate good fitting, indicating that pore size distribution in these two samples is approximately random. The density distribution of the green sample significantly deviates from the Poisson's distribution, which is likely due to the influence by the printing trajectory. Fig. 5.4 (d) plots the evolution of pore eccentricity, e_l, which is defined as the ratio of the longest principal axis to the equivalent radius. Going from the green to the sintered, and to the HIPed sample, a left-ward shift of the curve is observed, indicating less eccentric, or more spherical, pore shapes after post-processing.

The orientation of each pore is defined as the direction along the longest axis of the ellipsoid. As shown in Fig. 5.4 (b), the 3D orientation is represented by the altitude angle θ (the angle of the orientation vector with respect to the vertical axis or the build direction) and the azimuth angle ϕ (the angle of projected orientation vector on the horizontal plane with respect to the reference of x axis). A small altitude angle θ close to 0° indicates that the pore is vertically orientated, while $\theta \sim 90^\circ$ represents a pore that is flat on the horizontal plane. The registered data of the altitude angle and azimuth angle is statistically analyzed. Fig. 5.4 (e) compares the distribution of the altitude angle θ among samples at different post-processing stages. In the green sample, the altitude angle appears to distribute randomly between 90° (i.e., within the print layers) and 0° (vertical to the print layers), without obvious orientation preference. However, in both sintered and HIPed samples, it is observed that the pore orientation is more closely aligned with the printing plane, as evident by the distribution peaks at 90°.

The apparent difference of the pore orientation between the green and the post-processed samples may stem from the particle rearrangement during sintering, in which more particles fall down and shrink the pores along the vertical direction. Note that there is no evidence of gravity playing a role in the large-scale heterogeneity of the pore distributions in the sample, it is only observed locally that particles tend to fall closer vertically than move closer horizontally under the influence of gravity. This gravity-influenced particle rearrangement has been observed in similar granular systems as well and is likely to be responsible for the anisotropy of pore orientation after sintering [161]. As a result, the pores are more likely to be flattened out on the horizontal plane with larger altitude angles. The altitude anisotropy is not significantly altered after the HIP process, which can be attributed to the application of isotropic pressure.

5.3.4 Quantitative pore evolution analysis using machine learning

Principal component analysis

The first step in analyzing global defect evolution is to extract the key morphological descriptors for the pores. These key morphological descriptors enable quantitative representation of the pore morphology with reduced dimensions. To implement the PCA analysis, the morphology data in Table 5.1 is re-scaled to yield a normalized dataset. This standard procedure improves the numerical stability and avoids the emphasis on certain variables with extreme values, and is commonly used [162].

The PCA analysis results are shown in Fig. 5.5(a)&(b). It can be seen that the combination of volume and eccentricity is of primary importance to PC1 and PC2, which account for 55% and 24% of the explained variance respectively. Interestingly, PC3 (12% of the explained variance) almost entirely consists of the altitude angle. This indicates that the inclination

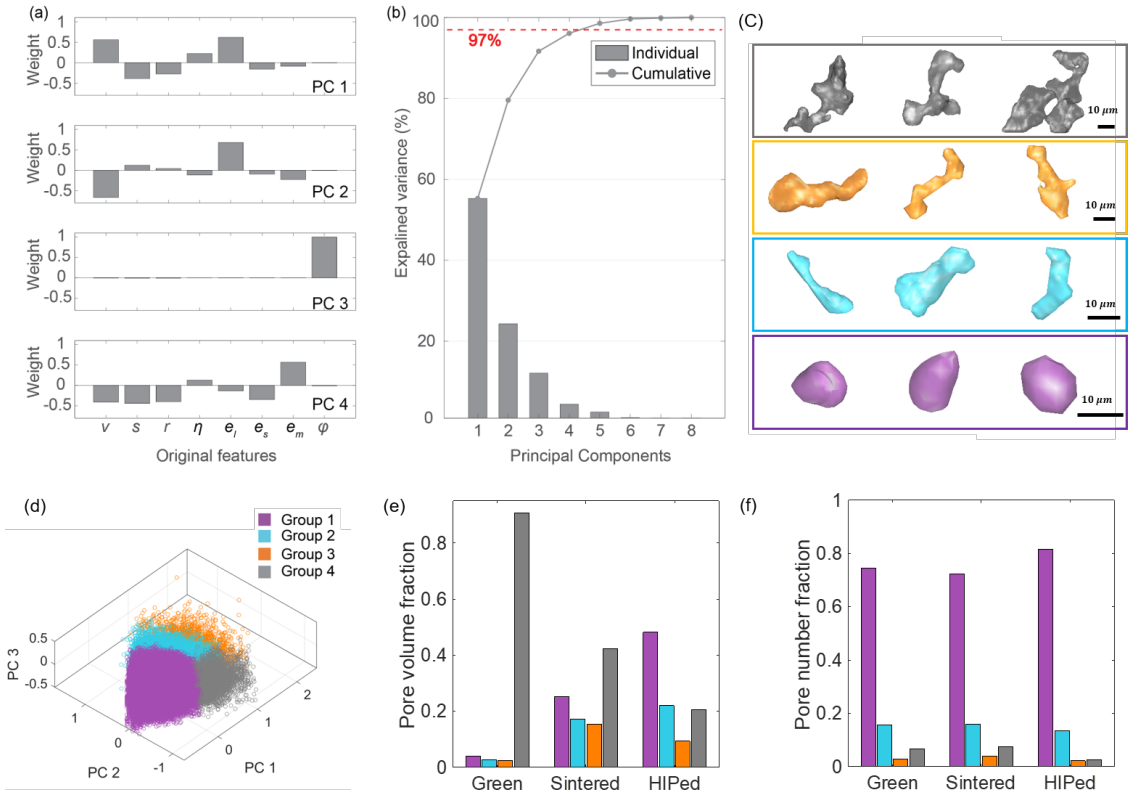

Figure 5.5: Principal component and clustering analysis results. (a) The first four principal components shown as weight of the linear combinations of the eight morphology parameters. (b) Explanation level of each principal component. The first four PCs explain around 97% variance in the original morphological data. (c) Examples of representative pores in each group and (d) four identified pore groups shown in the three-dimensional PC domain. Quantitative evolution of (e) pore number fraction and (f) relative volume fraction for the four pore groups

angle is uncorrelated with other morphological features. Overall, decomposition into the first four PCs accounts for 97% of the explained variance, or morphology differences, of all the registered pores, whereas the trailing principal components represent the morphological features of the pores that stay unchanged during the post-processing. For the purpose of pore evolution analysis, we focus on the leading PC to describe the most salient changes. The following analysis is based on the reduced 4-PC representation.

Clustering analysis

After PCA, clustering analysis is implemented in the reduced 4-dimensional PC space using GMM clustering. To determine the optimal cluster number, such analysis has been performed for scenarios of various cluster numbers (with cluster number of 1 to 8). The clustering results are evaluated by two information criteria, AIC and BIC. It is found that the best classification with the smallest intra-cluster covariance is achieved at the cluster number of 4. In other words, the detected pores in all three binder jetted copper samples are best categorized into four morphological groups.

For visualization, the clustered data points are plotted in the 3D space spanned by PC1, PC2, and PC3 in Fig. 5.5(d). For the subspace defined by each cluster, the data points at the center of the subspace represent the typical morphology of the corresponding pore group. Fig. 5.5(c) shows the typical 3D pore morphology for each of the four groups, which can be interpreted as:

- Group 1: quasi-spherical pores. These pores are predominately classified by their small volume (0.32±0.39 e4 μm^3), low eccentricity (e_l:1.51±0.21,e_m:0.97±0.10,e_s:0.70±0.09), high solidity (0.76±0.13), high volume ratio (0.35±0.13), and absence of sharp edges or extrusions. Pores meeting these classification criteria are the most numerous in the detected samples.
- Group 2: small elongated pores (volume: 0.97±0.41 e4 μm^3) with high solidity (0.51±0.13). These pores are characterized by eccentric structures but without significant extrusions, which results in high solidity (e_l:2.13±0.19,e_m:0.84±0.10,e_s:0.57±0.06).
- Group 3: large elongated pores (volume: 3.61±0.52 e4 μm^3) with low solidity (0.36±0.12). These pores are usually elongated, displaying a lot of extrusions and necking that result in low solidity (e_l:2.55±0.27,e_m:0.77±0.09,e_s:0.52±0.06).

- Group 4: reticulated defects (volume: 5.56±1.58 e4 μm^3, solidity: 0.33±0.12). Characterized by a tortuous, network topology, these defects are composed of large packing voids that are interconnected. The average volume of these defects is larger than that of any previous group (e_l:1.63±0.19,e_m:1.05±0.13,e_s:0.59±0.09).

Quantitative evolution of the pore morphology

We next use the clustering basis to quantify pore morphology evolution in Figs. 5.5(e) and (f) to present the quantitative evolution with respect to pore number fraction and relative pore volume fraction (given pore volume/total pore volume). In terms of pore number fraction, Group 1 pores are of the largest number in all stages (green, sintered, or HIPed), as shown in Fig. 5.5(e). In terms of relative pore volume fraction, however, the weight of each pore group changes significantly during the post-processing stages, as shown in Fig. 5.5(f). We observe a steady reduction of the reticulated defects (Group 4) throughout the post-processing stages. In the green sample, the reticulated defects make up over 90% of the relative pore volume fraction, despite being less than 10% of the pore number fraction. The relative pore volume fraction of the reticulated pores decreases to 42.3% after the sintering, and further decreases to 20.5% after HIP. The reduction of the reticulated pore is accompanied by the steady increase of the quasi-spherical pores (Group 1), from 4% relative volume fraction in the green sample to 25% in the sintered sample, and to 48% in the HIPed sample. Overall, during post-processing of binder jetting the main source of porosity shifts from Group 4 (>90% relative pore volume fraction in the green sample) to Group 1 pores (48% relative pore volume fraction in the HIPed sample). On the other hand, the behavior of Group 2 and Group 3 pores is not characterized by a simple trend, involving an increase of number fraction and relative volume fraction by the sintering process, and then a decrease of number fraction after the HIP process.

5.3.5 Physical insights from data analytics

The data analytical results in section 5.3.4 provide quantitative physical insights into pore evolution during the post-processing of binder jetting. Initially, the binder infiltrates among the loosely packed particles, forming large and mostly interconnected gaps. The green sample is observed with a high porosity of 37.90%, which is predominately a result of these reticulated defects. The reticulated defects (Group 4) consist of tortuous, interconnected voids, and typically contain multiple narrow regions among particles in contact. During sintering, neighboring particles form neck structures at the contacting locations as a result of densification diffusion. The growth of the neck structure brings the particles closer together with overall pore shrinkage [163]. At the same time, neck growth of the particle contact can lead to breakup of the interconnected pores and future decomposition of large pores, resulting in more discontinuous pores that belong to Group 2 and Group 3. The pore shrinkage and pore breakup explain the increased number and average size of Group 2 and Group 3 pores after the sintering step, despite the overall shrinkage of pore sizes. It is also observed that the orientation of the pores favors the horizontal direction after sintering, indicating that a greater degree of shrinkage occurs along the vertical direction. This anisotropy is considered to be a result of particle rearrangement under the influence of gravity during sintering. These findings are consistent with previous studies based on the 2D characterization of pores [131, 161, 164].

During the final stage of HIP, the pore morphology is observed to favor isolated and geometrically regular pore classifications (Groups 1 and 2). These results can be explained by the continuation of particle neck growth via surface diffusion, which is accelerated by the isostatic pressure during HIP. Intense, isotropic diffusion during HIP introduces future decomposition of large pores into small pores with high solidity. At the same time, it also smooths the pore shape and further reduces the pore size. As a result, the solidity continu-

ously increases and eccentricity decreases during HIP, i.e., pores become steadily smoother and more isotropic. The orientation of the pores remains largely unchanged during the HIP process, suggesting that gravity is no longer influential in the presence of isostatic pressure from all directions. At the final stage of pore evolution, small quasi-spherical pores may shrink below the threshold of µXCT detection or completely close up, leading to the substantial reduction of pore number at the end the post-processing. These pore morphology evolution mechanisms are illustrated in Fig. 5.6.

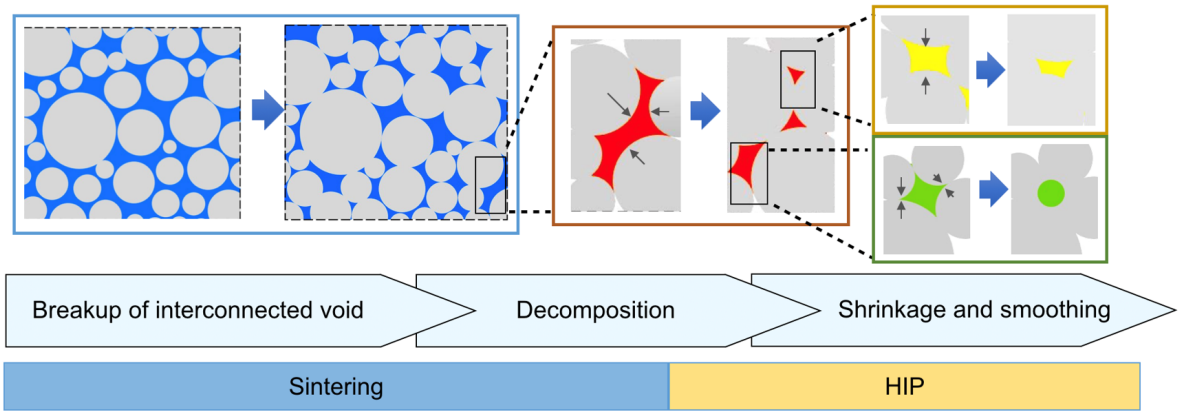

Figure 5.6: Pore morphology evolution mechanisms during the post-processing of sintering and HIP in binder jetting. The blue, red, yellow and green colors represent the four pore evolution patterns of 1) pore segmentation due to densification of loose particles, 2) decomposition of interconnected pore due to neck growth, 3) pore shrinkage and 4) pore smoothing.

5.4 Conclusion

To summarize, we have presented a new inspection pipeline to characterize the defect evolution in post-processing of binder jetting. Through the integration of fast tomography, 3D morphology analysis and machine learning, we demonstrate a pathway toward efficient acquisition of holistic defect information and robust morphological representation.

For future work, the presented inspection pipeline can be improved in several aspects. The framework can be validated with porosity data from other established methods, so that the accuracy and traceability can be quantified. The resolution of the µXCT tomography can be improved to the sub-µm level, to include small pores and resolve sharp peaks at the boundary of the pores. More effective deep learning algorithms can be developed for fast tomography to reduce the data acquisition time. More advanced data analytical tools can be incorporated, e.g., to better represent the topology of network defects, and to include the potential interaction of adjacent pores.

Chapter 6

Conclusions and Future Work

6.1 Conclusions

In this thesis, data-driven based deep learning algorithms are utilized to improve the reconstruction results from the image and measurement domains to improve fast tomography with reduced training data. The developed algorithms are applied for image reconstruction and data-processing for different cases combined with advanced computer vision-based image analysis and machine learning-based big data processing. To summarize:

Chapter 2 introduces the hierarchical synthesis CNN (HSCNN), which is a knowledge-incorporated data-driven tomographic reconstruction method for sparse-view tomography with split-and-synthesis approach. The learning scheme is robust against sampling bias and aberrations introduced in the forward modeling. This proposed learning-based method informs the forward model biases based on data-driven learning but with reduced training data size.

Evaluation on both numerical simulated and experiments was conducted to demonstrate the feasibility of the proposed method. High-fidelity X-ray tomographic imaging reconstruction results are achieved with a very sparse number of projection angles. Comparison with both conventional non-learning-based algorithms and advanced learning-based approaches shows improved accuracy for our method. We also prove the importance of splitting strategies

by showing the reconstruction results from different splitting methods. As a result of the split-and-synthesis strategy, the trained network is transferable to new cases.

Chapter 3 presents a deep learning-based enhancement method, HDrec, for low-dose tomography reconstruction via a hybrid-dose acquisition strategy composed of extremely sparse-view normal-dose projections and full-view low-dose projections. The training is applied on each individual acquisition without the need of additional high-fidelity tomographic scans. Evaluation on two experimental datasets under different hybrid-dose acquisition conditions show significantly improved structural details and reduced noise levels compared to uniformly distributed acquisitions with the same number of total dosage. The resulting reconstructions also preserve more structural information than reconstructions processed with conventional analytical and regularization-based iterative reconstruction methods from uniform acquisitions. In addition, we provide a strategy to distribute dosage smartly with improved reconstruction quality. When total dosage budget is limited, the strategy of fewer normal-dose projections in combination with not-too-low full-view low-dose measurements greatly outperforms the uniform distribution of the dosage.

Chapter 4 applies the proposed data-driven X-ray tomographic imaging reconstruction techniques, HSCNN in chapter 2 and HDrec in chapter 3, to dynamic damage behaviors characterization in the cellular materials, which has the potential to improve the data acquisition speeds to record internal structure changes. A quantitative dynamic damage evolution characterization pipeline is then proposed in the local and global scales after the proposed fast tomography reconstruction algorithms to reduce labor of manual-labelling, including:

1. Deep learning-based algorithms for damage feature detection in the local and global scales to reduce labor of manual-labelling,
2. Computer vision-enabled 3D structural analysis of the cellular microstructure,
3. Autonomous multi-scale damage structure analysis by correlating to the cellular mi-

crostructure.

Deep learning-based algorithms are implemented to recognize damage features in different scales. A quantitative 3D cellular network analysis pipeline is developed for a multi-scale structural representation and quantification of biological cellular materials. New understandings are developed regarding registered damage regions with this developed quantitative analysis framework.

Chapter 5 implements the proposed data-driven X-ray tomographic imaging reconstruction techniques, HSCNN in chapter 2, to unravel pore evolution in the binder jetting printed materials. Through the integration of 1) fast tomography reconstruction techniques HSCNN, 2) automated 3D morphology analysis, and 3) machine learning-based big data analysis, we present a pathway toward efficient acquisition of holistic dynamic defect evolution with a robust morphological representation. X-ray computed tomography and automated computer vision result in a holistic defect morphology database for the inspected macroscopic volume, based on which machine learning analysis is employed to reveal quantitative insights into the global evolution of defect characteristics beyond qualitative human observation.

We demonstrate this pipeline by examining the global-scale pore evolution in post-processing of binder jetting additive manufacturing, from the green state,to the sintered state, and to the hot isostatic pressed state of copper. The pipeline is shown to be effective at detecting and processing the information associated with a large number of pores in macroscopic volumes. The subsequent principal component analysis and clustering analysis extract the key morphological descriptors and categorize the detected pores into four morphological groups. Through this quantitative defect evolution characterization, including the weight of pore morphology parameters, and the pore number and volume fraction of each categorized group, new understandings are developed regarding the effects of sintering and hot isostatic pressing on pore decomposition, shrinkage, and smoothing during post-processing of binder

jetting.

In conclusion, this thesis proposed two different data-driven tomographic imaging techniques to achieve fast X-ray tomography for 4D material characterization applications with reduced training data. Proposed HSCNN algorithm improves reconstruction quality for insufficient measurements by incorporating prior knowledge of the physics models. HDrec algorithm reduces the acquisition time and dosage by smartly distribute the photon budget between a few high-fidelity projections and a full-view set of low-dosage projections. The applications for two different 4D material characterization demonstrate the advantages based on these proposed tomographic imaging techniques, which provide high-quality reconstructed volume with fast acquisition speed for analysis.

6.2 Future work

Several interesting studies could be continued based on presented methods in this thesis, which could be briefly summarized as follows:

1. Following chapter 4, *in situ* tomographic scan with hybrid-dose techniques will be implemented to study the dynamic damage evolution process in the sea urchin spine structure. Detailed implementation plans are discussed in section 4.3.1.

2. Following chapter 3, HSCNN network could be used as the basic network structure to learn the denoise model in the future to include the prior information in the measurement domain to further reduce the requirement of low-dose projection measurements.

3. Continuing chapter 4 and chapter 5, where we applied the proposed tomographic reconstruction techniques and quantitative image analysis framework to two different 4D damage/defect characterization problems. These approaches also provide the possibilities for

many other material characterization applications, including studying damage evolution under different loading conditions for porous structural materials, defect evolution during sintering or solidification in other metal additive manufacturing materials, investigating liquid dynamics through a constriction, and etc.

4. Following chapter 2 and chapter 3, model-driven based tomographic reconstruction could be explored to further speed up the acquisition, which could provide more continuous measurements compared to data-driven framework.

5. Continuing the quantitative results evaluation framework in the thesis, a quantitative comparison with other material characterization methods for each application could be added to demonstrate the efficiency of our proposed methods, such as comparison the network representation results for sea urchin spine structure, pore analysis results for binder jetting printed materials with commercial software avizo.

In conclusion, this thesis provides the strategies to characterize dynamic evolution processes for different materials in terms of experimental data acquisition, tomographic image reconstruction and 3D image analysis.

Bibliography

[1] E. Maire and P. J. Withers, "Quantitative X-ray tomography," *International Materials Reviews*, vol. 59, no. 1, pp. [1] W. Li, K. G. Field, and D. Morgan, "Automated, 2014.

[2] P. Sedigh Rahimabadi, M. Khodaei, and K. R. Koswattage, "Review on applications of synchrotron-based X-ray techniques in materials characterization," *X-Ray Spectrometry*, vol. 49, no. 3, pp. 348–373, 2020.

[3] W. Kanitpanyacharoen, D. Y. Parkinson, F. De Carlo, F. Marone, M. Stampanoni, R. Mokso, A. MacDowell, and H. R. Wenk, "A comparative study of X-ray tomographic microscopy on shales at different synchrotron facilities: ALS, APS and SLS," *Journal of Synchrotron Radiation*, vol. 20, no. 1, pp. 172–180, 2013.

[4] T. Yang, Z. Wu, H. Chen, Y. Zhu, and L. Li, "Quantitative 3D structural analysis of the cellular microstructure of sea urchin spines (I): Methodology," *Acta Biomaterialia*, vol. 107, pp. 204–217, 4 2020.

[5] E. Maire, "X-Ray Tomography Applied to the Characterization of Highly Porous Materials," *Annual Review of Materials Research*, vol. 42, no. 1, pp. [1] W. Li, K. G. Field, and D. Morgan, "Automated, 2012.

[6] Y. Obata, H. A. Bale, H. S. Barnard, D. Y. Parkinson, T. Alliston, and C. Acevedo, "Quantitative and qualitative bone imaging: A review of synchrotron radiation microtomography analysis in bone research," *Journal of the Mechanical Behavior of Biomedical Materials*, vol. 110, no. June, pp. [1] W. Li, K. G. Field, and D. Morgan, "Automated, 2020.

[7] A. du Plessis and W. P. Boshoff, "A review of X-ray computed tomography of concrete and asphalt construction materials," *Construction and Building Materials*, vol. 199, pp. [1] W. Li, K. G. Field, and D. Morgan, "Automated, 2019.

[8] A. du Plessis, I. Yadroitsava, and I. Yadroitsev, "Effects of defects on mechanical properties in metal additive manufacturing: A review focusing on X-ray tomography insights," *Materials and Design*, vol. 187, pp. [1] W. Li, K. G. Field, and D. Morgan, "Automated, 2020.

[9] A. Du Plessis, I. Yadroitsev, I. Yadroitsava, and S. G. Le Roux, "X-Ray Microcomputed Tomography in Additive Manufacturing: A Review of the Current Technology and Applications," *3D Printing and Additive Manufacturing*, vol. 5, no. 3, pp. [1] W. Li, K. G. Field, and D. Morgan, "Automated, 2018.

[10] C. E. Shannon, "00659497," vol. 3, no. 2, 1998.

[11] H. Zhang, J. Wang, D. Zeng, X. Tao, and J. Ma, "Regularization strategies in statistical image reconstruction of low-dose x-ray CT: A review," *Medical Physics*, vol. 45, no. 10, pp. e886–e907, 2018.

[12] E. Y. Sidky and X. Pan, "Image reconstruction in circular cone-beam computed tomography by constrained, total-variation minimization," *Physics in Medicine and Biology*, vol. 53, pp. 4777–4807, 9 2008.

[13] Y. Liu, J. Ma, Y. Fan, and Z. Liang, "Adaptive-weighted total variation minimization for sparse data toward low-dose x-ray computed tomography image reconstruction," *Physics in Medicine and Biology*, vol. 57, no. 23, pp. 7923–7956, 2012.

[14] Q. Xu, H. Y. Yu, X. Q. Mou, L. Zhang, J. Hsieh, and G. Wang, "Low-dose X-ray

CT reconstruction via dictionary learning," *IEEE Transactions on Medical Imaging*, vol. 31, no. 9, pp. 1682–1697, 2012.

[15] Y. Chen, D. Gao, C. Nie, L. Luo, W. Chen, X. Yin, and Y. Lin, "Bayesian statistical reconstruction for low-dose X-ray computed tomography using an adaptive-weighting nonlocal prior," *Computerized Medical Imaging and Graphics*, vol. 33, no. 7, pp. 495–500, 2009.

[16] K. Kim, J. C. Ye, W. Worstell, J. Ouyang, Y. Rakvongthai, G. E. Fakhri, Q. Li, W. Wu, F. Liu, Y. Zhang, Q. Wang, and H. Yu, "Non-local Low-rank Cube-based Tensor Factorization for Spectral CT Reconstruction," *IEEE Transactions on Medical Imaging*, vol. PP, no. 3, p. 1, 2015.

[17] H. Kim, J. Chen, A. Wang, C. Chuang, M. Held, and J. Pouliot, "Non-local total-variation (NLTV) minimization combined with reweighted L1-norm for compressed sensing CT reconstruction," *Physics in Medicine and Biology*, vol. 61, no. 18, pp. 6878–6891, 2016.

[18] W. Wu, F. Liu, Y. Zhang, Q. Wang, and H. Yu, "Non-local Low-rank Cube-based Tensor Factorization for Spectral CT Reconstruction," *IEEE Transactions on Medical Imaging*, vol. PP, no. c, p. 1, 2018.

[19] M. Hidayetoğlu, T. Bicer, S. G. De Gonzalo, B. Ren, V. De Andrade, D. Gürsoy, R. Kettimuthu, I. T. Foster, and W.-m. W. Hwu, "Petascale xct: 3d image reconstruction with hierarchical communications on multi-gpu nodes," in *Proceedings of the International Conference for High Performance Computing, Networking, Storage and Analysis*, ACM, in press.

[20] M. Hidayetoğlu, T. Biçer, S. G. De Gonzalo, B. Ren, D. Gürsoy, R. Kettimuthu, I. T. Foster, and W.-m. W. Hwu, "Memxct: Memory-centric x-ray ct reconstruction

with massive parallelization," in *Proceedings of the International Conference for High Performance Computing, Networking, Storage and Analysis*, pp. 1–56, 2019.

[21] T. Bicer, D. Gürsoy, V. D. Andrade, R. Kettimuthu, W. Scullin, F. D. Carlo, and I. T. Foster, "Trace: A high-throughput tomographic reconstruction engine for large-scale datasets," *Advanced Structural and Chemical Imaging*, vol. 3, p. 6, Jan 2017.

[22] T. Bicer, D. Gursoy, R. Kettimuthu, F. De Carlo, G. Agrawal, and I. T. Foster, "Rapid tomographic image reconstruction via large-scale parallelization," in *Euro-Par 2015: Parallel Processing*, pp. 289–302, Springer, 2015.

[23] H. Chen, Y. Zhang, Y. Chen, J. Zhang, W. Zhang, H. Sun, Y. Lv, P. Liao, J. Zhou, and G. Wang, "LEARN: Learned Experts' Assessment-Based Reconstruction Network for Sparse-Data CT," *IEEE Transactions on Medical Imaging*, vol. 37, no. 6, pp. 1333–1347, 2018.

[24] Y. Lecun, Y. Bengio, and G. Hinton, "Deep learning," *Nature*, vol. 521, no. 7553, pp. 436–444, 2015.

[25] C. Tian, L. Fei, W. Zheng, Y. Xu, W. Zuo, and C.-W. Lin, "Deep Learning on Image Denoising: An overview," 2019.

[26] G. Ongie, A. Jalal, C. A. Metzler, R. G. Baraniuk, A. G. Dimakis, and R. Willett, "Deep Learning Techniques for Inverse Problems in Imaging," *IEEE Journal on Selected Areas in Information Theory*, vol. 1, no. 1, pp. 39–56, 2020.

[27] G. Wang, J. C. Ye, K. Mueller, and J. A. Fessler, "Image Reconstruction is a New Frontier of Machine Learning," *IEEE Transactions on Medical Imaging*, vol. 37, no. 6, pp. 1289–1296, 2018.

[28] G. Wang, "A perspective on deep imaging," *IEEE Access*, vol. 4, pp. 8914–8924, 2016.

[29] L. Fu and B. De Man, "A hierarchical approach to deep learning and its application to tomographic reconstruction," vol. 1107202, no. May 2019, p. 41, 2019.

[30] W. Wang, X.-G. Xia, C. He, Z. Ren, J. Lu, T. Wang, and B. Lei, "A model-guided deep network for limited-angle computed tomography," vol. 14, no. 8, pp. 1–14, 2020.

[31] H. Lee, J. Lee, and S. Cho, "View-interpolation of sparsely sampled sinogram using convolutional neural network," vol. 1013328, no. February 2017, p. 1013328, 2017.

[32] H. Lee, J. Lee, H. Kim, B. Cho, and S. Cho, "Deep-neural-network based sinogram synthesis for sparse-view CT image reconstruction," *IEEE Transactions on Radiation and Plasma Medical Sciences*, vol. PP, no. c, p. 1, 2018.

[33] H. Yuan, J. Jia, and Z. Zhu, "SIPID: A deep learning framework for sinogram interpolation and image denoising in low-dose CT reconstruction," *Proceedings - International Symposium on Biomedical Imaging*, vol. 2018-April, no. Isbi, pp. 1521–1524, 2018.

[34] D. Karimi, P. Deman, R. Ward, and N. Ford, "A sinogram denoising algorithm for low-dose computed tomography," *BMC Medical Imaging*, vol. 16, no. 1, pp. 1–14, 2016.

[35] X. Yang, V. De Andrade, W. Scullin, E. L. Dyer, N. Kasthuri, F. De Carlo, and D. Gürsoy, "Low-dose x-ray tomography through a deep convolutional neural network," *Scientific Reports*, vol. 8, no. 1, pp. 1–13, 2018.

[36] T. Würfl, M. Hoffmann, V. Christlein, K. Breininger, Y. Huang, M. Unberath, and A. K. Maier, "Deep Learning Computed Tomography: Learning Projection-Domain Weights From Image Domain in Limited Angle Problems," *IEEE Transactions on Medical Imaging*, vol. 37, no. 6, pp. 1454–1463, 2018.

[37] M. U. Ghani and W. C. Karl, "Integrating data and image domain deep learning for limited angle tomography using consensus equilibrium," *Proceedings - 2019 International Conference on Computer Vision Workshop, ICCVW 2019*, pp. 3922–3932, 2019.

[38] K. Monakhova, J. Yurtsever, G. Kuo, N. Antipa, K. Yanny, and L. Waller, "Learned reconstructions for practical mask-based lensless imaging," *Optics Express*, vol. 27, no. 20, p. 28075, 2019.

[39] M. R. Kellman, E. Bostan, N. A. Repina, and L. Waller, "Physics-Based Learned Design: Optimized Coded-Illumination for Quantitative Phase Imaging," *IEEE Transactions on Computational Imaging*, vol. 5, no. 3, pp. 344–353, 2019.

[40] J. Dong, J. Fu, and Z. He, "A deep learning reconstruction framework for X-ray computed tomography with incomplete data," *PLoS ONE*, vol. 14, no. 11, pp. 1–17, 2019.

[41] S. Xie, X. Zheng, Y. Chen, L. Xie, J. Liu, Y. Zhang, J. Yan, H. Zhu, and Y. Hu, "Artifact Removal using Improved GoogLeNet for Sparse-view CT Reconstruction," *Scientific Reports*, vol. 8, no. 1, pp. 1–9, 2018.

[42] Z. Liu, T. Bicer, R. Kettimuthu, D. Gursoy, F. De, and I. Foster, "TomoGAN : Low-Dose Synchrotron X-Ray Tomography," 2020.

[43] H. Chen, Y. Zhang, M. K. Kalra, F. Lin, Y. Chen, P. Liao, J. Zhou, and G. Wang, "Low-Dose CT with a Residual Encoder-Decoder Convolutional Neural Network (RED-CNN)," *IEEE Transactions on Medical Imaging*, vol. 36, no. 12, pp. 2524–2535, 2017.

[44] K. H. Jin, M. T. McCann, E. Froustey, and M. Unser, "Deep Convolutional Neural Network for Inverse Problems in Imaging," *IEEE Transactions on Image Processing*, vol. 26, no. 9, pp. 4509–4522, 2017.

[45] D. M. Pelt and J. A. Sethian, "A mixed-scale dense convolutional neural network for image analysis," *Proceedings of the National Academy of Sciences*, vol. 115, no. 2, pp. 254–259, 2018.

[46] Z. Ren, Z. Xu, and E. Y. Lam, "End-to-end deep learning framework for digital holographic reconstruction," vol. 1, no. 1, pp. 1–12, 2019.

[47] H. Wang, Y. Rivenson, Y. Jin, Z. Wei, and R. Gao, "Deep learning achieves super-resolution in fluorescence microscopy," 2018.

[48] G. Barbastathis, A. Ozcan, and G. Situ, "On the use of deep learning for computational imaging," *Optica*, vol. 6, no. 8, p. 921, 2019.

[49] C. Qiao, H. Qiao, J. Wu, X. Li, J. Fan, and Q. Dai, "Deep learning based tomographic phase microscopy with blind structured illumination," vol. 2019, p. NM3C.3, 2019.

[50] K. Hammernik, T. Klatzer, E. Kobler, M. P. Recht, D. K. Sodickson, T. Pock, and F. Knoll, "Learning a variational network for reconstruction of accelerated MRI data," *Magnetic Resonance in Medicine*, vol. 79, no. 6, pp. 3055–3071, 2018.

[51] J. Adler and O. Öktem, "Learned Primal-Dual Reconstruction," *IEEE Transactions on Medical Imaging*, vol. 37, no. 6, pp. 1322–1332, 2018.

[52] F. Wang, Y. Bian, H. Wang, M. Lyu, G. Pedrini, W. Osten, G. Barbastathis, and G. Situ, "Phase imaging with an untrained neural network," *Light: Science and Applications*, vol. 9, no. 1, 2020.

[53] S. Zhang, L. Li, and A. Kumar, *Materials characterization techniques*. CRC press, 2008.

[54] Y. Leng, *Materials characterization: introduction to microscopic and spectroscopic methods*. John Wiley & Sons, 2009.

[55] Y. Obata, H. A. Bale, H. S. Barnard, D. Y. Parkinson, T. Alliston, and C. Acevedo, "Quantitative and qualitative bone imaging: A review of synchrotron radiation microtomography analysis in bone research," *Journal of the Mechanical Behavior of Biomedical Materials*, vol. 110, p. 103887, 2020.

[56] W. W. Wits, S. Carmignato, F. Zanini, and T. H. Vaneker, "Porosity testing methods for the quality assessment of selective laser melted parts," *CIRP annals*, vol. 65, no. 1, pp. 201–204, 2016.

[57] C. Raufaste, B. Dollet, K. Mader, S. Santucci, and R. Mokso, "Three-dimensional foam flow resolved by fast x-ray tomographic microscopy," *EPL (Europhysics Letters)*, vol. 111, no. 3, p. 38004, 2015.

[58] M. Bührer, M. Stampanoni, X. Rochet, F. Büchi, J. Eller, and F. Marone, "High-numerical-aperture macroscope optics for time-resolved experiments," *Journal of synchrotron radiation*, vol. 26, no. 4, pp. 1161–1172, 2019.

[59] Q. Y. Lu and C. H. Wong, "Additive manufacturing process monitoring and control by non-destructive testing techniques: challenges and in-process monitoring," *Virtual and physical prototyping*, vol. 13, no. 2, pp. 39–48, 2018.

[60] V. Presser, S. Schultheiß, C. Berthold, and K. Nickel, "Sea urchin spines as a model-system for permeable, light-weight ceramics with graceful failure behavior. part i. mechanical behavior of sea urchin spines under compression," *Journal of Bionic Engineering*, vol. 6, no. 3, pp. 203–213, 2009.

[61] D. Müter, H. O. Sørensen, J. Oddershede, K. N. Dalby, and S. L. S. Stipp, "Microstructure and micromechanics of the heart urchin test from x-ray tomography," *Acta Biomaterialia*, vol. 23, pp. 21–26, 2015.

[62] R. Ziel, A. Haus, and A. Tulke, "Quantification of the pore size distribution (porosity profiles) in microfiltration membranes by sem, tem and computer image analysis," *Journal of membrane science*, vol. 323, no. 2, pp. 241–246, 2008.

[63] R. Müller, H. Van Campenhout, B. Van Damme, G. Van der Perre, J. Dequeker, T. Hildebrand, and P. Rüegsegger, "Morphometric analysis of human bone biopsies: a quantitative structural comparison of histological sections and micro-computed tomography," *Bone*, vol. 23, no. 1, pp. 59–66, 1998.

[64] B. Gludovatz, F. Walsh, E. Zimmermann, S. Naleway, R. Ritchie, and J. Kruzic, "Multiscale structure and damage tolerance of coconut shells," *Journal of the mechanical behavior of biomedical materials*, vol. 76, pp. 76–84, 2017.

[65] C. Lauer, S. Schmier, T. Speck, and K. G. Nickel, "Strength-size relationships in two porous biological materials," *Acta Biomaterialia*, vol. 77, pp. 322–332, 2018.

[66] S. M. H. Hojjatzadeh, N. D. Parab, W. Yan, Q. Guo, L. Xiong, C. Zhao, M. Qu, L. I. Escano, X. Xiao, K. Fezzaa, *et al.*, "Pore elimination mechanisms during 3d printing of metals," *Nature communications*, vol. 10, no. 1, pp. 1–8, 2019.

[67] W. E. King, H. D. Barth, V. M. Castillo, G. F. Gallegos, J. W. Gibbs, D. E. Hahn, C. Kamath, and A. M. Rubenchik, "Observation of keyhole-mode laser melting in laser powder-bed fusion additive manufacturing," *Journal of Materials Processing Technology*, vol. 214, no. 12, pp. 2915–2925, 2014.

[68] N. T. Aboulkhair, N. M. Everitt, I. Ashcroft, and C. Tuck, "Reducing porosity in alsi10mg parts processed by selective laser melting," *Additive Manufacturing*, vol. 1, pp. 77–86, 2014.

[69] F. Pierron, S. A. McDonald, D. Hollis, P. J. Withers, and A. Alderson, "Assessment

of the deformation of low density polymeric auxetic foams by x-ray tomography and digital volume correlation," in *Applied Mechanics and Materials*, vol. 70, pp. 93–98, Trans Tech Publ, 2011.

[70] S. Roux, F. Hild, P. Viot, and D. Bernard, "Three-dimensional image correlation from x-ray computed tomography of solid foam," *Composites Part A: Applied science and manufacturing*, vol. 39, no. 8, pp. 1253–1265, 2008.

[71] S. A. McDonald, G. Dedreuil-Monet, Y. T. Yao, A. Alderson, and P. J. Withers, "In situ 3d x-ray microtomography study comparing auxetic and non-auxetic polymeric foams under tension," *physica status solidi (b)*, vol. 248, no. 1, pp. 45–51, 2011.

[72] F. Forsberg, R. Mooser, M. Arnold, E. Hack, and P. Wyss, "3d micro-scale deformations of wood in bending: synchrotron radiation μct data analyzed with digital volume correlation," *Journal of structural biology*, vol. 164, no. 3, pp. 255–262, 2008.

[73] A. du Plessis and C. Broeckhoven, "Looking deep into nature: A review of micro-computed tomography in biomimicry," *Acta biomaterialia*, vol. 85, pp. 27–40, 2019.

[74] S. A. Hall, M. Bornert, J. Desrues, Y. Pannier, N. Lenoir, G. Viggiani, and P. Bésuelle, "Discrete and continuum analysis of localised deformation in sand using x-ray μct and volumetric digital image correlation," *Géotechnique*, vol. 60, no. 5, pp. 315–322, 2010.

[75] F. Tagliaferri, J. Waller, E. Andò, S. A. Hall, G. Viggiani, P. Bésuelle, and J. T. DeJong, "Observing strain localisation processes in bio-cemented sand using x-ray imaging," *Granular Matter*, vol. 13, no. 3, pp. 247–250, 2011.

[76] Z. Chen, X. Jin, L. Li, and G. Wang, "A limited-angle CT reconstruction method based on anisotropic TV minimization," *Physics in Medicine and Biology*, vol. 58, no. 7, pp. 2119–2141, 2013.

[77] H. Yu and G. Wang, "Compressed sensing based interior tomography," *Physics in Medicine and Biology*, vol. 54, no. 13, pp. 4341–4341, 2009.

[78] J. Li, C. Wu, H. Hao, Z. Liu, and Y. Yang, "Basalt scale-reinforced aluminium foam under static and dynamic loads," *Composite Structures*, vol. 203, no. May, pp. [1] W. Li, K. G. Field, and D. Morgan, "Automated, 2018.

[79] I. M. Daniel and J. M. Cho, "Characterization of Anisotropic Polymeric Foam Under Static and Dynamic Loading," *Experimental Mechanics*, vol. 51, no. 8, pp. [1] W. Li, K. G. Field, and D. Morgan, "Automated, 2011.

[80] H. Chen, Y. Zhang, W. Zhang, P. Liao, K. Li, J. Zhou, and G. Wang, "aLow-dose CT via convolutional neural network," *Biomedical Optics Express*, vol. 8, no. 2, p. 679, 2017.

[81] H. Kudo, T. Suzuki, and E. A. Rashed, "Image reconstruction for sparse-view CT and interior CT — introduction to compressed sensing and differentiated backprojection," vol. 3, no. 3, pp. 147–161, 2013.

[82] Z. Zhu, K. Wahid, P. Babyn, D. Cooper, I. Pratt, and Y. Carter, "Improved Compressed Sensing-Based Algorithm for Sparse-View CT Image Reconstruction," vol. 2013, 2013.

[83] H. Yan, X. Mou, S. Tang, Q. Xu, and M. Zankl, "Projection correlation based view interpolation for cone beam ct: Primary fluence restoration in scatter measurement with a moving beam stop array," *Physics in Medicine and Biology*, vol. 55, no. 21, pp. 6353–6375, 2010.

[84] A. Momose, T. Takeda, Y. Itai, and K. Hirano, "© 199 6 Nature Publishing Group

http://www.nature.com/naturemedicine," *Nature Medicine*, vol. 2, no. 4, pp. 473–475, 1996.

[85] T. Le, R. Chartrand, and T. J. Asaki, "A variational approach to reconstructing images corrupted by poisson noise," *Journal of Mathematical Imaging and Vision*, vol. 27, no. 3, pp. 257–263, 2007.

[86] J. C. Y. Yoseob Han, "Framing U-Net via Deep Convolutional Framelets: Application to Sparse-view CT," *Current Opinion in Solid State and Materials Science*, vol. 21, no. 3, pp. 141–158, 2018.

[87] M. Deng, S. Li, and G. Barbastathis, "Learning to synthesize: splitting and recombining low and high spatial frequencies for image recovery,"

[88] A. Krizhevsky, I. Sutskever, and G. E. Hinton, "ImageNet classification with deep convolutional neural networks," *Communications of the ACM*, vol. 60, pp. 84–90, 5 2017.

[89] V. Nair and G. E. Hinton, "Rectified linear units improve restricted boltzmann machines," in *ICML*, 2010.

[90] D. P. Kingma and J. Ba, "Adam: A method for stochastic optimization," *arXiv preprint arXiv:1412.6980*, 2014.

[91] I. Sutskever, J. Martens, G. Dahl, and G. Hinton, "On the importance of initialization and momentum in deep learning," in *International conference on machine learning*, pp. 1139–1147, 2013.

[92] M. Beister, D. Kolditz, and W. A. Kalender, "Iterative reconstruction methods in x-ray ct," *Physica medica*, vol. 28, no. 2, pp. 94–108, 2012.

[93] D. Brunet, E. R. Vrscay, and Z. Wang, "On the mathematical properties of the structural similarity index," *IEEE Transactions on Image Processing*, vol. 21, no. 4, pp. 1488–1499, 2011.

[94] Q. Huynh-Thu and M. Ghanbari, "Scope of validity of psnr in image/video quality assessment," *Electronics letters*, vol. 44, no. 13, pp. 800–801, 2008.

[95] J.-F. Aujol and C. Dossal, "Stability of over-relaxations for the forward-backward algorithm, application to fista," *SIAM Journal on Optimization*, vol. 25, no. 4, pp. 2408–2433, 2015.

[96] A. Biguri, M. Dosanjh, S. Hancock, and M. Soleimani, "Tigre: a matlab-gpu toolbox for cbct image reconstruction," *Biomedical Physics & Engineering Express*, vol. 2, no. 5, p. 055010, 2016.

[97] F. De Carlo, D. Gürsoy, D. J. Ching, K. J. Batenburg, W. Ludwig, L. Mancini, F. Marone, R. Mokso, D. M. Pelt, J. Sijbers, and M. Rivers, "TomoBank: A tomographic data repository for computational x-ray science," *Measurement Science and Technology*, vol. 29, no. 3, 2018.

[98] D. Gürsoy, F. De Carlo, X. Xiao, and C. Jacobsen, "TomoPy: A framework for the analysis of synchrotron tomographic data," *Journal of Synchrotron Radiation*, vol. 21, no. 5, pp. 1188–1193, 2014.

[99] L. Wang, Q. Gao, M. Meng, S. Li, M. Zhu, D. Li, G. Chen, D. Zeng, Q. Xie, Q. Zhao, Z. Bian, D. Meng, and J. Ma, "Semi-supervised noise distribution learning for low-dose CT restoration," vol. 1131244, no. March, p. 149, 2020.

[100] K. Kim, S. Soltanayev, and S. Y. Chun, "Unsupervised Training Of Denoisers For

Low-Dose CT Reconstruction Without Full-Dose Ground Truth," vol. 4553, no. may 1932, pp. 1–15, 2020.

[101] O. Ronneberger, P. Fischer, and T. Brox, "U-net: Convolutional networks for biomedical image segmentation," *Lecture Notes in Computer Science (including subseries Lecture Notes in Artificial Intelligence and Lecture Notes in Bioinformatics)*, vol. 9351, pp. 234–241, 2015.

[102] K. He, X. Zhang, S. Ren, and J. Sun, "Deep residual learning for image recognition," *Proceedings of the IEEE Computer Society Conference on Computer Vision and Pattern Recognition*, vol. 2016-Decem, pp. 770–778, 2016.

[103] H. Chen, Y. Zhang, M. K. Kalra, F. Lin, Y. Chen, P. Liao, J. Zhou, and G. Wang, "Low-Dose CT with a residual encoder-decoder convolutional neural network," *IEEE Transactions on Medical Imaging*, vol. 36, no. 12, pp. 2524–2535, 2017.

[104] K. Simonyan and A. Zisserman, "Very deep convolutional networks for large-scale image recognition," *3rd International Conference on Learning Representations, ICLR 2015 - Conference Track Proceedings*, pp. 1–14, 2015.

[105] Q. Yang, P. Yan, Y. Zhang, H. Yu, Y. Shi, X. Mou, M. K. Kalra, Y. Zhang, L. Sun, and G. Wang, "Low-Dose CT Image Denoising Using a Generative Adversarial Network With Wasserstein Distance and Perceptual Loss," *IEEE Transactions on Medical Imaging*, vol. 37, no. 6, pp. 1348–1357, 2018.

[106] R. L. Siddon, "Fast calculation of the exact radiological path for a three-dimensional CT array," *Medical Physics*, vol. 12, pp. 252–255, 3 1985.

[107] W. Kanitpanyacharoen, D. Y. Parkinson, F. De Carlo, F. Marone, M. Stampanoni, R. Mokso, A. MacDowell, and H.-R. Wenk, "A comparative study of x-ray tomographic

microscopy on shales at different synchrotron facilities: Als, aps and sls," *Journal of synchrotron radiation*, vol. 20, no. 1, pp. 172–180, 2013.

[108] L. J. Gibson, "Biomechanics of cellular solids," *Journal of biomechanics*, vol. 38, no. 3, pp. 377–399, 2005.

[109] L. J. Gibson and M. F. Ashby, *Cellular solids: structure and properties*. Cambridge university press, 1999.

[110] M. F. Ashby and R. M. Medalist, "The mechanical properties of cellular solids," *Metallurgical Transactions A*, vol. 14, no. 9, pp. 1755–1769, 1983.

[111] M. K. Habibi and Y. Lu, "Crack propagation in bamboo's hierarchical cellular structure," *Scientific reports*, vol. 4, no. 1, pp. 1–7, 2014.

[112] I. Daniel and J.-M. Cho, "Characterization of anisotropic polymeric foam under static and dynamic loading," *Experimental mechanics*, vol. 51, no. 8, pp. 1395–1403, 2011.

[113] A. Rafsanjani, D. Derome, F. K. Wittel, and J. Carmeliet, "Computational up-scaling of anisotropic swelling and mechanical behavior of hierarchical cellular materials," *Composites Science and Technology*, vol. 72, no. 6, pp. 744–751, 2012.

[114] N. Tsafnat, J. D. Fitz Gerald, H. N. Le, and Z. H. Stachurski, "Micromechanics of Sea Urchin Spines," *PLoS ONE*, vol. 7, no. 9, pp. [1] W. Li, K. G. Field, and D. Morgan, "Automated, 2012.

[115] V. Presser, S. Schultheiß, C. Berthold, and K. G. Nickel, "Sea Urchin Spines as a Model-System for Permeable, Light-Weight Ceramics with Graceful Failure Behavior. Part I. Mechanical Behavior of Sea Urchin Spines under Compression," *Journal of Bionic Engineering*, vol. 6, no. 3, pp. [1] W. Li, K. G. Field, and D. Morgan, "Automated, 2009.

[116] R. Müller, "Hierarchical microimaging of bone structure and function," *Nature Reviews Rheumatology*, vol. 5, no. 7, pp. 373–381, 2009.

[117] Y. Sun and Q. Li, "Dynamic compressive behaviour of cellular materials: A review of phenomenon, mechanism and modelling," *International Journal of Impact Engineering*, vol. 112, pp. 74–115, 2018.

[118] A. Larrue, A. Rattner, Z.-A. Peter, C. Olivier, N. Laroche, L. Vico, and F. Peyrin, "Synchrotron radiation micro-ct at the micrometer scale for the analysis of the three-dimensional morphology of microcracks in human trabecular bone," *PLoS one*, vol. 6, no. 7, p. e21297, 2011.

[119] D. Roussel, A. Lichtner, D. Jauffrès, J. Villanova, R. K. Bordia, and C. L. Martin, "Strength of hierarchically porous ceramics: Discrete simulations on x-ray nanotomography images," *Scripta Materialia*, vol. 113, pp. 250–253, 2016.

[120] L. Zhang, F. Yang, Y. D. Zhang, and Y. J. Zhu, "Road crack detection using deep convolutional neural network," in *2016 IEEE international conference on image processing (ICIP)*, pp. 3708–3712, IEEE, 2016.

[121] W. Li, K. G. Field, and D. Morgan, "Automated defect analysis in electron microscopic images," *npj Computational Materials*, vol. 4, no. 1, pp. 1–9, 2018.

[122] Y.-J. Cha, W. Choi, and O. Büyüköztürk, "Deep learning-based crack damage detection using convolutional neural networks," *Computer-Aided Civil and Infrastructure Engineering*, vol. 32, no. 5, pp. 361–378, 2017.

[123] H. Homann, "Implementation of a 3d thinning algorithm," *Insight Journal*, vol. 421, 2007.

[124] Y. Ben-Zvi, N. Reznikov, R. Shahar, and S. Weiner, "3d architecture of trabecular bone in the pig mandible and femur: inter-trabecular angle distributions," *Frontiers in Materials*, vol. 4, p. 29, 2017.

[125] C. Lauer, T. B. Grun, I. Zutterkirch, R. Jemmali, J. H. Nebelsick, and K. G. Nickel, "Morphology and porosity of the spines of the sea urchin heterocentrotus mamillatus and their implications on the mechanical performance," *Zoomorphology*, vol. 137, no. 1, pp. 139–154, 2018.

[126] A. Liebscher and C. Redenbach, "Statistical analysis of the local strut thickness of open cell foams," *Image Analysis & Stereology*, vol. 32, no. 1, pp. 1–12, 2013.

[127] P. De Jaeger, C. T'Joen, H. Huisseune, B. Ameel, and M. De Paepe, "An experimentally validated and parameterized periodic unit-cell reconstruction of open-cell foams," *Journal of Applied Physics*, vol. 109, no. 10, p. 103519, 2011.

[128] P. Ma, K. G. Prashanth, S. Scudino, Y. Jia, H. Wang, C. Zou, Z. Wei, and J. Eckert, "Influence of annealing on mechanical properties of al-20si processed by selective laser melting," *Metals*, vol. 4, no. 1, pp. 28–36, 2014.

[129] K. G. Prashanth, S. Scudino, H. J. Klauss, K. B. Surreddi, L. Löber, Z. Wang, A. K. Chaubey, U. Kühn, and J. Eckert, "Microstructure and mechanical properties of al–12si produced by selective laser melting: Effect of heat treatment," *Materials Science and Engineering: A*, vol. 590, pp. 153–160, 2014.

[130] K. Prashanth, H. S. Shahabi, H. Attar, V. Srivastava, N. Ellendt, V. Uhlenwinkel, J. Eckert, and S. Scudino, "Production of high strength al85nd8ni5co2 alloy by selective laser melting," *Additive Manufacturing*, vol. 6, pp. 1–5, 2015.

[131] A. Mostafaei, J. Toman, E. L. Stevens, E. T. Hughes, Y. L. Krimer, and M. Chmielus,

"Microstructural evolution and mechanical properties of differently heat-treated binder jet printed samples from gas-and water-atomized alloy 625 powders," *Acta Materialia*, vol. 124, pp. 280–289, 2017.

[132] R. J. Griffiths, M. E. Perry, J. M. Sietins, Y. Zhu, N. Hardwick, C. D. Cox, H. A. Rauch, and Z. Y. Hang, "A perspective on solid-state additive manufacturing of aluminum matrix composites using meld," *Journal of Materials Engineering and Performance*, vol. 28, no. 2, pp. 648–656, 2019.

[133] A. Mostafaei, E. L. Stevens, E. T. Hughes, S. D. Biery, C. Hilla, and M. Chmielus, "Powder bed binder jet printed alloy 625: Densification, microstructure and mechanical properties," *Materials & Design*, vol. 108, pp. 126–135, 2016.

[134] A. Y. Kumar, J. Wang, Y. Bai, S. T. Huxtable, and C. B. Williams, "Impacts of process-induced porosity on material properties of copper made by binder jetting additive manufacturing," *Materials & Design*, vol. 182, p. 108001, 2019.

[135] S. K. Everton, M. Hirsch, P. Stravroulakis, R. K. Leach, and A. T. Clare, "Review of in-situ process monitoring and in-situ metrology for metal additive manufacturing," *Materials & Design*, vol. 95, pp. 431–445, 2016.

[136] M. Seifi, M. Gorelik, J. Waller, N. Hrabe, N. Shamsaei, S. Daniewicz, and J. J. Lewandowski, "Progress towards metal additive manufacturing standardization to support qualification and certification," *Jom*, vol. 69, no. 3, pp. 439–455, 2017.

[137] A. Fire, "8.1. 0: 1995–2014©, fei, sas–visualization sciences group, hillsboro, usa," 2014.

[138] W. S. Rasband *et al.*, "Imagej," 1997.

[139] M. Seifi, M. Gorelik, J. Waller, N. Hrabe, N. Shamsaei, S. Daniewicz, and J. J. Lewandowski, "Progress Towards Metal Additive Manufacturing Standardization to Support Qualification and Certification," *Jom*, vol. 69, no. 3, pp. 439–455, 2017.

[140] A. Mosavi, T. Rabczuk, and A. R. Varkonyi-Koczy, "Reviewing the novel machine learning tools for materials design," in *International Conference on Global Research and Education*, pp. 50–58, Springer, 2017.

[141] D. M. Dimiduk, E. A. Holm, and S. R. Niezgoda, "Perspectives on the impact of machine learning, deep learning, and artificial intelligence on materials, processes, and structures engineering," *Integrating Materials and Manufacturing Innovation*, vol. 7, no. 3, pp. 157–172, 2018.

[142] J. Schmidhuber, "Deep learning in neural networks: An overview," *Neural networks*, vol. 61, pp. 85–117, 2015.

[143] J. A. Slotwinski, E. J. Garboczi, and K. M. Hebenstreit, "Porosity measurements and analysis for metal additive manufacturing process control," *Journal of research of the National Institute of Standards and Technology*, vol. 119, p. 494, 2014.

[144] R. Cunningham, S. P. Narra, C. Montgomery, J. Beuth, and A. Rollett, "Synchrotron-based x-ray microtomography characterization of the effect of processing variables on porosity formation in laser power-bed additive manufacturing of ti-6al-4v," *Jom*, vol. 69, no. 3, pp. 479–484, 2017.

[145] A. Du Plessis, S. G. le Roux, J. Els, G. Booysen, and D. C. Blaine, "Application of micro-ct to the non-destructive testing of an additive manufactured titanium component," *Case Studies in Nondestructive Testing and Evaluation*, vol. 4, pp. 1–7, 2015.

[146] M. Kachanov, "Elastic solids with many cracks and related problems," in *Advances in applied mechanics*, vol. 30, pp. 259–445, Elsevier, 1993.

[147] M. Kachanov, I. Tsukrov, and B. Shafiro, "Effective moduli of solids with cavities of various shapes," 1994.

[148] S. Romano, A. Brandão, J. Gumpinger, M. Gschweitl, and S. Beretta, "Qualification of am parts: extreme value statistics applied to tomographic measurements," *Materials & Design*, vol. 131, pp. 32–48, 2017.

[149] P. Lykov, E. Safonov, and A. Akhmedianov, "Selective laser melting of copper," in *Materials Science Forum*, vol. 843, pp. 284–288, Trans Tech Publ, 2016.

[150] A. Thompson, N. Senin, I. Maskery, and R. Leach, "Effects of magnification and sampling resolution in x-ray computed tomography for the measurement of additively manufactured metal surfaces," *Precision Engineering*, vol. 53, pp. 54–64, 2018.

[151] Z. Wu, T. Yang, L. Li, and Y. Zhu, "Feature-based sparse angle tomography reconstruction for dynamic characterization of bio-cellular materials," in *Computational Imaging III*, vol. 10669, p. 106690O, International Society for Optics and Photonics, 2018.

[152] S. Wold, K. Esbensen, and P. Geladi, "Principal component analysis," *Chemometrics and intelligent laboratory systems*, vol. 2, no. 1-3, pp. 37–52, 1987.

[153] C. J. Veenman, M. J. T. Reinders, and E. Backer, "A maximum variance cluster algorithm," *IEEE Transactions on pattern analysis and machine intelligence*, vol. 24, no. 9, pp. 1273–1280, 2002.

[154] D. Xu and Y. Tian, "A comprehensive survey of clustering algorithms," *Annals of Data Science*, vol. 2, no. 2, pp. 165–193, 2015.

[155] T. K. Moon, "The expectation-maximization algorithm," *IEEE Signal processing magazine*, vol. 13, no. 6, pp. 47–60, 1996.

[156] T. Kanungo, D. M. Mount, N. S. Netanyahu, C. D. Piatko, R. Silverman, and A. Y. Wu, "An efficient k-means clustering algorithm: Analysis and implementation," *IEEE transactions on pattern analysis and machine intelligence*, vol. 24, no. 7, pp. 881–892, 2002.

[157] S. I. Vrieze, "Model selection and psychological theory: a discussion of the differences between the akaike information criterion (aic) and the bayesian information criterion (bic).," *Psychological methods*, vol. 17, no. 2, p. 228, 2012.

[158] A. Kumar, Y. Bai, A. Eklund, and C. B. Williams, "Effects of hot isostatic pressing on copper parts fabricated via binder jetting," *Procedia Manufacturing*, vol. 10, pp. 935–944, 2017.

[159] A. Y. Kumar, Y. Bai, A. Eklund, and C. B. Williams, "The effects of hot isostatic pressing on parts fabricated by binder jetting additive manufacturing," *Additive Manufacturing*, vol. 24, pp. 115–124, 2018.

[160] J. Gonzalez, J. Mireles, Y. Lin, and R. B. Wicker, "Characterization of ceramic components fabricated using binder jetting additive manufacturing technology," *Ceramics International*, vol. 42, no. 9, pp. 10559–10564, 2016.

[161] A. Mostafaei, P. R. De Vecchis, I. Nettleship, and M. Chmielus, "Effect of powder size distribution on densification and microstructural evolution of binder-jet 3d-printed alloy 625," *Materials & Design*, vol. 162, pp. 375–383, 2019.

[162] M. Shanker, M. Y. Hu, and M. S. Hung, "Effect of data standardization on neural network training," *Omega*, vol. 24, no. 4, pp. 385–397, 1996.

[163] C. L. Cramer, P. Nandwana, R. A. Lowden, and A. M. Elliott, "Infiltration studies of additive manufacture of wc with co using binder jetting and pressureless melt method," *Additive Manufacturing*, vol. 28, pp. 333–343, 2019.

[164] A. Mostafaei, S. H. V. R. Neelapu, C. Kisailus, L. M. Nath, T. D. Jacobs, and M. Chmielus, "Characterizing surface finish and fatigue behavior in binder-jet 3d-printed nickel-based superalloy 625," *Additive Manufacturing*, vol. 24, pp. 200–209, 2018.